Geochemical and mineralogical investigation of mine tailings and mine-impacted sediments at Long Lake near Sudbury, Ontario

Birendra Sapkota

Thesis submitted to the University of Ottawa in partial fulfillment of the requirements for the Master's Degree in Earth Sciences

Department of Earth and Environmental Sciences
Faculty of Science
University of Ottawa

Statement of co-authorship

This thesis is the summary of an original research undertaken at the University of Ottawa by Birendra Sapkota under the supervision of Prof. Tom Al. It includes two chapters that have been published in peer-reviewed journals in slightly modified form. The contributions of co-authors in the papers are stated below:

Thesis Chapter	**Paper citation**	**Author contribution**
Chapter 2	Sapkota, B., Verbuyst, B., Bain, J., Ptacek, C., Blowes, D., Al, T., 2023. Geochemical and mineralogical investigation of cemented crusts in the tailings cover at Long Lake Gold Mine, Sudbury, Canada. *Journal of Hazardous Materials* 451, 131192.	B. Sapkota: collection of cemented crust samples, solid-phase geochemical and mineralogical analyses, original-draft preparation B. Verbuyst: measurements of hydrogeological parameters, aqueous geochemical analysis J. Bain: vertical core sampling C. Ptacek; D. Blowes: supervision on B. Verbuyst's work T. Al: supervision, collection of cemented crust samples, analysis of diffraction patterns, conceptual model on evolution of cemented crusts, review and editing
Chapter 3	Sapkota, B. and Al, T., 2024. Diagenetic iron-oxyhydroxides formed in suboxic to anoxic mine-impacted lake sediments near Sudbury, Ontario. *Chemical Geology 658, 122131.*	B. Sapkota: geochemical and mineralogical analyses, original-draft preparation T. Al: supervision, collection of sediment cores with Simon Hayles, analysis of diffraction patterns and EELS data, review and editing

Abstract

The former Long Lake Gold Mine (1908–1939) near Sudbury, Ontario, produced sulfide-bearing tailings that were discharged directly to shallow wetland areas without containment, and oxidation of sulfide minerals (mainly pyrite and arsenopyrite) has resulted in elevated aqueous arsenic (As) concentrations downstream in Luke Creek and Long Lake. Over time, erosion and transport of tailings-derived solids, and their deposition in the lake formed a sediment delta at the mouth of the creek. In the early 1970s, the Ontario government constructed a sand cover (~ 0.3 m thick) to stabilize the tailings surface and the sand cover now contains cemented crusts formed by precipitation of secondary minerals. The cemented sand layer has eroded at several locations and the transport of the eroded material by surface-water runoff has become a secondary source of pollution to the surrounding environment. The main objectives of this research were to characterize the nature and distribution of cemented crusts in the tailings and the sand cover, and to understand diagenetic transformations that affect tailings-derived oxidation products following burial in the sediment delta. Vertical cores were collected from the tailings and the sediment delta. They were dried anaerobically, and polished thin sections were prepared for examination by SEM-EDS, EPMA, and (S)TEM-EDS/EELS. Elevated concentrations of solid-phase As (1.41 wt.%), Fe (7.62 wt.%), and S (2.88 wt.%) in the sand layer indicate upward transport of sulfide-oxidation products from the underlying tailings. The mineralogical observations indicate moderate to high degrees of sulfide-mineral oxidation in the shallow (< 0.7 m depth) tailings, and secondary minerals in the tailings and the sand layer mainly consist of ferric-arsenates (principally scorodite) and K/Na-jarosite. The shallow porewater is acidic (pH 4 − 6) and contains elevated concentrations of As (up to 346 mg/L), Fe (up to 1844 mg/L), and SO_4 (up to 12,000 mg/L). The capillary rise of tailings porewater led to the precipitation of ferric-arsenates and K/Na-jarosite that cemented the sand

particles and formed cemented crusts. The distribution of secondary-mineral precipitates is variable in the sand cover, leading to a distribution of cemented crusts that is discontinuous both vertically and horizontally. The lake sediment contains numerous fragments of cemented crusts in the mine-impacted section (maximum depth 1.9 m). Compared to the cemented crusts that occur in the tailings areas, these fragments display partial-dissolution features. The partial-dissolution of scorodite and K/Na-jarosite contribute to elevated aqueous concentrations of As, Fe, and SO_4 near the sediment-water interface, creating concentration gradients that can drive diffusive transport upward into the lake water and downward into the underlying natural sediment. In comparison to the crusts in the tailings, the sediment-hosted crusts have relatively low and variable As/Fe ratios, implying selective As-depletion. The depletion and mobilization of As leaves residual ferric-arsenates progressively enriched with Fe, and as a result, Fe-oxyhydroxides (nm to μm size) form as the main diagenetic product in the sediment. They occur throughout the mine-impacted sediment, from the surface to depths where Fe- and As-sulfides form in response to sulfate reduction in suboxic-anoxic conditions. Fe-oxyhydroxides exhibit diverse morphologies, with some consisting of aggregates of lepidocrocite microcrystals arranged in spherulitic form with silica in the interstitial spaces. The lepidocrocite microcrystals contain a mixture of Fe(III) and Fe(II), with Fe(III)/ΣFe = approximately 0.8. The mineralogical forms of As-bearing phases that control As concentrations in the tailings and sediment porewater can have implications for design of remediation plans. Future remediation efforts may benefit from knowledge of the mineralogical forms of As, and understanding of the erosion and transport of tailings-derived solids and their diagenesis upon burial in the lake sediment.

Acknowledgements

My interest to work on mine wastes developed while working in an environmental consulting firm. My supervisor, Dr. Tom Al, provided me an opportunity to get involved in research on mine wastes. I am indebted to him for his guidance, and his contribution to my knowledge and analytical skills in geochemistry and mineralogy. I would like to thank him for his unwavering support throughout my time at the University of Ottawa.

I would like to extend my thanks to Dr. Al's research team, research staff at the University of Ottawa, and my committee (Dr. Danielle Fortin and Dr. Richard Amos) for their support.

I would like to acknowledge the funding provided by the Natural Sciences and Engineering Research Council of Canada Strategic Partnership Grants for Networks Program, 'Toward Environmentally Responsible Resource Extraction Network' (NSERC-TERRE-NET).

Finally, I extend my appreciation to my family for their enduring patience and support all the time.

Table of Contents

List of Figures

List of Tables

CHAPTER ONE

INTRODUCTION

1.1. Mine waste

Mine waste refers to uneconomic material discarded during mining. It originates from excavation and further physical and chemical processing of a wide range of metalliferous and non-metalliferous ores (Szczepanska and Twardowska, 2004). From metalliferous ores in particular, only a small fraction of valuable component is extracted, while the majority of the total mined material is rejected as processing and metallurgical waste (Lottermoser, 2010). Although present-day mines in developed countries operate under stringent environmental regulations (Parbhakar-Fox and Lottermoser, 2015), managing mine wastes and minimizing environmental impacts associated with resource extraction and refining operations present significant challenges (Perreault et al., 2015). Specifically, sulfide-bearing mine wastes exposed to weathering processes have the potential to generate acid mine drainage (AMD) with elevated concentrations of dissolved metals (Ohlander et al., 2012) which can negatively affect ecosystems (Gray, 1997; Hogsden and Harding, 2012).

Safe, long-term containment of mine waste is one of the main challenges in the mining industry (Vriens et al., 2020). Waste rock (wall rock material removed to access and mine ore) is typically stored in piles near the mining sites, whereas tailings (fine-grained residue from the ore concentration process) are usually pumped to surface facilities where they are disposed of either subaerially or under water (Hotton et al., 2020; Williams, 2020). For sulfide-bearing tailings, installation of an engineered cover system over the tailings is one of the most commonly adopted measures to control AMD. The cover system can vary from a single layer of natural soil to multiple

layers consisting of different soil types, geofabrics, capillary barriers, and geomembranes (Bussière et al., 2003). Other strategies for AMD reduction include neutralization (blending with lime), desulfurization, which consists of separating a large amount of the sulfide minerals from the mine tailings prior to disposal (Benzaazoua et al., 2008), co-disposal with waste rock, and passivation (e.g., precipitation of Fe-oxyhydroxide coatings on the surfaces of sulfide minerals) (Neculita et al., 2007; Park et al., 2019; Ighalo et al., 2022). The implementation of such techniques has helped to decrease the occurrence of AMD in some active mines (Jackson et al., 2015; Bussière et al., 2020). However, at abandoned mines, where waste materials are often found deposited along water courses or low-lying areas close to the mills (Walker et al., 2009), weathering and erosion has resulted in significant human and environmental impacts (Dudka and Adriano, 1997; Jamieson, 2011; DeSisto et al., 2016). The long-term potential environmental risks of many legacy mines are still largely unknown (Moyo et al., 2023).

1.2. Mine waste weathering

Sulfide-bearing minerals (e.g., pyrite [FeS_2], pyrrhotite [Fe(1-x)S], arsenopyrite [FeAsS]) are not targeted for recovery because of their low economic value (Blowes et al., 2003). Consequently, these minerals are contained in tailings and waste rock, and can undergo oxidation resulting in the release of acid and metal(loid)s (Wunderly et al., 1996; Rimstidt and Vaughan., 2003). A brief overview of pyrite oxidation, which is a widely studied topic, is presented here, and detailed information about the reactions involved can be found in Nordstrom (1982). Abiotic oxidation of pyrite occurs when it is exposed to oxidants such as dissolved oxygen or ferric iron [Fe (III)]. The reaction of pyrite with dissolved oxygen is illustrated in (Equation 1).

$$FeS_{2(s)} + \frac{7}{2}O_2 + H_2O \rightarrow Fe^{2+} + 2SO_4^{2-} + 2H^+ \qquad (1)$$

The Fe^{2+} released from pyrite oxidation oxidizes to Fe^{3+} in the presence of excess oxygen and with the consumption of protons (Equation 2). Hydrolysis of Fe^{3+} promotes precipitation of Fe(III)-oxyhydroxides and generates additional H^+ (Equation 3). The overall process of abiotic pyrite oxidation with oxygen as an oxidant (Equation 4), therefore, involves the reaction of pyrite with oxygen and water to form ferric-oxyhydroxide and sulfuric acid [in Equations 3 and 4, $Fe(OH)_3$ represents a variety of possible Fe-oxyhydroxides].

$$Fe^{2+} + \frac{1}{4} O_2 + H^+ \rightarrow Fe^{3+} + \frac{1}{2} H_2O \quad (2)$$

$$Fe^{3+} + 3H_2O = Fe(OH)_{3(s)} + 3H^+ \quad (3)$$

$$FeS_{2(s)} + \frac{15}{4} O_2 + \frac{7}{2} H_2O \rightarrow Fe(OH)_{3(s)} + 2H_2SO_4 \quad (4)$$

Once ferric iron (Fe^{3+}) is formed, it becomes the primary oxidant of pyrite at low pH (Equation 5), interacting with reactive surface sites of sulfide minerals more effectively than dissolved oxygen (Moses et al., 1987).

$$FeS_{2(s)} + 14Fe^{3+} + 8H_2O \rightarrow 15Fe^{2+} + 2SO_4^{2-} + 16H^+ \quad (5)$$

Biologically-mediated sulfide-mineral oxidation is accomplished by certain lithotrophic prokaryotes (those that obtain energy from oxidation of inorganic compounds). At neutral pH condition, neutrophilic thiobacilli can oxidize metal sulfides, and as the pH decreases, acid-tolerant (acidophilic) bacteria catalyze sulfide oxidation reactions (Blowes et al., 1995). Nordstrom and Southam (1997) and Johnson and Hallberg (2003) list Fe-oxidizers (e.g., *Thiobacillus ferrooxidans, Leptospirillum ferrooxidans*) and S-oxidizers (e.g., *Acidithiobacillus thiooxidans, Thiomonas cuprina*) that contribute to the formation of ferric iron and sulfuric acid as by-products of their metabolism. Likewise, As-oxidizers (e.g., *Leptothrix sp.*, *Thiomonas sp*.) that are able to survive in As-contaminated mining environment can also catalyze sulfide oxidation reactions

(Hudson-Edwards et al., 2013). These studies indicate that the rate of microbially-mediated sulfide-mineral oxidation is greater by many orders of magnitude than abiotic oxidation.

The reactions (Equations 1–5) between sulfide minerals and oxidants (O_2 and Fe(III)) lead to the formation of secondary minerals (Table 1) that accumulate on grain surfaces or within pore spaces among tailings particles. Petrunic et al. (2009) explain two general conditions leading to secondary mineral formation: i) precipitation when the porewater saturation state is exceeded, and ii) incongruent dissolution and in-situ transformation of primary minerals undergoing weathering reactions. Precipitation of secondary minerals plays an important role in attenuating concentrations of metal(loid)s in drainage water. For example, the precipitation of Fe-oxyhydroxides provides increased capacity for adsorption of arsenic (Zhang et al., 1999). Most importantly, the precipitation of such secondary minerals can lead to reductions in sulfide-oxidation rates by limiting oxygen diffusion to sulfide minerals, and over a long time, can lead to the development of cemented crusts and hardpans (Blowes et al., 1990; Jamieson et al., 2015; Sapkota et al., 2023). In Fe-As-rich tailings, Fe-arsenate minerals are the most commonly observed secondary mineral precipitates, with scorodite ($FeAsO_4{\cdot}2H_2O$) being the most prevalent (Drahota and Filippi, 2009). In fact, scorodite is often a desired secondary mineral as its low solubility limits the concentration of arsenic in AMD (Flemming et al., 2005). However, it tends to dissolve incongruently in contact with water, and thus, there are concerns over its long-term stability (Bluteau and Demopoulos, 2007). In suboxic-anoxic environments, microbially-mediated reductive dissolution of scorodite can be the dominant mechanism, as demonstrated by several microcosm-based studies (Newman et al., 1998; Nicholas et al., 2003; Revesz et al., 2015). Under anoxic conditions, microorganisms fulfill their respiration requirements by oxidation of an electron donor, such as organic carbon, coupled to the reduction of terminal electron acceptors such as As(V) and Fe(III) (Cummings et

al., 1999). Common dissimilatory As(V)-reducing bacteria related to *Geospirillum* and *Bacillus* spp. (Macy et al., 2000; Oremland and Stolz, 2003) and Fe(III)-reducing bacteria related to *Shewanella* and *Geobacter* spp. (Cummings et al., 1999; Esther et al., 2015) lead to the reduction of structurally-bound As(V) and Fe(III) and the release of As(III) and Fe(II) to porewater.

Together, these studies indicate that in Fe-As-rich tailings, oxidation of sulfide-bearing minerals can lead to the precipitation of secondary minerals (e.g., ferric arsenate, ferric-arsenate sulfate) that sequester As, Fe, and S by removing them from the solution, but these secondary minerals can get destabilized under anoxic conditions by incongruent or dissimilatory microbial-reduction, and subsequently release these elements back into the porewater. In sufficiently reducing conditions, dissimilatory sulfate reduction can occur (Fortin and Beveridge, 1997) and favour the removal of these elements from the solution and become incorporated into Fe and As-sulfides, thereby, completing Fe, As, and S cycles in the mine waste and the surrounding environment.

Table 1.1. List of common secondary minerals found in sulfide mine wastes

Mineral	**Formula**
Ferrihydrite	$Fe_{10}O_{14}(OH)_2$
Goethite	α-FeOOH
Lepidocrocite	γ-FeOOH
Scorodite	$FeAsO_4 \cdot 2H_2O$
K-jarosite	$KFe_3(SO_4)_2(OH)_6$
Na-jarosite	$NaFe_3(SO_4)_2(OH)_6$
Hydronium-jarosite	$(H_3O)Fe_3(SO_4)_2(OH)_6$
Gypsum	$CaSO_4 . 2H_2O$

Gibbsite	$Al(OH)_3$
Schwertmannite	$Fe_{16}O_{16}(SO_4)_2.nH_2O$
Epsomite	$MgSO_4.7H_2O$
Anglesite	$PbSO_4$

1.3. Mineralogical and geochemical characterization

The extent of environmental impacts from mine waste depends on the mineralogical and geochemical composition of waste material, local climate, and in-situ chemical, biological, and physical processes (Nordstrom and Southam, 1997; Lindsay et al., 2015). Many case studies (e.g., Al et al., 1994; Blowes et al., 1995; Gierre et al., 2003; Ahn et al., 2005; Salzsauler et al., 2005; Seal et al., 2008; Jamieson, 2011; DeSisto et al., 2016) involving geochemical and mineralogical characterization of mine waste and weathering products have investigated stability of minerals at the local environmental conditions, the fate and transport of contaminants from waste impoundments, and associated environment risks.

Jamieson et al. (2011) and Hammarstrom and Smith (2002) provide an overview of analytical methods that have been commonly used to study mine waste mineralogy. Powder X-ray diffraction (XRD), a bulk characterization technique, involves determination of diffraction patterns from samples and matching them against a database for mineral identification. The most abundant minerals can be identified with this method; however, it can become difficult to identify minerals that make up less than a few percent of the entire sample and those that are poorly crystalline or amorphous (Jamieson et al., 2015). Identification of common rock-forming minerals and observation of textures (e.g., corroded borders) associated with weathered minerals can be performed using optical microscopy. However, secondary minerals that precipitate in mine waste

are often micro- to nano-crystalline (Hochella et al., 1999), and mineral identification is not always possible with the optical microscope. Scanning electron microscopy (SEM) and energy-dispersive spectroscopy (EDS) have proven to be valuable microscale mineral identification and characterization techniques (e.g., Roussel et al., 2000; Salzsauler et al., 2005; Bao et al., 2022). Likewise, Electron microprobe analysis (EPMA) provides quantitative chemical analysis with μm-scale spatial resolution which is useful to identify and characterize secondary phases. More recently, studies have begun to use high-resolution imaging techniques such as transmission electron microscopy (TEM) to identify μm- to nm-scale secondary phases (e.g., Hochella et al., 1999; Petrunic and Al, 2005; Petrunic et al., 2006; Petrunic et al., 2009; Schindler and Singer, 2017). These and other similar studies have demonstrated that reaction processes in mine wastes can occur at various scales, and therefore, a combination of cross-scale mineralogical measurements ranging from mm- to nm-scale (Bao et al., 2021) are desirable to understand distribution and reactivity of minerals.

Mine waste studies often combine mineralogical and geochemical techniques to understand mineral-water interactions that are responsible for dissolution of primary minerals and precipitation of secondary minerals (e.g., Blowes and Jambor, 1990; Hudson-Edwards et al., 1999; Petrunic and Al, 2005; Parviainen, 2009). X-ray fluorescence is a non-destructive method widely used for determination of major-element oxides and trace elements. It is generally limited to elements with high atomic number ($Z > 16$) (Fitton, 2014). For determination of total carbon, nitrogen, and sulphur contents, a dry-combustion instrument with an infrared detector (e.g., CNS-2000 analyzer; LECO Corporation Inc.) is commonly used (Kowalenko, 2001). Likewise, for multi-element analysis of aqueous and solid samples, studies rely on inductively-coupled plasma optical-emission spectrometry (ICP-OES) or inductively-coupled plasma mass spectrometry (ICP-

MS), while determinations of anions in aqueous samples have been obtained by ion chromatography (IC). Measurements of pH and redox potential, which are master variables controlling the stability and fate of mineral species at low temperature (Nordstrom, 2011), are conducted during the aqueous sampling program. In addition, aqueous geochemical modelling using the geochemical equilibrium models, such as PHREEQC (Parkhurst and Appelo, 1999) and the WATEQ4F database (Ball and Nordstrom, 1991), have also been used to assess species distribution in porewater and calculate the saturation indices for minerals. Such models have proven to be useful for understanding geochemical evolution of AMD (Molson et al., 2008, Amos et al., 2015), and to predict secondary-mineral precipitation in mine tailings. In summary, mine waste studies have shown that the integration of the results from simultaneous mineralogical and geochemical investigations can lead to a better understanding of the inherently complex biogeochemical interactions that occur in mine waste environments, help assess environmental risk, and prepare for effective mine waste remedial options.

1.4. Long Lake Gold Mine

The former Long Lake Gold Mine (46º 18’ 19.1’’ N and 81º, 8’ 59.5’’ W) (Fig. 1.1) is located in Eden Township, approximately 17 km southwest of the city of Sudbury. Gold was discovered in 1907 and consisted mainly of gold-bearing pyrite and arsenopyrite in quartz veins hosted in quartzite (Winter, 1987). The mine operated intermittently from 1908 until the main arsenopyrite ore zone was mined out in 1939 (Gordon et al., 1979). Approximately 200,487 tons of ore were milled at a grade of 8.1 g/tonne (CH2M HILL, 2014). During the operations, approximately 163,000 m^3 of tailings were discharged directly onto the ground without additional containment. The tailings areas consist of three interconnected areas (TA-01, TA-02, and TA-03), TA-01 being the largest (7.1 ha). The tailings were discharged into lowland areas connected by Luke Creek, and

subsequent erosion and transport of tailings-derived solids downstream into Long Lake has formed a sediment delta at the mouth of the creek.

Sulfide minerals (mainly pyrite and arsenopyrite) in the tailings were exposed to the environment for nearly 30 years before a sand cover (approximately 0.3 m thick) was applied in 1970 to prevent erosion, oxidation, and transport of the sulfide minerals (CH2M HILL, 2014). However, concerns have been raised regarding the mine impact on wetland ecology downstream of the tailings. The Ontario government has monitored surface-water quality in Luke Creek and Long Lake, and records from 2012 to 2018 show arsenic concentrations ranging from 95 to 133 µg/L, which are well-above the guideline concentration of 5 µg/L for the protection of aquatic life (CCME, 1997). Likewise, analysis of groundwater samples from TA-01 show elevated arsenic in most of the samples (15 to 67,800 µg/L) (SNC-Lavalin, 2016). The capillary rise of contaminated tailings porewater has led to the precipitation of secondary minerals, forming cemented crusts in the sand cover. The cemented sand layer has eroded at several locations and transport of the cover material with surface-water runoff has become a secondary source of pollution to the surrounding environment.

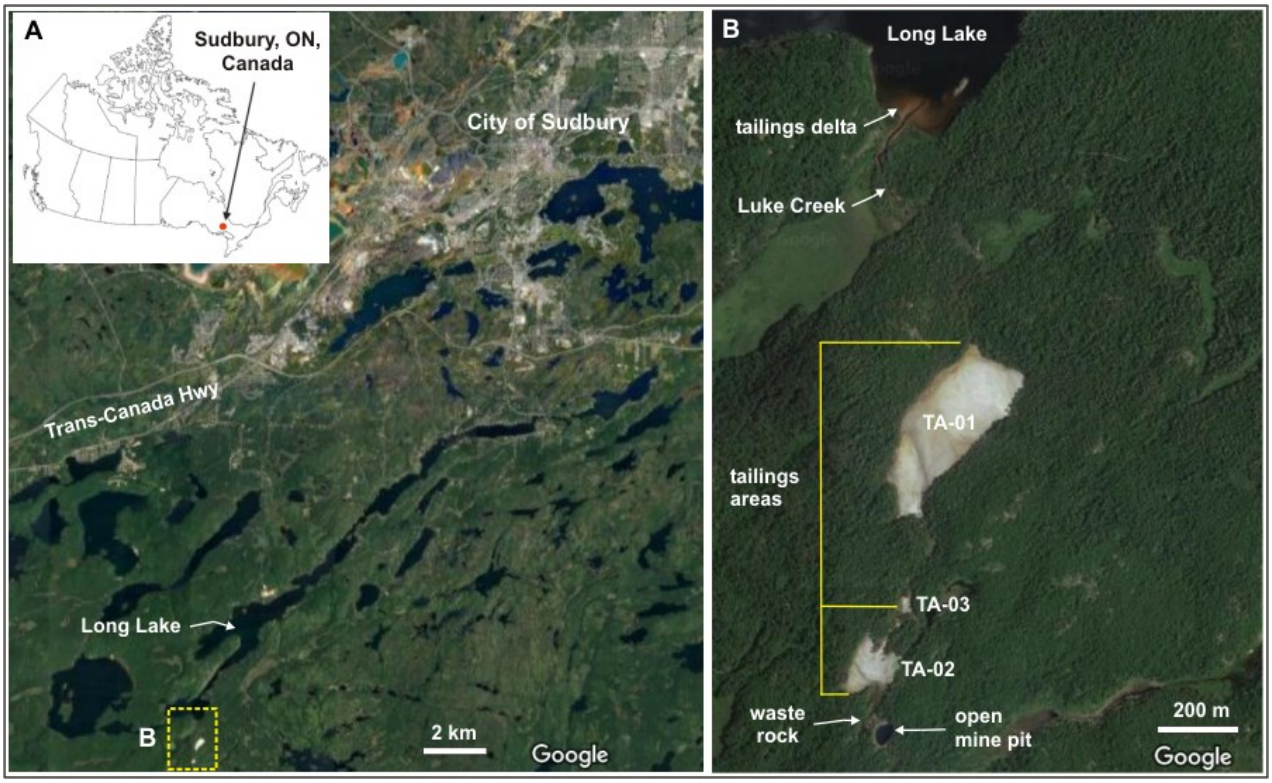

Fig. 1.1. Map showing the location of the former Long Lake Gold Mine. Yellow rectangle (A) represents the studied area and a magnified region in B shows the tailings areas and a sediment delta at the mouth of Luke Creek.

1.5. Goals and objectives

The overall goals of this research were to investigate the extent of sulfide-mineral oxidation and secondary-mineral accumulation in the Long Lake tailings, and diagenetic transformations that affect tailings-derived oxidation products following burial in the lacustrine sedimentary delta.

The specific objectives required to accomplish this goal were:

1) conduct a detailed characterization of cemented crusts to determine the composition and distribution of secondary minerals in the tailings and in the sand cover,
2) conduct a detailed characterization of the mine-impacted sediment delta to understand diagenetic transformations of tailings-derived oxidation products and subsequent formation of diagenetic minerals, and
3) conduct geochemical measurements on the tailings and the mine-impacted sediment to understand the nature and reactivity of the solids, and the mobility of metals.

1.6. Thesis structure

This thesis is organized in four chapters that reflect the objectives and main outcomes of the research. Chapter 1 introduces the concepts of mine waste, and weathering reactions, and it highlights the need for detailed geochemical and mineralogical studies to understand the risk of contamination from mine waste. Chapter 2 focuses on the transport of aqueous solutes from oxidized tailings and precipitation of secondary minerals that can lead to the formation of cemented crusts in the tailings and cover material. Chapter 2 has been published in the Journal of Hazardous Materials (Sapkota et al., 2023). Chapter 3 examines diagenetic transformations in tailings-derived material following burial in lake sediment. This chapter has been published in Chemical Geology (Sapkota and Al, 2024). Given that chapters 2 and 3 are included in the form of journal

publications, their content stands alone, including the description of materials and methods which are not described separately. Chapter 4 summarizes the main findings of this research. Aqueous and solid-phase geochemical data and additional SEM-EDS data from the tailings and the lake sediment that were not included within the main body of this thesis are included in the appendices.

References

Ahn, J. S., Park, Y. S., Kim, J. Y., Kim, K. W., 2005. Mineralogical and geochemical characterization of arsenic in an abandoned mine tailings of Korea. Environmental Geochemistry and Health 27, 147–157.

Al, T.A., Blowes, D. W., Jambor, J. L., Scott, J. D., 1994. The geochemistry of mine-waste pore affected by the combined disposal of natrojarosite and base-metal sulphide tailings at Kidd Creek, Timmins, Ontario. Canadian Geotechnical Journal 31, 502–512.

Amos, R. T., Blowes, D. W., Bailey, B. L., Sego, D. C., Smith, L., Ritchie, A. I. M., 2015. Waste-rock hydrogeology and geochemistry. Applied Geochemistry 57, 140–156.

Ball, J.W. and Nordstrom, D.K., 1991. WATEQ4F- user's manual with revised thermodynamic data base and test cases for calculating speciation of major, trace and redox elements in natural waters. In: US Geological Survey Open-File Report, 91–183.

Bao, Z., Al, T., Couillard, M., Poirier, G., Bain, J., Shrimpton, H. K., Finfrock, Y.Z., Lanzirotti, A., Paktunc, D., Saurette, E., Hu, Y., Ptacek, C.J., Blowes, D. W., 2021. A cross scale investigation of galena oxidation and controls on mobilization of lead in mine waste rock. Journal of Hazardous Materials 412, 125130.

Bao, Z., Al, T., Bain, J., Shrimpton, H. K., Finfrock, Y. Z., Ptacek, C. J., Blowes, D. W., 2022. Sphalerite weathering and controls on Zn and Cd migration in mine waste rock: An integrated study from the molecular scale to the field scale. Geochimica et Cosmochimica Acta 318, 1–18.

Benzaazoua, M., Bussière, B., Demers, I., Aubertin, M., Fried, É., Blier, A., 2008. Integrated mine tailings management by combining environmental desulphurization and cemented paste backfill: Application to mine Doyon, Quebec, Canada. Minerals Engineering 21, 330–340.

Blowes, D.W. and Jambor, J.L., 1990. The porewater geochemistry and the mineralogy of the vadose zone of sulfide tailings, Waite Amulet, Quebec, Canada. Applied Geochemistry 5, 327–346.

Blowes, D. W., Al, T., Lortie, L., Gould, W. D., Jambor, J. L., 1995. Microbiological, chemical, and mineralogical characterization of the Kidd Creek mine tailings impoundment, Timmins area, Ontario. Geomicrobiology Journal 13, 13–31.

Blowes, D. W., Ptacek, C. J., Jambor, J. L., Weisener, C. G., 2003. The Geochemistry of acid mine drainage. Treatise on Geochemistry 9, 149–204.

Bluteau, M. C. and Demopoulos, G. P., 2007. The incongruent dissolution of scorodite – solubility, kinetics and mechanism. Hydrometallurgy 87, 163–177.

Bussière, B., Aubertin, M., Chapuis, R. P., 2003. The behavior of inclined covers used as oxygen barriers. Canadian Geotechnical Journal, 40(3), 512–535.

Bussiere, B., Pabst, T., Boulanger-Martel, V., Guittonny, M., Plante, B., Neculita, C.M., Awoh, S., Mbonimpa, M., Demers, I., Maqsoud, A., Dimech, A., Labonte-Raymond, P.L., 2020. Monitoring the performance of mine site reclamation. In: Hard Rock Mine Reclamation - From prediction to management of acid mine drainage (Bussière and Guittonny, eds.), CRC Press, 384p.

CCME (Canadian Council of Ministers of the Environment), 1997. Canadian Water Quality Guidelines for the Protection of Aquatic Life.

CH2M HILL, 2014. Site Characterization report and data analysis - Long Lake Gold Mine tailings areas, Eden Township, Ontario. Final Technical Report prepared for Ontario Ministry of Northern Development and Mines.

Cummings, D. E., Caccavo, F., Fendorf, S., Rosenzweig, R. F., 1999. Arsenic mobilization by the dissimilatory Fe(III)-reducing bacterium Shewanella alga BrY. Environmental Science and Technology 33, 723–729.

DeSisto, S. L., Jamieson, H. E., Parsons, M. B., 2016. Subsurface variations in arsenic mineralogy and geochemistry following long-term weathering of gold mine tailings. Applied Geochemistry, 73, 81–97.

Drahota, P. and Filippi, M., 2009. Secondary arsenic minerals in the environment: A review. Environment International 35, 1243–1255.

Dudka, S. and Adriano, D. C., 1997. Environmental impacts of metal ore mining and processing: A Review. Journal of Environmental Quality 26(3), 590–602.

Esther, J., Sukla, L. B., Pradhan, N., Panda, S., 2015. Fe (III) reduction strategies of dissimilatory iron reducing bacteria. Korean Journal of Chemical Engineering 32, 1–14.

Fitton, G., 2014. X-ray fluorescence spectrometry. In: Modern Analytical Geochemistry – An introduction to quantitative chemical analysis for earth, environmental and material scientists (Robin, eds.), Routledge, 329p.

Flemming, R. L., Salzsauler, K. A., Sherriff, B. L., Sidenko, N. V., 2005. Identification of scorodite in fine-grained, high-sulfide, arsenopyrite mine-waste using micro X-ray diffraction (μXRD). Canadian Mineralogist 43, 1243–1254.

Fortin, D. and Beveridge, T. J., 1997. Microbial sulfate reduction within sulfidic mine tailings: formation of diagenetic Fe sulfides. Geomicrobiology Journal, 14, 1–21.

Gieré, R., Sidenko, N. V., Lazareva, E. V., 2003. The role of secondary minerals in controlling the migration of arsenic and metals from high-sulfide wastes (Berikul gold mine, Siberia). Applied Geochemistry 18, 1347–1359.

Gordon, J.B., Lovell, H.L., Grijs, Jan de, Davie, R.F., 1979. Gold deposits of Ontario, Part 2. Part of District Cochrane, Districts of Muskoka, Nipissing, Parry Sound, Sudbury, Timiskaming and counties of Southern Ontario; Ontario Geological Survey, Mineral Deposits Circular 18, 253p.

Gray, N. F., 1997. Environmental impact and remediation of acid mine drainage: A management problem. Environmental Geology 30, 62–71.

Hammarstrom, J. M. and Smith, K. S., 2002. Geochemical and mineralogic characterization of solids and their effects on waters in metal-mining environments. Progress on Geoenvironmental Models for Selected Mineral Deposit Types 8–54.

Hochella Jr., M.F., Moore, J.N., Golla, U., Putnis, A., 1999. A TEM study of samples from acid mine drainage systems: Metal–mineral association with implications for transport. Geochimica Cosmochimica Acta 63, 3395–3406.

Hogsden, K. L. and Harding, J. S., 2012. Consequences of acid mine drainage for the structure and function of benthic stream communities: A review. Freshwater Science 31, 108–120.

Hotton, G., Bussière, B., Pabst, T., Bresson, É., Roy, P., 2020. Influence of climate change on the ability of a cover with capillary barrier effects to control acid generation. Hydrogeology Journal 28, 763–779.

Hudson-Edwards, K. A., Schell, C., Macklin, M. G., 1999. Mineralogy and geochemistry of alluvium contaminated by metal mining in the Rio Tinto area, southwest Spain. Applied Geochemistry 14, 1015–1030.

Hudson-Edwards, K.A. and Santini, J.M., 2013. Arsenic-microbe-mineral interactions in mining-affected environments. Minerals 3, 337 – 351.

Ighalo, J. O., Kurniawan, S. B., Iwuozor, K. O., Aniagor, C. O., Ajala, O. J., Oba, S. N., Iwuchukwu, F.U., Ahmadi, S., Igwegbe, C. A., 2022. A review of treatment technologies for the mitigation of the toxic environmental effects of acid mine drainage (AMD). Process Safety and Environmental Protection 157, 37–58.

Jackson, L.M., Parbhakar-Fox, A., Gregory, D., Hughes, A., Agius, J., Ferguson, T., Lester, D., 2015. Evaluating the benefits of water covers as a rehabilitation strategy in temperate climates : A Tasmanian Perspective. 10th International Conference on Acid Rock Drainage and IMWA Annual Conference, 1–11.

Jamieson, H.E., 2011. Geochemistry and mineralogy of solid mine waste: Essential knowledge for predicting environmental impact. Elements 380–386.

Jamieson, H. E., Walker, S. R., Parsons, M. B., 2015. Mineralogical characterization of mine waste. Applied Geochemistry 57, 85–105.

Johnson, D. B. and Hallberg, K. B., 2003. The microbiology of acidic mine waters. Research in Microbiology 154, 466–473.

Kowalenko, C. G., 2001. Assessment of Leco CNS-2000 analyzer for simultaneously measuring total carbon, nitrogen and sulphur in soil. Communications in Soil Science and Plant Analysis 32, 2065–2078.

Lindsay, M. B. J., Moncur, M. C., Bain, J. G., Jambor, J. L., Ptacek, C. J., Blowes, D. W., 2015. Geochemical and mineralogical aspects of sulfide mine tailings. Applied Geochemistry 57, 157–177.

Lottermoser, B. G., 2010. Introduction to Mine Wastes. In Mine Wastes (Third ed.): Characterization, treatment and Environmental Impacts, Springer, 1–41.

Macy, J. M., Santini, J. M., Pauling, B. V., O'Neill, A. H., Sly, L. I., 2000. Two new arsenate/sulfate-reducing bacteria: mechanisms of arsenate reduction. Archives of Microbiology 173, 49–57.

Molson, J., Fala, O., Aubertin, M., Bussière, B., 2008. Geochemical transport modelling of acid mine drainage within heterogeneous waste rock piles. 61st Canadian Geotechnical Conference and 9th Joint CSG/IAH-CNC Groundwater Conference, Edmonton, Canada.

Moses, C. O., Nordstrom, D.K., Herman, J. S., Mills, A. L., 1987. Aqueous pyrite oxidation by dissolved oxygen and by ferric iron. Geochimica et Cosmochimica Acta 51, 1561–1571.

Neculita, C.M., Zagury, G. J., Bussière, B., 2007. Passive treatment of acid mine drainage in bioreactors using sulfate-reducing bacteria: Critical review and research needs. Journal of Environmental Quality 36, 1–16.

Newman, D. K., Ahmann, D., Morel, F. M. M., 1998. A brief review of microbial arsenate respiration. Geomicrobiology Journal 15(4), 255–268.

Nicholas, D. R., Ramamoorthy, S., Palace, V., Spring, S., Moore, J. N., Rosenzweig, R. F., 2003. Biogeochemical transformations of arsenic in circumneutral freshwater sediments. Biodegradation 14(2), 123–137.

Nordstrom, D. K., 1982. Aqueous pyrite oxidation and the consequent formation of secondary iron minerals. Acid Sulfate Weathering, 37–56.

Nordstrom, D. K., 2011. Hydrogeochemical processes governing the origin, transport and fate of major and trace elements from mine wastes and mineralized rock to surface waters. Applied Geochemistry 26, 1777–1791.

Nordstrom, D.K., Southam, G., 1997. Geomicrobiology of sulfide mineral oxidation. In: Geomicrobiology: Interactions between microbes and minerals (Banfield and Nelson, eds.), 35, Reviews in Mineralogy 361 -390.

Öhlander, B., Chatwin, T., Alakangas, L., 2012. Management of sulfide-bearing waste, a challenge for the mining industry. Minerals 2, 1–10.

Oremland, R.S. and Stolz, J.F., 2003. The ecology of arsenic. Science 300, 939 – 944.

Parbhakar-Fox, A., Lottermoser, B.G., 2015. A critical review of acid rock drainage prediction methods and practices. Minerals Engineering 82, 107–124.

Park, I., Tabelin, C. B., Jeon, S., Li, X., Seno, K., Ito, M., Hiroyoshi, N., 2019. A review of recent strategies for acid mine drainage prevention and mine tailings recycling. Chemosphere 219, 588–606.

Parkhurst, D.L. and Appelo, C.A.J., 1999. User's guide to PHREEQC (Version 2)- a computer program for speciation, batch-reaction, one-dimensional transport, and inverse geochemical calculations. In: U.S. Geological Survey, Water Resources Investigations Report 99-4259, 312p.

Parviainen, A., 2009. Tailings mineralogy and geochemistry at the abandoned Haveri Au-Cu mine, SW Finland. Mine Water and the Environment 28, 291–304.

Perreault, N. N., McKinnell, R. J., Delisle, S., 2015. Tailings , managing for the future. Proceedings Tailings and Mine Waste, October 26 - 28, Vancouver, B.C.

Petrunic, B. M. and Al, T. A., 2005. Mineral/water interactions in tailings from a tungsten mine, Mount Pleasant, New Brunswick. Geochimica et Cosmochimica Acta 69, 2469–2483.

Petrunic, B. M., Al, T. A., Weaver, L., 2006. A transmission electron microscopy analysis of secondary minerals formed in tungsten-mine tailings with an emphasis on arsenopyrite oxidation. Applied Geochemistry 21, 1259–1273.

Petrunic, B. M., Al, T. A., Weaver, L., Hall, D., 2009. Identification and characterization of secondary minerals formed in tungsten mine tailings using transmission electron microscopy. Applied Geochemistry 24, 2222–2233.

Revesz, E., Fortin, D., Paktunc, D., 2015. Reductive dissolution of scorodite in the presence of Shewanella sp. CN32 and Shewanella sp. ANA-3. Applied Geochemistry 63, 347–356.

Rimstidt, D. D. and Vaughan, D. J., 2003. Pyrite oxidation: A state-of-the-art assessment of the reaction mechanism. Geochimica et Cosmochimica Acta 67, 873–880.

Roussel, C., Néel, C., Bril, H., 2000. Minerals controlling arsenic and lead solubility in an abandoned gold mine tailings. Science of the Total Environment 263, 209–219.

Salzsauler, K. A., Sidenko, N. V., Sherriff, B. L., 2005. Arsenic mobility in alteration products of sulfide-rich, arsenopyrite-bearing mine wastes, Snow Lake, Manitoba, Canada. Applied Geochemistry 20, 2303–2314.

Sapkota, B., Verbuyst, B., Bain, J., Ptacek, C., Blowes, D., Al, T., 2023. Geochemical and mineralogical investigation of cemented crusts in the tailings cover at Long Lake Gold Mine, Sudbury, Canada. Journal of Hazardous Materials 451, 131192.

Seal, R. R., Hammarstrom, J. M., Johnson, A. N., Piatak, N. M., Wandless, G. A., 2008. Environmental geochemistry of a Kuroko-type massive sulfide deposit at the abandoned Valzinco mine, Virginia, USA. Applied Geochemistry 23, 320–342.

Schindler, M. and Singer, D.M., 2017. Mineral surface coatings: environmental records at the nanoscale. Elements 13, 159–164.

SNC-Lavalin, 2016. Long-term monitoring well installation and groundwater assessment report, 624398-0000-4GCC-0008-PB. Prepared for Ministry of the Northern Development Mines, Ontario.

Szczepańska, J. and Twardowska, I., 2004. Mining waste. In: Waste Management Series 4; Solid Waste: Assessment, Monitoring and Remediation (Twardowska, Kettrup and Lacy, eds.), 319–385.

Vriens, B., Plante, B., Seigneur, N. and Jamieson, H., 2020. Mine waste rock: Insights for sustainable hydrogeochemical management. Minerals 10, 1–38.

Walker, S. R., Parsons, M. B., Jamieson, H. E., Lanzirotti, A., 2009. Arsenic mineralogy of near-surface tailings and soils: Influences on arsenic mobility and bioaccessibility in the Nova Scotia gold mining districts. Canadian Mineralogist 47, 533–556.

Williams, D., 2020. The role of technology and innovation in improving tailings management. Towards Zero Harm: A Compendium of Papers Prepared for the Global Tailings Review. Available online: https://globaltailingsreview. org/wpcontent/uploads/2020/09.

Winter, L.D.S., 1986. Geological report on the Eden Township Property, District of Sudbury, Ontario. Prepared for Loki Resources Inc.

Wunderly, M. D., Blowes, D. W., Frind, E. O., Ptacek, C. J., 1996. Sulfide mineral oxidation and subsequent reactive transport of oxidation products in mine tailings impoundments: A numerical model. Water Resources Research 32, 3173–3187.

Zhang, H., Penn, R. L., Hamers, R. J., Banfield, J. F., 1999. Enhanced adsorption of molecules on surfaces of nanocrystalline particles. Journal of Physical Chemistry B 103, 4656–4662.

CHAPTER TWO

GEOCHEMICAL AND MINERALOGICAL INVESTIGATION OF CEMENTED CRUSTS IN THE TAILINGS COVER AT LONG LAKE GOLD MINE, SUDBURY, CANADA[1]

[1]Reprinted with permission from Journal of Hazardous Materials:
Sapkota, B., Verbuyst, B., Bain, J., Ptacek, C., Blowes, D., Al, T., 2023. Geochemical and mineralogical investigation of cemented crusts in the tailings cover at Long Lake Gold Mine, Sudbury, Canada. Journal of Hazardous Materials 451, 131192.

Abstract

In mine tailings, precipitation of secondary minerals may cement the tailings material and form cemented crusts or hardpans. Hardpans typically form beneath the surface of reactive tailings. However, at the former Long Lake Gold Mine near Sudbury, Ontario, cemented crusts formed in a clean sand cover above the tailings. We applied mineralogical and geochemical techniques to investigate the formation of these cemented crusts. Representative samples were collected from the sand cover and vertical cores from the underlying tailings. Elevated concentrations of arsenic (As), iron (Fe), and sulfur (S) in the sand cover indicate the upward transport of sulfide-mineral oxidation products. The shallow porewater of the tailings is acidic (pH 4 – 6) and contains elevated concentrations of As (up to 346 mg/L), Fe (up to 1844 mg/L), and SO_4 (up to 12,000 mg/L). Mineralogical observations indicate that primary sulfide minerals in the near-surface tailings display moderate to strong oxidation, and secondary Fe-arsenate and jarosite minerals are formed both in the near-surface tailings and the sand cover. Upward migration of sulfide-mineral oxidation products leads to the formation of cemented crusts, which with continuing erosion, represent a long-term source of pollution to the surrounding environment.

Keywords: Mine tailings; Sulfide oxidation; Secondary minerals; Capillarity; Hardpans

2.1. INTRODUCTION

Metal mining generates a large volume of mine waste because only a small fraction of the ore has economic value. The majority of mined and processed material is rejected as waste rock, tailings, and slag (Lottermoser, 2010). Historically, mine tailings were routinely dispersed along watercourses, and impounded in low-lying areas close to the mills (Walker et al., 2009), which were inexpensive and operationally easy disposal methods, but were ecologically disruptive (Pedersen and Losher, 1988). Tailings disposed of in this way can cause severe environmental impacts, primarily from acid mine drainage (AMD) (Jambor et al., 2005; Heikkinen et al., 2009).

In sulfide-bearing tailings, oxidation and hydrolysis reactions are responsible for chemical weathering of sulfide minerals and mobilization of oxidation products (e.g., AsO_4^{3-}, H^+, $Fe(OH)_3$, SO_4^{2-}) (Nesbitt et al., 1995; Wunderly et al., 1996; Bain et al., 2000; Rimstidt and Vaughan, 2003). Some of these oxidation products may represent sources of contamination to the environment. Their aqueous concentrations may be attenuated by adsorption on mineral surfaces or precipitation and coprecipitation with secondary minerals that precipitate directly from porewater or remain following incongruent dissolution of primary minerals (Petrunic et al., 2009). When secondary minerals cement the tailings, physically dense indurated layers form, referred to as 'hardpans' (Blowes et al., 1991). Hardpans, generally characterized by relatively low porosities and hydraulic conductivities compared to initial tailings (Ahn et al., 2011), can act as barriers against water infiltration and oxygen ingress, thereby, reducing the oxidation rates in the underlying tailings (Gilbert et al., 2003). Several studies (e.g., Blowes et al., 1991; Blowes et al., 1998; Moncur et al., 2005; Alakangas and Öhlander, 2006; Graupner et al., 2007; DeSisto et al., 2011; Liu et al., 2018; Elghali et al., 2019; Liu et al., 2019) have described the mechanisms of hardpan formation beneath the surface of reactive tailings, commonly at the oxic-anoxic boundary region in sulfidic-mine

wastes. Hardpan formation generally involves weathering of primary minerals at shallow depths where oxygen is readily available, downward transport (diffusive or advective) of dissolved constituents, precipitation of secondary minerals, and cementation of tailings material. In sulfidic-mine wastes, frequently reported cementing minerals include Fe-oxyhydroxide, jarosite, gypsum, scorodite, and Fe-arsenate (Alakangas and Öhlander, 2006; Graupner et al., 2007; Murciengo et al., 2019).

In addition to downward transport, studies have also demonstrated the role of capillarity in driving upward migration of aqueous solutes, leading to the formation of cemented crusts near the surface. For example, Acero et al. (2007) studied the evolution of pyrite-rich tailings in unsaturated column experiments simulating sub-arid conditions and showed that cemented crusts develop on the top surface of the columns at the end of the evaporation experiment (125 days). Dold and Fontbote (2001) studied mineralogical and geochemical changes at the interface between oxidized and unoxidized zones in copper-mine tailings, and how climatic conditions could influence the transport pathways of oxidation products. These studies suggest that in uncovered reactive tailings, prolonged dry seasons can contribute to an upward rise of solutes and precipitation of secondary minerals at the tailings surface. Similarly, numerical simulation studies (e.g., Molson et al., 2005; Pedretti et al., 2015) have demonstrated that geochemical processes and solute transport driven by capillarity could promote the formation of cemented crusts in the unsaturated zone in waste-rock dumps.

Laboratory leaching tests (Benzaazoua et al., 2004; Elghali et al., 2019) and numerical hydrogeochemical assessments (Pabst et al., 2018; Larochelle et al., 2019) have assessed the impact of capillarity in different reclamation options, including monolayer and two-or three-layer dry covers that utilize the capillary barrier effect (CBE). A typical three-layer cover with CBE is

composed of a fine-grained, moisture-retaining layer between two layers of coarse-grained materials. The bottom coarse-grained layer acts as a capillary break (prevents water rise), and the top layer limits water loss by evaporation, thereby, allowing the middle moisture-retaining layer to remain at near-saturation and function as a barrier against oxygen diffusion to the underlying tailings (Bussière et al., 2004 and references therein). Dry cover materials designed to utilize the CBE have been used at several mine sites to limit sulfide oxidation (Dagenais et al., 2005). For example, Bussière et al. (2006) monitored the performance of the cover implementing CBE at LTA impoundment near Malartic, Quebéc, and they found that the cover was successful in limiting oxygen diffusive flux reaching the underlying sulfide tailings. An investigation of thickened tailings by Al and Blowes (1999) demonstrated that capillarity contributes to the formation of a thick tension-saturated zone (up to 5 to 6 m) above the water table which limits the thickness of unsaturated tailings and consequently reduces the depth of sulfide oxidation.

At the former Long Lake Gold Mine (Fig. 2.1) near Sudbury, Ontario, cemented crusts, which are precursors to hardpans, have developed in a sand layer overlying the tailings. The sand layer was placed on the tailings in the early 1970s, nearly 30 years after the mine was abandoned, in a remediation attempt intended to prevent erosion and transport of the As-rich tailings to the surrounding environment, and to slow the rate of sulfide oxidation (CH2M HILL, 2014). However, the capillary rise of contaminated tailings porewater led to the precipitation of secondary minerals that cemented the sand particles. Erosion and transport of the cover material by surface water runoff represent a risk to the surrounding environment. The degree of risk posed by the situation is partly contingent on the chemical composition and stability of the cementing minerals.

Whereas previous studies focused on the role of capillarity in promoting upward transport of solutes and the implications for tailings management, there is limited literature documenting the

geochemical and mineralogical processes controlling the formation of cemented crusts or hardpans on tailings surfaces and in cover materials. The overall objective of this study was to investigate the extent of sulfide-mineral oxidation and secondary-mineral precipitation in a historic mine site at Long Lake, specifically to characterize the nature and distribution of cemented crusts in the sand cover in the context of environmental risk due to erosion and transport of the sand cover.

2.2. SITE DESCRIPTION

The former Long Lake Gold Mine is located approximately 17 km southwest of the city of Sudbury (Fig. 2.1). The gold deposit was discovered in 1907 and consisted mainly of gold-bearing pyrite and arsenopyrite in quartz veins hosted in quartzite (Winter, 1986). The open pit and underground mine operated intermittently from 1908 until the main arsenopyrite-bearing ore zone was mined out and abandoned in 1939 (Gordon et al., 1979). Approximately 200,487 tonnes of ore were milled at a grade of 8.1 g/tonne (CH2M HILL, 2014). During operations, an estimated 163,000 m^3 of tailings were discharged directly into topographic depressions without additional containment. The tailings areas consist of three interconnected areas (TA-01, TA-02, and TA-03); TA- 01 has the largest surface area (7.1 ha) of the three. A creek flows through the tailings impoundments (Figs. 2.1 and 2S.1). The transport of tailings-derived solids downstream into Long Lake, via Luke Creek, has formed a sediment delta at the mouth of the creek. Sulfide-bearing minerals in the tailings were exposed to the environment for nearly 30 years before a sand cover (~ 0.3 m thick) was applied in the early 1970s by the Government of Ontario (CH2M HILL, 2014). Since the cover placement, portions of the sand cover have eroded, exposing the tailings at several locations.

Surface water-quality monitoring (1976 to 1989) by the Government of Ontario identified aqueous As concentrations that exceed the Canadian Council of Ministers guideline of 5 µg/L for

the protection of freshwater aquatic life (CCME, 1997). Similarly, groundwater assessment performed by SNC-Lavalin (2016) at TA-01 identified exceedances of As in most of the samples.

The Long Lake area has a continental climate, with hot summer and cold winter (approximate seasonal range from -23 to 28 ºC). Precipitation occurs throughout the year. The average annual rainfall ranges between 523 and 900 mm/year, and the average annual precipitation ranges between 660 and 1114 mm/yr (data from Sudbury, Ontario between 2000 and 2012, http://climate.weather.gc.ca).

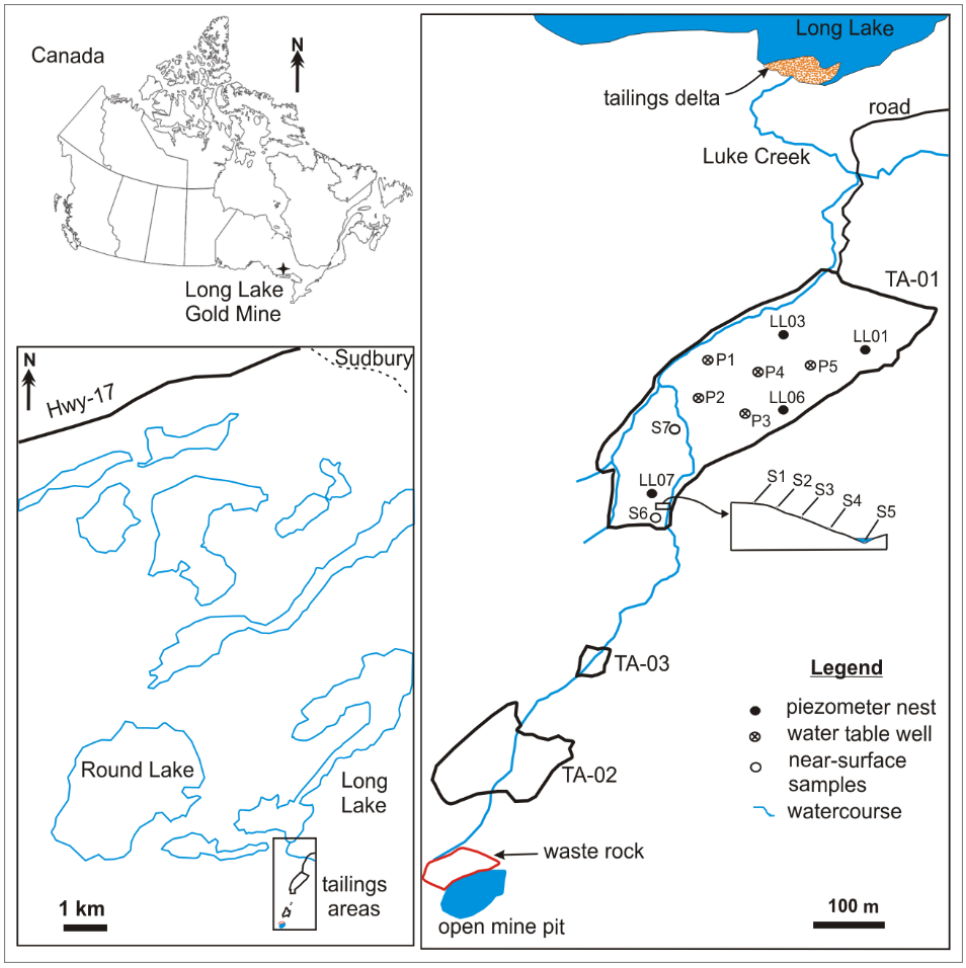

Fig. 2.1. (Left) Location of the former Long Lake Gold Mine, with inset showing locations of tailings areas and the southern end of Long Lake. (Right) Sample locations within TA-01, and the surrounding area.

2.3. MATERIALS AND METHODS

2.3.1. Hydrogeology

A network of 23 drive-point piezometers was installed in four nests (LL01, LL03, LL06, and LL07) at TA-01 (Fig. 2.1). Each nest contains five to six piezometers and one to two suction lysimeters. Five single, shallow water-table wells (P1 to P5; Fig. 2.1) were used to define the depth to the water table and determine the groundwater flow direction. Hydraulic head measurements were conducted eight times between June 2017 and July 2019.

2.3.2. Tailings geochemistry

A set of vertical cores (0.051 m diameter, maximum depth of 4.1 m), one from each of the four nested piezometer locations (Fig. 2.1), was collected in December 2016. The cores transected three stratigraphic units: the sand cover, tailings, and the underlying natural sediment. These cores allow for an assessment of the effect of vertical solute transport processes on the geochemical and mineralogical evolution of the system. The cores were immediately sealed and transported with minimal disturbance to the laboratory to preserve spatial and stratigraphic relationships among the solids. The cores were split in half length-wise; one half was used for mineralogical investigations and the second half was used for geochemical analysis. The cores for geochemical analysis were dried in air and pulverized using a mortar and pestle. Solid samples from LL03 and LL06 from the sand cover (n = 4), tailings (n = 19), and natural sediment (n = 7) were submitted for whole-rock analyses to Activation Laboratories, Ancaster, Ontario. Powdered samples were fused at 750 °C with sodium peroxide and the fusion cakes were dissolved in dilute nitric acid. The resulting solutions were analyzed by Inductively-Coupled Plasma Optical-Emission Spectroscopy (ICP-

OES). The total sulfur content was determined by LECO induction furnace with an infrared detector.

2.3.3. Aqueous geochemistry

Groundwater from the saturated zone was collected from the piezometer network using a peristaltic pump. Samples from the unsaturated zone were collected using suction lysimeters and by extracting porewater from four vertical cores obtained at the piezometer nest locations. The cores (0.076 m diameter, maximum depth of 1.3 m) were collected in December 2016 using the piston-barrel method described by Starr and Ingleton (1992). They were cut into lengths of 0.25–0.45 m and squeezed using a hydraulic press to recover porewater directly into syringes, following the method described by Moncur et al. (2013). The samples were analyzed in the field immediately upon collection for pH (Orion Ross Ultra pH electrode; Model 8156BNUWP), redox potential (Orion Platinum redox electrode; Model 9678BNWP), and total alkalinity. The performance of the redox electrode was checked with ZoBell's solution (Nordstrom, 1977) and the values were referenced to the standard hydrogen electrode (Eh). Water samples for total alkalinity measurements were filtered through 0.45 μm cellulose-acetate membranes and titrated using a Hach Digital Titrator with 0.16 N or 1.6 N sulfuric acid and bromocresol green-methyl red indicator. Samples for geochemical analysis were also filtered (0.45 μm cellulose acetate) and those for cation determination were acidified to pH < 2.0 using trace-metal-grade nitric acid and analyzed by ICP-OES and Inductively-Coupled Plasma Mass Spectrometry (ICP-MS). Anion concentrations (Cl^-, Br^-, F^-, NO_2^-, NO_3^-, PO_4^{3-}, and SO_4^{2-}) were determined by Ion Chromatography (IC).

2.3.4. Geochemical modeling

Aqueous geochemical modeling was performed using PHREEQC 3.6.1 (Parkhurst and Appelo, 1999) with the WATEQ4F database (Ball and Nordstrom, 1991) to speciate porewater and calculate mineral saturation indices (SI), thereby, allowing an assessment of the tendency for mineral phases to precipitate or dissolve. Redox speciation was performed using the corrected Eh measurements. Results from the geochemical modeling were used to assess the potential for precipitation of secondary As-and Fe-bearing minerals.

2.3.5. Mineralogy

2.3.5.1. Sample collection and preparation

Thin cemented crusts were observed at the surface along a cross-section of a stream bank in tailings area TA-01; the crusts apparently formed from the precipitation of dissolved solutes where groundwater seepage occurs along the slope of the stream bank. Five samples (S1 – S5) were collected on the sloping stream bank along with two additional crust samples (S6 and S7) of cemented surficial sand (Fig. 2.1). Together with the vertical cores described above, the surface crust samples allow for a comparison between cemented crusts formed by capillarity-driven vertical transport (core samples) and crusts formed by the discharge of phreatic groundwater.

The cores used for mineralogical investigations were dried in a nitrogen-purged anaerobic chamber to prevent oxidation of ferrous-iron and sulfide-bearing minerals. The surface crust samples were air-dried in the laboratory at room temperature. All samples were impregnated with low-viscosity epoxy resin (EPO-TEK 301 2FL) and petrographic thin sections (~100 μm thick) were prepared using kerosene for polishing.

2.3.5.2. Mineralogical analyses

Cross-scale mineralogical techniques were used to examine the extent of sulfide-mineral oxidation, and the formation of secondary minerals in the tailings, sand cover, and the natural sediment that underlies the tailings. The sand cover and the tailings were sampled and analyzed by powder X-ray diffraction (XRD; University of Ottawa). Prior to the analysis of samples containing cemented crusts, secondary-mineral cements were pre-concentrated using an autogenous grinding technique to detach secondary minerals which were collected by sieving (<52 μm nylon) and then powdered using a mortar and pestle. The diffractometer (Rigaku Ultima IV) was operated with CuKα radiation generated at 40 kV and 44 mA. A 10-mm divergence slit was used on the incident beam and diffraction patterns were recorded from 10 to 65º 2θ with scan speeds of 0.5 or 0.25 deg/min. Mineral identification was conducted using the program Match! (Crystal Impact, Bonn, Germany) and the Crystallography Open Database (https://www.crystallography.net/cod/).

Thin sections were examined by optical microscopy under reflected light. The features of interest, predominantly the oxidized sulfide-mineral grains and secondary minerals, were first located by optical microscopy and then examined in detail using Scanning Electron Microscopy (SEM, JEOL 6610LV) coupled with Energy-Dispersive X-ray Spectroscopy (EDS, Oxford Instruments INCA). Chemical compositions of representative secondary minerals from the cemented crusts were quantitatively determined with a JEOL JXA-8230 Electron Microprobe (EMP; University of Ottawa). The EMP instrument is equipped with five tunable wavelength dispersive spectrometers and was operated at 15 kV and 5 nA. Spot analyses of Al, As, Ca, Cu, Fe, Na, K, Si, S, and Ti were performed on carbon-coated polished sections. Data collection time was 20 s for all elements and for background positions (off-peak) on either side of the main peak

position. The raw data were corrected for atomic number, absorption, and fluorescence effects (ZAF) by the modified Phi-Rho-Z procedure (Armstrong, 1988).

Four Transmission Electron Microscope (TEM) samples (~ 10 μm x 30 μm) were prepared directly from petrographic thin sections using a focused ion beam (Ga ion source) at Fibics Incorporated, Ottawa, Ontario. A JEOL JEM-2100F analytical Scanning Transmission Electron Microscope (STEM; University of Ottawa) equipped with annular dark-field and bright-field detectors was used for imaging and characterization of the composition of secondary phases. Selected-area electron diffraction (SAED) was conducted at the National Research Council of Canada on a FEI Titan 80-300 TEM operated at 300 keV.

2.4. RESULTS

2.4.1. Hydrogeology

The water table at P1 to P5, and in the shallow piezometers at each nest, ranged from 0.02 to 1.3 meters below ground surface (mbgs) between October 2018 and July 2019, with the highest water table positions recorded during October-November and the lowest in July. The average water table positions were highest (242.82 meters above sea level; masl) in the southwest area close to LL07 and lowest (239.56 masl) in the north, close to LL03, indicating that the groundwater flows north toward Long Lake. The vertical hydraulic gradients ranged from -0.87 (downward) to 1.1 (upward) (average 0.02), suggesting a seasonal variation, with a uniformly upward gradient during measurement periods in June, July, and September, and a downward gradient during October and November at all four locations.

2.4.2. Tailings geochemistry

Depth-profiles for the elements contained in common carbonate, silicate, and primary sulfide minerals are plotted (Fig. 2.2) for samples from LL03 and LL06. The concentrations of As, Fe, and S in the tailings below 0.7 m (i.e., below the sand-tailings interface) are relatively high, and their concentrations gradually decrease with the transition upward to the shallow tailings. For example, at LL06, As concentrations decrease from 3.16 to 1.02 wt.%, Fe from 8.11 to 2.83 wt.%, and S from 5.34 to 0.34 wt.%. Similarly, at LL03, As concentrations decrease from 3.53 to 0.37 wt.%, Fe from 8.12 to 1.04 wt.%, and S from 7.69 to 0.61 wt.%. In the sand cover at LL06, the concentrations of As, Fe, and S are similar to those in the shallow tailings, but at LL03, there is a slight increase in Fe and S concentrations and a decrease in As concentrations relative to the shallow tailings. In the natural sediment below the tailings, As and S concentrations decrease sharply to < 0.1 wt.%, whereas Fe concentrations decrease more gradually to near constant values between 3 and 4 wt.%. The Ca and Mg concentrations are low (< 0.2 wt.%) in the sand cover but gradually increase in the tailings and are highest in the sediment. The concentrations of Si (16.9 to 35.5 wt.%) and Al (3.75 to 6.67 wt.%) are near constant throughout the depth profiles. The concentration of K (0.3 – 0.7 wt.%) is constant through the sand cover and tailings but increases up to ~2 wt.% in the underlying sediment.

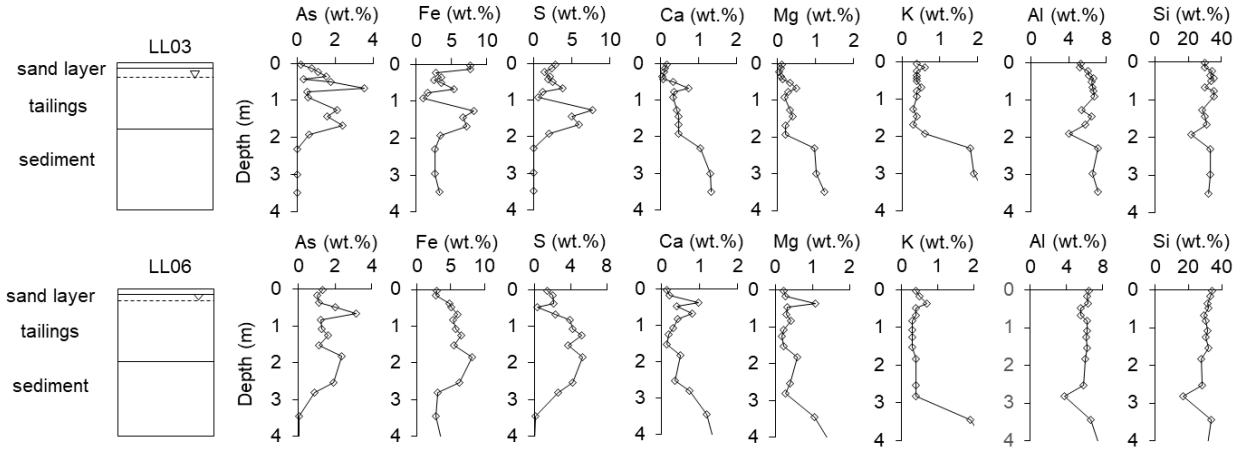

Fig. 2.2. Solid-phase geochemistry profiles for locations LL03 and LL06. Average water table depths are indicated by the dashed lines in the stratigraphic columns (left).

2.4.3. Aqueous geochemistry

The aqueous geochemical depth profiles for LL03 and LL06 are presented in Figure 2.3. The pH values in the porewater from the sand layer and the shallow tailings are < 4.0 at LL03 and between 4 and 6.7 at LL06 but are near neutral at a greater depth at both locations. The Eh measurements indicate relatively oxidizing conditions at the surface (517 to 789 mV at LL03, and 148 to 303 mV at LL06) and a decreasing trend with depth (71 to 366 mV at LL03, and 71 to 267 mV at LL06). Alkalinity concentrations are relatively low in the sand layer and the shallow tailings (< 100 mg/L as $CaCO_3$), and higher in the deep tailings (up to 460 mg/L as $CaCO_3$). The concentrations of SO_4^{2-} and dissolved major (Al, As, Ca, Fe, K, Mg, Na, Si) and trace (Cu, Ni, Zn) elements show a trend of relatively high concentrations in the upper portion of the tailings and a gradual decrease with depth. For example, the porewater collected at 0.5 mbgs from LL03 in June 2018 has As, Fe, and SO_4^{2-} concentrations of 346, 2326, and 12,000 mg/L, respectively, and at 1.86 mbgs, their respective concentrations are 7.4, 1032, and 4005 mg/L. Below the tailings, As, Fe,

and SO_4^{2-} concentrations range from < 1.0 to 15 mg/L, 1.0 to 403 mg/L, and 2.8 to 2500 mg/L, respectively.

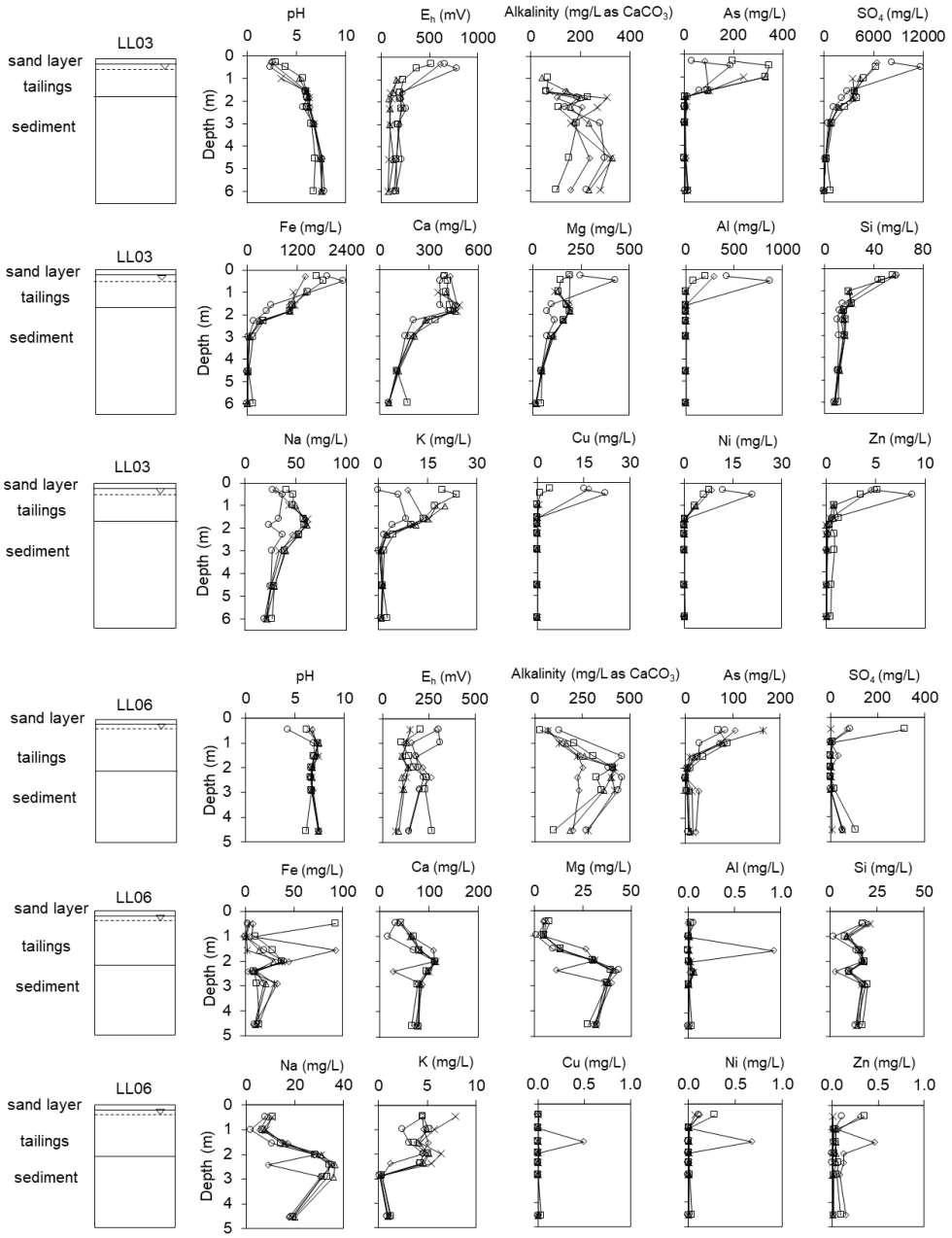

Fig. 2.3. Depth profiles of groundwater geochemistry for locations LL03 and LL06 from various sampling episodes: December 2016 (□), June 2017 (◊), September 2017 (X), November 2017 (Δ), and June 2018 (O).

Saturation indices of selected phases obtained from geochemical modeling of porewater data from two sampling episodes (June and November 2017) at LL03 and LL06 are presented in Figure 2.4. The porewater in the sand cover at LL03 is undersaturated with respect to all of the selected phases except goethite [α- FeOOH]. The porewater in the tailings at both locations remains slightly supersaturated with respect to ferrihydrite [$5Fe_2O_3.9H_2O$; as $Fe(OH)_3$ in the WATEQ4F database], alunite [$KAl_3(SO_4)_2(OH)_6$], gibbsite [$Al(OH)_3$], and goethite, and undersaturated with respect to scorodite [$FeAsO_4.2H_2O$] and jarosite [$KFe_3(SO_4)_2(OH)_6$]. For calcite [$CaCO_3$] and dolomite [$CaMg(CO_3)_2$], the porewater in the shallow tailings is undersaturated but approaches near-equilibrium with respect to these phases at greater depth.

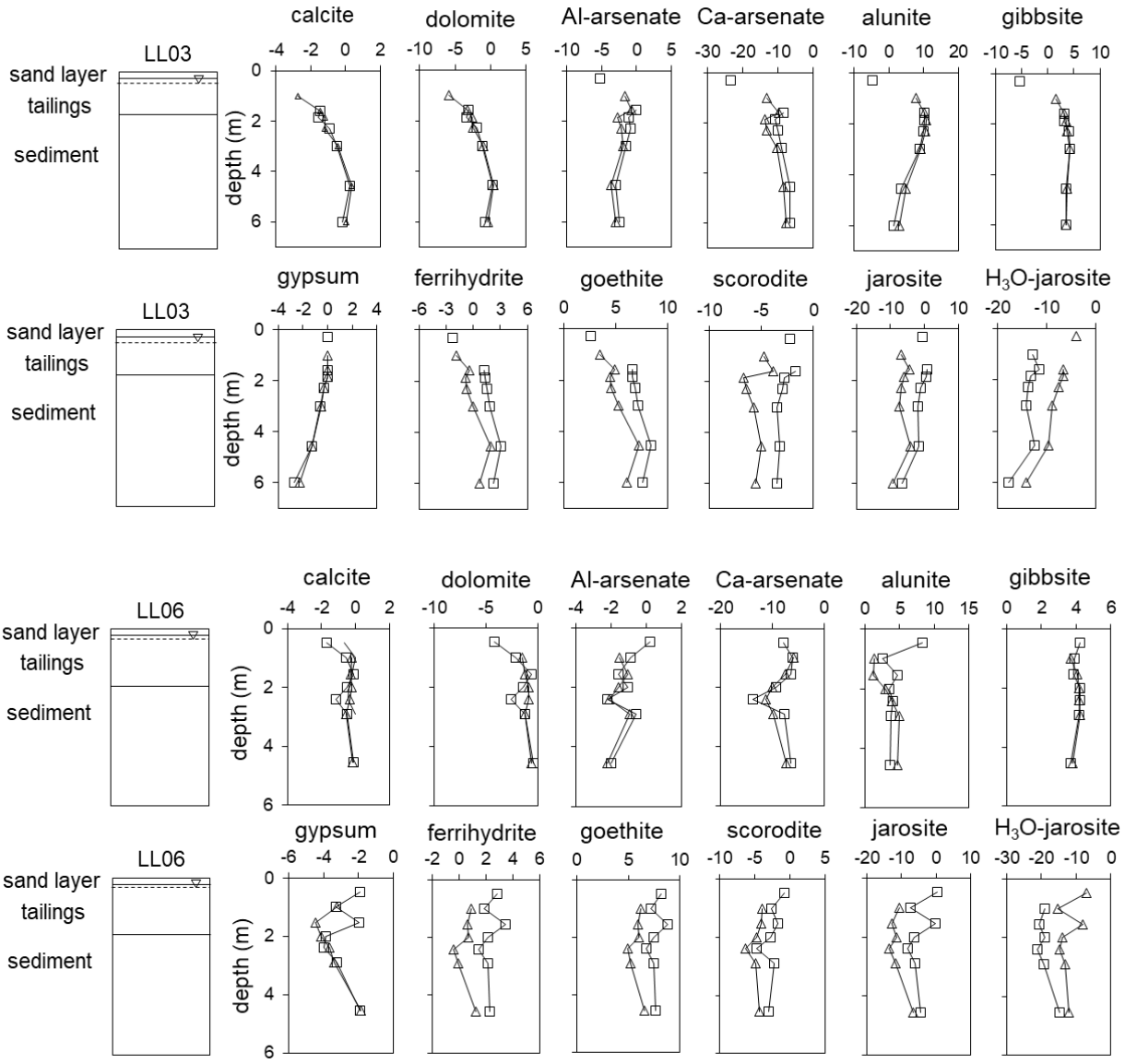

Fig. 2.4. Depth profiles of saturation indices for selected phases at locations LL03 and LL06. Symbols Δ and □ correspond to groundwater sampled in June 2017 and November 2017, respectively.

2.4.4. Mineralogy

2.4.4.1. Field-scale observation

Red-brown to yellow-orange crusts (Figs. 2.5, S2.1) are present in the sand layer throughout the tailings area TA-01. The crusts (Fig. 2.5A, B) that are located on the upper, relatively flat surface of the tailings where the sand cover has not been completely eroded, are relatively thick (cm-scale) and discontinuous. In the sloping areas at the sides of drainage channels where the sand cover has been eroded, the crusts (Fig. 2.5C) form at the surface and are relatively thin (mm-scale).

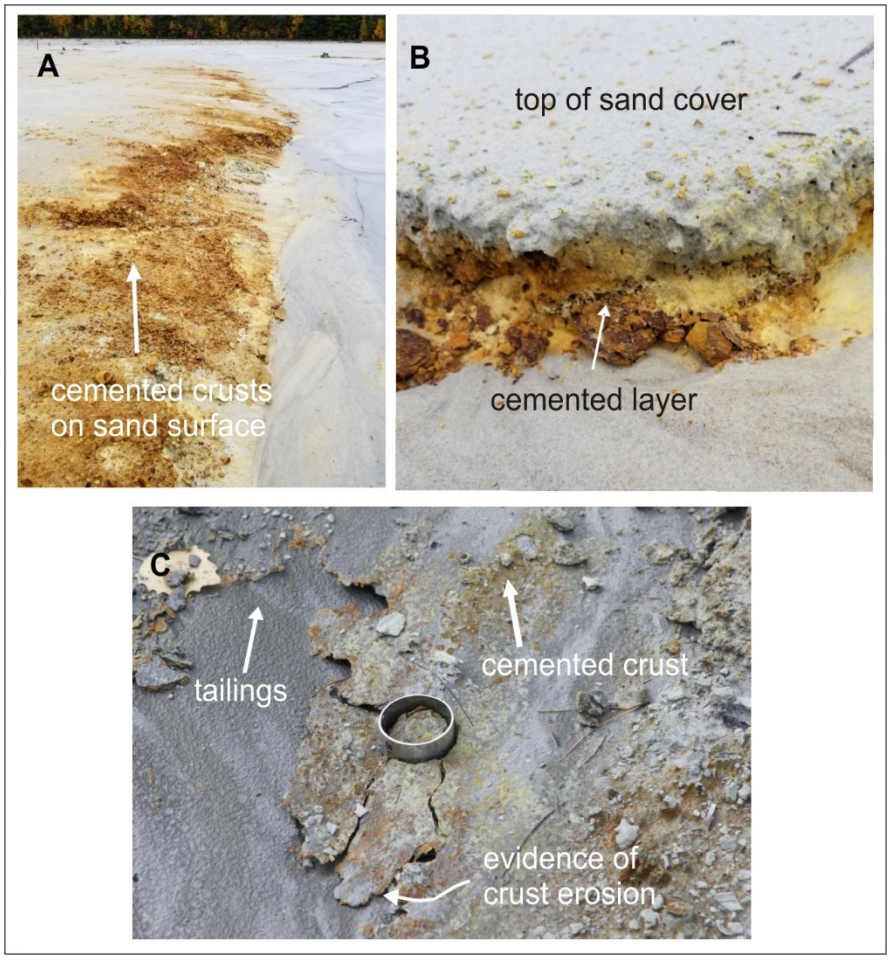

Fig. 2.5. Cemented crusts at TA-01: (A, B) discontinuous crusts in the sand cover at S7; (C) thin, partially eroded crusts on the tailings surface at S2.

2.4.4.2. Microscale characterization

2.4.4.2.1. Tailings

XRD analyses indicate that the tailings contain pyrite as the principal sulfide mineral, and quartz and albite as the dominant silicate minerals. Quartz (32 – 45%) and albite (55 – 61%) constitute the majority of the tailings samples while pyrite is present in low abundance (< 2%). The XRD results represent samples collected from two locations (LL03 and LL06) and through the entire depth of the tailings at each location. The results should therefore represent the bulk mineralogical composition of the tailings through time as they were deposited. The data suggest that the bulk mineralogy has been constant through time.

SEM analyses indicate that at depths > 0.7 m below the sand-tailings interface, the tailings are mostly unoxidized and the sulfide minerals show little indication of alteration, while at < 0.7 m depth below the interface, they display moderate to high degrees of alteration (Fig. 2.6) with irregular and pitted outlines and secondary-mineral coatings. Although not detected by XRD, SEM analyses indicate the presence of small amounts of arsenopyrite, which display more advanced weathering features than pyrite, with thick coatings surrounding highly weathered grains. The secondary-mineral precipitation in the shallow tailings ranges from coatings on sulfide minerals due to incongruent oxidative dissolution to accumulations of particles and coatings in the pore space. The EDS analyses on the secondary minerals in the tailings indicate that the dominant phase has a Fe-As-O composition (Fig. 2.6).

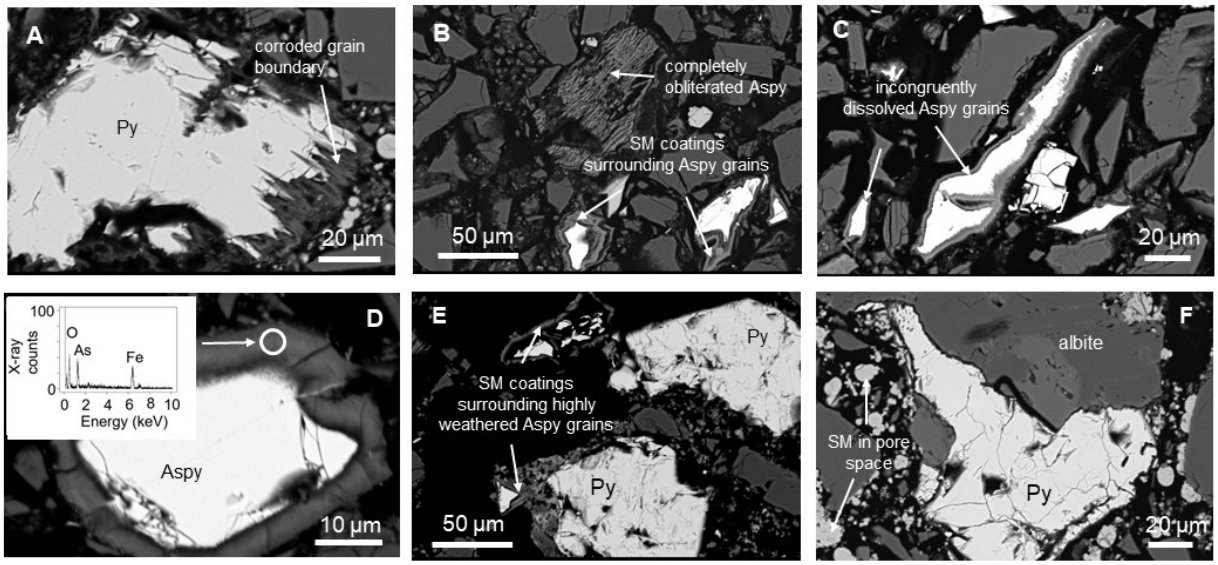

Fig. 2.6. Backscattered images illustrating textures of variably weathered pyrite (Py) and arsenopyrite (Aspy) grains. The incongruently-dissolved sulfide minerals have secondary mineral (SM) coatings of variable thickness, and the dominant phase consists of Fe-As-O composition. The Aspy grain in bottom centre of panel B was investigated further with (S)TEM (Fig. 2.9).

2.4.4.2.2. Cemented crusts in sand cover

The solutes that result from the oxidative dissolution of sulfide minerals could migrate both upward toward the sand cover or down to the deeper tailings and natural sediment. The solutes that were transported to the sand cover precipitated and partially to completely filled the pore space, forming cements between the grains. The SEM-EDS analyses of the cements indicate that the secondary-mineral precipitates have four principal chemical compositions; Fe-As-O, Fe-As-S-O, Fe-S-O-K/Na, and Fe-O, indicating the presence of ferric-arsenate, ferric-arsenate sulfate, K/Na-jarosite, and Fe-oxyhydroxide, respectively (Figs. 2.7 and 2.8). Ferric-arsenate and jarosite minerals are the most commonly observed in the samples while Fe-arsenate sulfate and Fe-

oxyhydroxide are less common. The results of EMP analysis (Table 2.1) of the secondary minerals in the cemented crusts are consistent with the SEM-EDS analyses. For example, both SEM-EDS and EMP analyses indicate that the cementing material at S2 is primarily composed of As, Fe, O, and S. Although the amount of S varies from 1.5 to 10 wt.%, Fe:As molar ratios range between 0.99 and 1.36, consistent with scorodite ($FeAsO_4 \cdot 2H_2O$). The analyses of crusts from S7 and LL03 suggest the presence of a solid solution between jarosite [$KFe_3(SO_4)_2(OH)_6$] and its sodium analog, natrojarosite [$NaFe_3(SO_4)_2(OH)_6$], with As_2O_5 contents ranging from 0.33 to 1.72 wt.%. The EMP analyses of the secondary minerals indicate that all phases are hydrated (H_2O ranging from ~ 11 to 19 wt.%) (Table 2.1).

Table 2.1. EMP analyses of secondary phases from cemented crusts (wt.% values are reported)

Samples	Locations	K_2O	SO_3	Na_2O	As_2O_5	Fe_2O_3	Cu_2O	CaO	TiO_2	SiO_2	Al_2O_3	H_2O	Total	Molar Fe/As	Molar Fe/S
S2	1	0.01	10.06	1.13	23.05	21.84	0.11	0.04	-	8.74	18.03	18.71	101.72	1.36	1.09
	2	0.02	4.58	0.09	38.97	28.42	0.05	0.01	0.16	2.45	5.93	16.96	97.64	1.05	3.11
	3	0.03	1.48	-	47.62	37.77	0.09	-	0.03	0.68	0.27	15.66	103.64	1.14	12.83
	4	0.04	2.07	0.02	44.44	30.64	-	-	0.05	0.86	0.54	16.25	94.92	0.99	7.42
	5	0.01	2.71	-	44.78	31.16	0.10	0.01	0.04	0.78	0.88	16.25	96.71	1.00	5.76
	*Mean	0.03	2.71	0.03	43.95	32.0	0.06	0.01	0.07	1.19	1.90	16.28			
	*Std.Dev.	0.01	1.35	0.04	3.62	4.03	0.05	0.01	0.06	0.84	2.69	0.53			
S7	1	1.54	32.71	2.09	0.37	44.77	-	0.07	-	0.05	0.74	11.46	93.80	173.59	0.69
	2	1.14	31.61	2.30	0.33	46.11	-	0.04	-	0.00	0.22	11.38	93.14	201.16	0.73
	3	2.22	31.97	2.23	0.59	47.94	-	0.03	-	0.01	0.19	11.21	96.39	116.52	0.75
	4	1.50	30.99	2.35	0.48	45.86	-	0.08	-	0.01	0.50	11.33	93.11	138.55	0.74
	5	1.78	32.27	2.00	0.72	43.78	-	0.05	-	0.07	0.32	11.47	92.46	87.10	0.68
	*Mean	1.64	31.91	2.19	0.50	45.69	-	0.06	-	0.03	0.39	11.37			
	*Std.Dev.	0.40	0.65	0.15	0.16	1.56	-	0.02	-	0.03	0.23	0.11			
LL03	1	6.30	30.14	0.61	1.45	46.87	0.06	0.05	-	0.01	0.31	10.92	96.71	46.52	0.78
	2	6.20	29.27	0.51	1.64	45.02	0.01	0.05	0.02	0.01	0.16	10.97	93.86	39.54	0.77
	3	6.46	29.31	0.72	1.48	45.77	0.03	0.02	-	0.08	0.30	10.92	95.08	44.41	0.78
	4	6.35	30.31	0.73	1.57	44.73	-	0.04	-	0.02	0.16	11.01	94.91	40.91	0.74
	5	6.22	29.40	0.68	1.72	43.35	0.03	0.03	-	0.02	0.06	11.04	92.54	36.26	0.74
	6	6.01	29.37	0.75	1.60	43.75	0.01	0.03	-	0.03	0.07	11.04	92.65	39.41	0.75
	*Mean	6.26	29.63	0.67	1.58	44.92	0.02	0.04	0.00	0.03	0.18	10.98			
	*Std.Dev.	0.15	0.46	0.09	0.10	1.29	0.02	0.01	0.01	0.02	0.11	0.06			

Note: For S2, Mean and Std. Dev. of oxides are calculated based on the values from locations 2 to 5 that contain the same phase. Std.Dev. = standard deviation.

The XRD results represent crust samples collected from five locations (LL03, LL06, S1, S6 and S7) that are separated on the surface by approximately 50 to 150 m. Despite the effort to concentrate secondary-mineral precipitates, it was not possible to extract sufficient secondary phases to obtain satisfactory XRD data. The XRD results indicate that the crusts are dominated by the primary silicate minerals, mainly quartz (22 – 29%) and albite (67 – 75%), with minor amounts of scorodite (2%) and jarosite (5 – 7%).

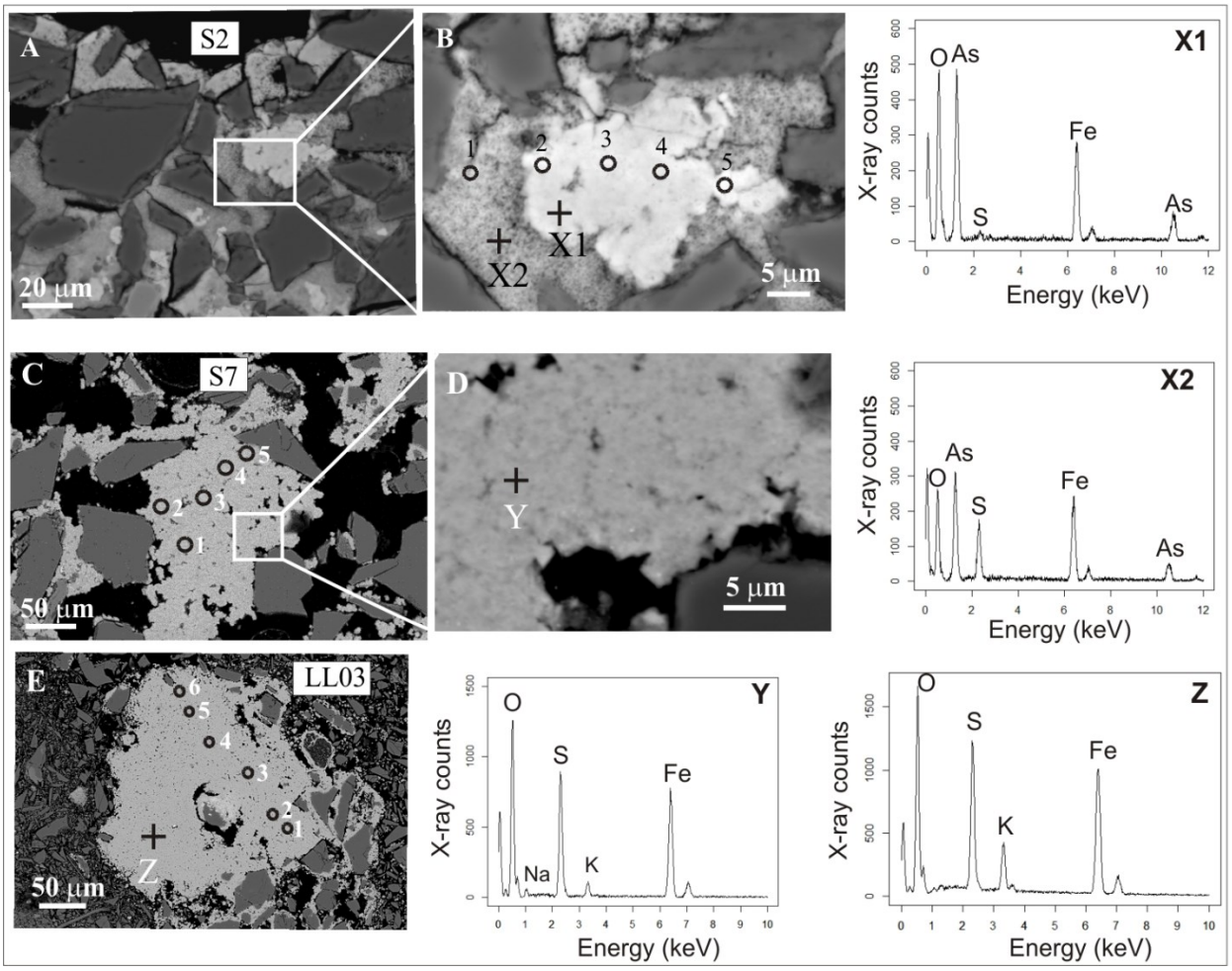

Fig. 2.7. Mineralogy of the cemented crusts in the sand layer at S2, S7, and LL03 (0.08 mbgs). (A, B) Backscattered electron images illustrating localized (μm-scale) morphological variation in secondary-mineral precipitates; X1 and X2 represent locations for EDS analyses on discrete phases, and the EDS spectra indicate that these phases are composed of Fe-As-O and Fe-As-O-S, respectively. Numbers 1 – 5 represent locations for EMP analyses (see Table 2.1). (C, D, E) Backscattered electron images illustrate dense precipitation of secondary minerals. EDS analyses conducted at locations Y and Z indicate Fe, S, O, K, and Na are the principal components. Numbers 1 to 5 in C, and numbers 1 to 6 in E represent locations for EMP analyses (see Table 2.1).

The distribution of secondary-mineral precipitates is variable at the μm scale in the pore space, and at the cm scale in the sand cover, leading to a discontinuous distribution of cemented crusts vertically and horizontally. To understand the development of crusts from the sand-tailings interface toward the surface, detailed SEM imaging and EDS analyses were performed on two samples from LL03 (LL03-T1; depth range 0.065 – 0.15 mbgs, in the sand cover, and LL03-T2; depth range 0.29 – 0.37 mbgs, at the sand-tailings interface region). While more extensive accumulations of secondary precipitates are present in the sand layer at and above the interface (Fig. 2.8A – C, F – G), the distribution of secondary minerals is sparse in the tailings near the sand-tailings interface (Fig. 2.8D – E). The EDS analyses indicate these secondary minerals at the interface region constitute Fe-arsenates whereas jarosite and natrojarosite are present higher in the sand cover.

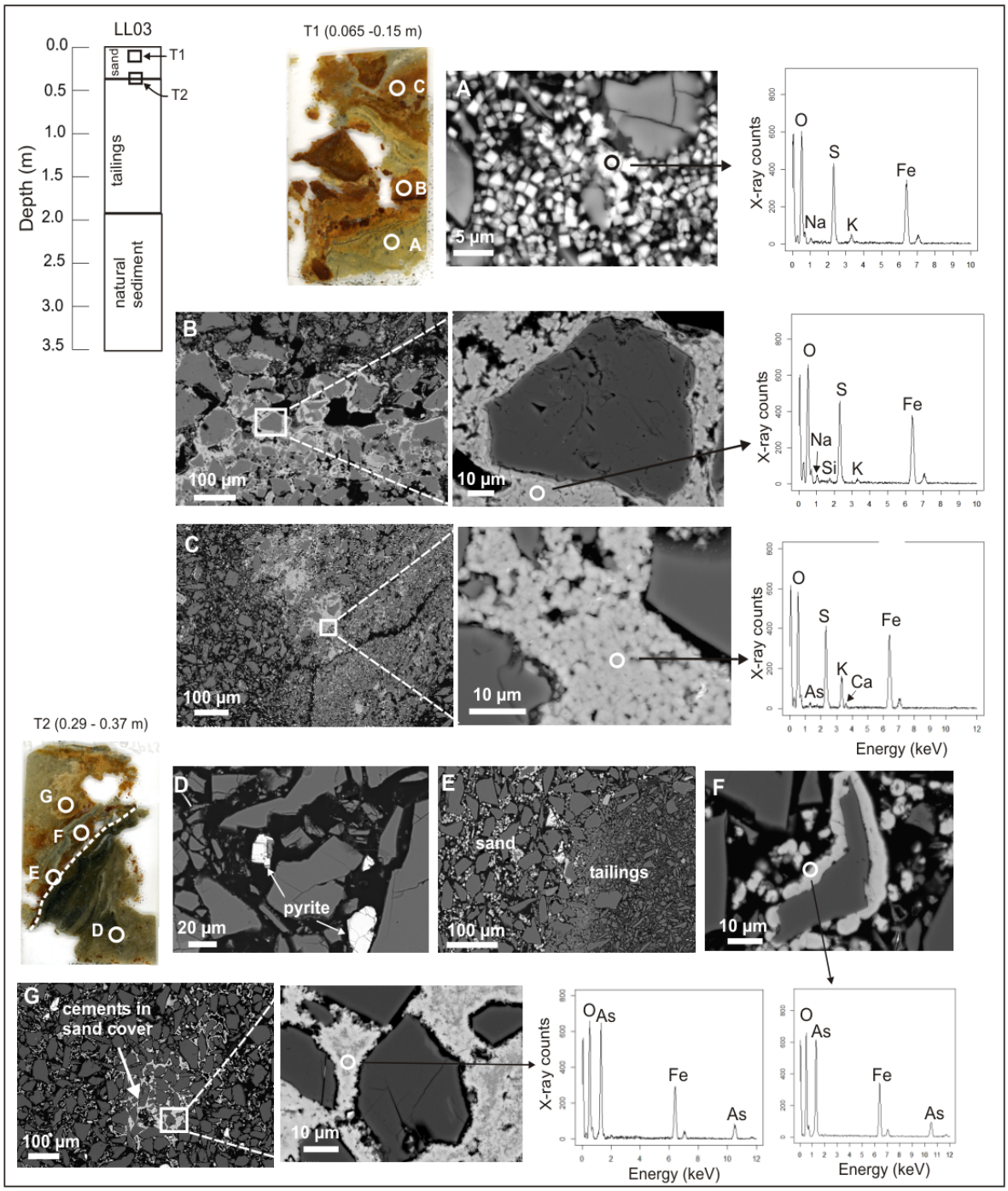

Fig. 2.8. Mineralogy from the sand-tailings interface and sand cover at LL03. Backscattered images illustrate accumulation of secondary-mineral precipitation above the sand-tailings interface (represented by a dashed-line in the thin section) compared to the underlying tailings. EDS analyses indicate the principal secondary-mineral phases consist of Fe-As-O and K/Na-jarosite.

2.4.4.2.3. Natural sediment

Below the tailings-sediment interface, secondary sulfide-bearing minerals are present as disseminated particles (Fig. 2S.2). The samples contain two principal phases composed of Fe-S and As-S, suggesting the presence of secondary ferrous monosulfide or pyrite and orpiment or its amorphous equivalent, respectively. These sulfide minerals occur in association with solid fragments of organic matter, likely indicating that they are products of biogenic sulfate reduction.

2.4.4.2.4. Nanometer-scale characterization

The SEM-EDS imaging and analyses indicate that the secondary-mineral precipitation in the sand cover is commonly observed as cement for the sand particles. In the tailings, precipitation is present as - 1) coatings surrounding the incongruently-dissolved sulfide-mineral grains, and 2) as disseminated particles and clusters in the pore space. Two samples representing sulfide-mineral coatings (LL01) and clusters of secondary mineral precipitation (LL04) in tailings pore space were further characterized at the nanometer scale.

A secondary-mineral coating surrounding an arsenopyrite grain located just below the sand-tailings interface at LL01 (Fig. 2.9A) was sectioned (Fig. 2.9B) to prepare a TEM sample. The layered appearance of the coatings surrounding the grain likely reflects variations in density of the secondary coating. STEM-EDS analyses conducted across the thickness of the secondary coating indicate the composition is dominated by Fe-As-O (Fig. 2.9C, D). SAED patterns (Fig. 2.9E) collected on the coating display broad diffuse rings characteristic of an amorphous or nanocrystalline material. The diffraction lines in the pattern correspond to a mixture of hydrated ferric-arsenates and Fe-oxyhydroxides (Table 2.2).

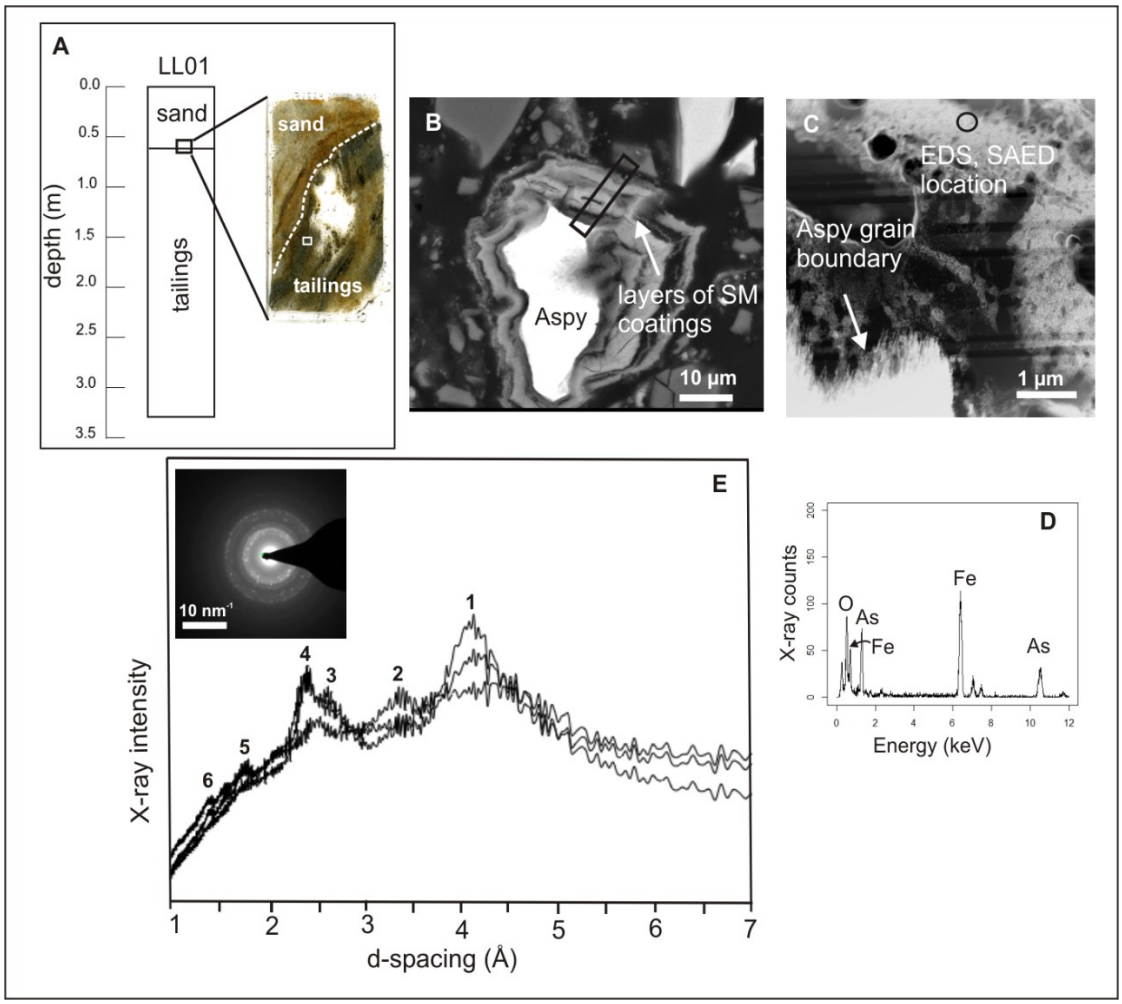

Fig. 2.9. An oxidized arsenopyrite (Aspy) grain located just below the sand-tailings interface at LL01 (A) was selected for nanometer-scale STEM investigation at the location indicated by the rectangle in (B). STEM-EDS analyses on the secondary mineral surrounding the Aspy grain (C) indicate the composition is dominated by Fe-As-O (D). Electron diffraction patterns (E) were derived by radial integration of the image intensity from the SAED patterns collected at location C.

Table 2.2. Identification of electron diffraction lines obtained from the Fe-As-O phase in the secondary mineral coatings surrounding arsenopyrite (Fig. 2.9).

Diffraction line	**Measured d-spacing (Å)**		**Phase**
	d-spacing peak	*d-spacing range*	
1	4.13	4.04 - 4.20	parascorodite?/goethite?
2	3.40	3.37 - 3.43	ferric-arsenate hydrate
3	2.64	2.60 - 2.69	ferric-arsenate hydrate
4	2.41	2.37 - 2.42	ferrihydrite
5	1.80	1.73 - 1.83	? (unidentified)
6	1.43	1.40 - 1.47	ferrihydrite

An aggregation of secondary minerals that infills the pore space of oxidized tailings (0.7 m below the sand-tailings interface at LL03) was sectioned to prepare a TEM sample (Fig. 2S.3). This secondary infill is composed of nanocrystalline minerals with different morphologies (fibrous, elongated) and compositions, mainly Fe-oxyhydroxides and ferric-arsenates.

2.5. DISCUSSION

2.5.1. Sulfide-mineral oxidation and precipitation of secondary minerals

Mineralogical analyses indicate moderate to high degrees of sulfide-mineral oxidation at < 0.7 m depth below the sand-tailings interface (Fig. 2.6). Sulfide oxidation reactions are commonly mediated by micro-organisms (Blowes et al., 1995; Nordstrom and Southam, 1997), as are the Fe and As oxidation reactions that lead to formation of secondary minerals that cement the crusts (Graupner et al., 2007; Liu et al., 2021). Sulfide oxidation has generated low-pH tailings porewater that contains elevated concentrations of dissolved Fe, As, and SO_4 (Fig. 2.3). Oxidation and hydrolysis of aqueous Fe and As species lead to the precipitation of Fe-, As- and SO_4-bearing secondary minerals (see example reactions in Equations 1 to 5).

Fe(II), As(III) oxidation reactions

$$Fe^{2+} + ¼\ O_2 + H^+ = Fe^{3+} + ½\ H_2O \quad (1)$$

$$2H_3AsO_3 + O_2 = 2H_2AsO_4^- + 2H^+ \quad (2)$$

Hydrolysis and precipitation reactions

$$Fe^{3+} + 3H_2O = \underset{\text{Fe-oxyhydroxide}}{Fe(OH)_{3(s)}} + 3H^+ \quad (3)$$

$$Fe^{3+} + H_2AsO_4^- + 2H_2O \rightarrow \underset{\text{scorodite}}{FeAsO_4.\ 2H_2O_{\ (s)}} + 2H^+ \quad (4)$$

$$3Fe^{3+} + K^+ + 2SO_4^{2-} + 6H_2O \rightarrow \underset{\text{K-jarosite}}{KFe_3\ (SO_4)_2(OH)_{6\ (s)}} + 6H^+ \quad (5)$$

Among the secondary minerals, the most commonly observed are ferric-arsenates (principally scorodite) and K/Na jarosite. The concentrations of K and Na in jarosite minerals are less than stoichiometric, suggesting they are solid solutions among the K-Na-H_3O end members, with deficiencies in K and Na offset by the substitution of hydronium ions (H_3O^+) as shown in previous studies (Jamieson et al., 2005; Basciano and Peterson, 2007). Jarosite minerals contain variable amounts of As (0.33 to 1.72 wt.%), which when present as AsO_4^{3-} can substitute for SO_4^{2-}. Fe-oxyhydroxides are the least common secondary minerals and contain a minor amount of As. Although ferric-arsenate and jarosite minerals are commonly observed in the tailings and the sand cover, saturation indices obtained from geochemical modeling of porewater data (Fig. 2.4) do not indicate saturation with respect to scorodite and K-Na jarosite. Such inconsistency between mineralogical data and model predictions might be due to the differences in the scale at which mineralogical and geochemical samples are collected. Secondary Fe- and As-sulfides (Fig. 2S.2)

are observed below the tailings where SO_4^{2-} reduction becomes possible in the organic-carbon-bearing natural sediment (Fortin and Beveridge, 1997). The formation of these secondary sulfides attenuates Fe and As, which were released during the oxidation of the primary sulfide minerals.

At depths above 0.7 m, Fe-, As- and SO_4-bearing secondary minerals predominantly form as coatings surrounding the incongruently-dissolved sulfide minerals (Fig. 2.6) and silicate grains (Figs. 2.7 and 2.8), with lesser occurrences of small accumulations infilling pore spaces of the tailings (Fig. 2.8). At and above the sand-tailings interface, secondary minerals cement the particles (Figs. 2.7 and 2.8), and when the precipitation is sufficiently extensive, cemented crusts form. The crusts on the tailings surface along the slope of the stream bank are relatively thin (mm-scale) but those in the sand cover are relatively thick (cm-scale) and discontinuous (Fig. 2.5). The differences in the crust morphologies can be attributed to differences in the hydrology and solute transport mechanisms. Along the slope of the stream bank, secondary mineral precipitation occurs where laterally-directed hydraulic gradients cause groundwater to discharge where the slope intersects the saturated tailings. Precipitates form when solutes in the groundwater are concentrated by evaporation, and oxidation of Fe(II) to Fe(III) and As(III) to As(V) occurs. The elevated concentrations of Fe(III) and As(V) contribute to the porewater becoming supersaturated with respect to Fe(III)-and As(V)-bearing secondary minerals.

The solutes can be transported upward to the sand layer with groundwater during periods when the water table is near the surface or due to capillary-pressure gradients in the vadose zone (discussed in Section 2.5.2). The water table position is variable; for example, water level measurements taken in October 2018 and July 2019 range from 0.02 to 1.07 mbgs at P1 and 0.29 to 1.17 mbgs at P5, respectively. The seasonal fluctuations can impact the rate of sulfide oxidation in shallow tailings and the mechanism of solute transport. For example, when the water table is

high and the tailings are saturated, the rate of sulfide oxidation is low, and solutes are transported by upward hydraulic gradients. In contrast, when the water table is low, the influx of oxygen to shallow tailings enhances the rate of sulfide oxidation, and evaporative conditions drive upward-transport of solutes by capillarity. Both transport mechanisms facilitate upward flow of solutes to the sand cover, and the subsequent precipitation of secondary minerals form the relatively thick cemented crusts in the sand cover.

2.5.2. Evolution of cemented crusts in sand layer

The roles of capillarity and precipitation-induced pore-size evolution in facilitating the development of cemented crusts in the sand cover are represented schematically in Figure 2.10. During dry seasons, when the water table is below the sand-tailings interface, an influx of oxygen occurs above the air-entry point (Fig. 2.10A) and promotes oxidation of aqueous Fe(II) and As(III) species (Equations 1 – 2) in the unsaturated pores at the interface of air and porewater. Hydrolysis of the oxidized Fe and As species (Equations 3 – 5) leads to the precipitation of secondary minerals (e.g., scorodite, k-jarosite). Precipitation of secondary minerals reduces effective porosity as it infills pore spaces (Fig. 2.10B). Given that capillary pressure is inversely related to pore size, a reduction in pore size contributes to an increase in capillary pressure and a higher capillary rise. This causes an upward migration in the air-entry point (Fig. 2.10C). The migration of the air-entry point at the sand-tailings interface, which is closer to the water table, is expected to be relatively fast due to higher pressure head compared to the region above the interface. In the absence of a capillary break (i.e., a coarse-grained layer that prevents water rise) in the cover material, the reaction zone for oxidation, hydrolysis, and precipitation at the air-entry point would ascend faster near the sand-tailings interface, slowing towards the sand surface (Fig. 2.10C). However, as the upward solute transport is dependent on hydrological conditions that vary seasonally, there is

spatial and temporal variability in the solute transport. Moreover, the sand layer consists of a range of particle sizes (sand-to-silt) and the pore-radii are not uniform. Such heterogeneity in particle-size results in spatial variability of capillary pressure which causes spatial variations in capillarity-driven transport and precipitation of secondary minerals. Consequently, seasonal variations in hydrologic conditions and heterogeneity in particle sizes cause the cemented crusts to form discontinuous layers within the sand layer.

Regions with a continental climate, such as Sudbury, favour for the formation of cemented crusts or hardpans because intermittent wet and dry cycles promote sulfide oxidation, evaporative porewater losses and upward mobilization of solutes by capillary forces. In absence of a capillary break, cemented crusts will form in shallow tailings, or in cover materials. As the crusts continually develop, they transfer the contaminants to shallow depths in the waste impoundment where they are susceptible to erosion by surface water.

Natural freeze-thaw cycles, common in continental climates (McGregor and Blowes, 2002), could also contribute to the physical weathering of crusts, increasing their susceptibility to erosion. Recent studies (Ding et al., 2022; Li et al., 2022) have demonstrated that the shear strength of tailings decreases as a function of the number of freeze-thaw cycles. In Sudbury, where the average winter temperature (November to March, inclusive) is -5.6 °C, typically there are 10 to 15 freeze-thaw cycles per year (http://climate.weather.gc.ca). A maximum number of freeze-thaw cycles, and therefore the greatest susceptibility to erosion would occur in regions where the average winter temperature is near 0 °C. Combined with the physical weakening of the surface material by freeze-thaw action, surface runoff and stream flow due to precipitation, particularly during storm events, has contributed to erosion and transport of the crusts and the tailings. Wind erosion, a common dispersal mechanism in arid and semi-arid regions (Blight, 2007), is not apparent at Long Lake.

Although the likelihood of weathering, crust formation, and erosion are climate specific, these processes must be taken into account during tailings management to minimize environmental risk.

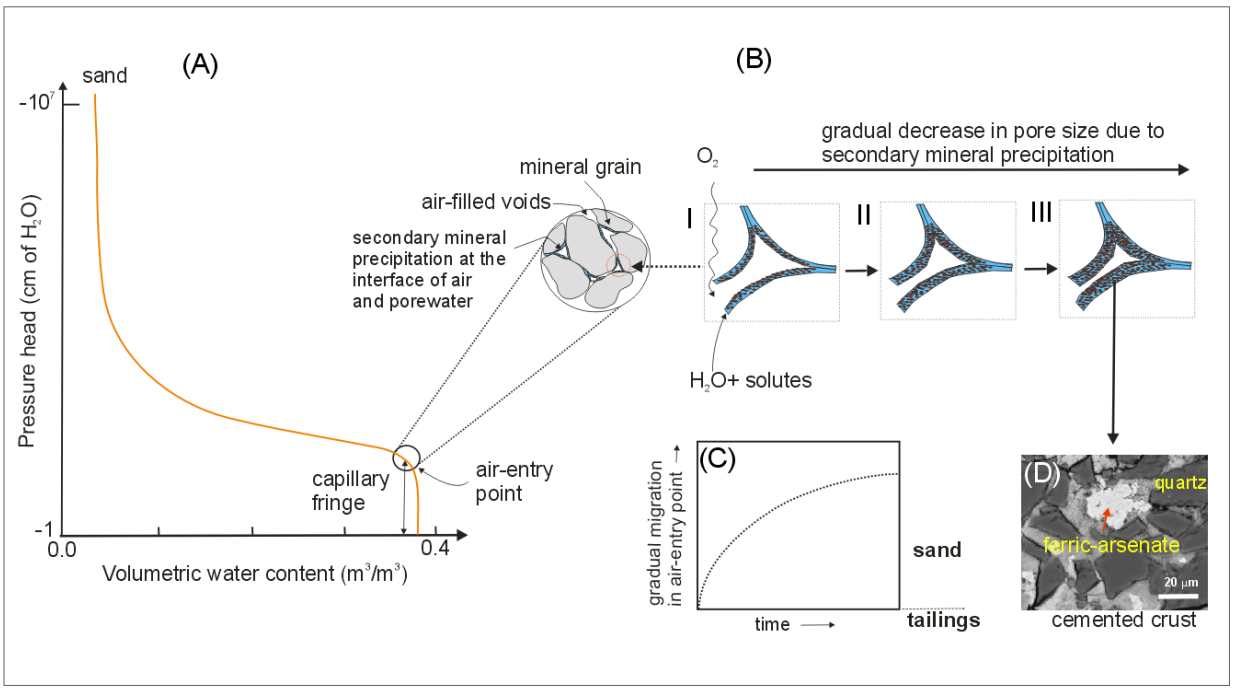

Fig. 2.10. Conceptual diagram showing how a gradual decrease in pore size due to mineral precipitation influences the capillary rise of porewater and development of cemented crusts in the sand. During dry seasons, when the water table is below the sand-tailings interface and the air-entry point (A) is near the interface, secondary mineral precipitation occurs in the partially saturated pores. The mineral precipitation leads to a reduction in pore size (I to III; B) that enhances the capillary rise of pore water. This causes a gradual upward migration in the air-entry point (C) and the associated locus of precipitation reactions. Long-term sulfide-mineral oxidation and capillarity contribute to the development of cemented crusts in the sand as shown in the backscattered electron micrograph (D)

2.6. CONCLUSIONS

The geochemical and mineralogical study of the Long Lake tailings demonstrates that long-term sulfide-mineral oxidation has generated acidic porewater that contains elevated concentrations of As, Fe, and SO_4. The precipitation of Fe-and As-bearing secondary minerals (ferric-arsenates/sulfates, K-Na-H_3O jarosite, and Fe-oxyhydroxides) in the sand cover results from upward transport of solutes from the oxidized tailings. The upward transport of solutes is facilitated by hydraulic gradients that are dependent on seasonally-variable hydrologic conditions, thereby contributing to the formation of discontinuous cemented crusts in the sand. As a consequence, the sand cover that was placed as a preliminary remediation step to prevent erosion and transport of tailings, now contains As-bearing secondary minerals. Its erosion at several locations has become a secondary source of As contamination, negating the intended benefits of the cover.

Acknowledgements

Funding for this study was provided by the Natural Sciences and Engineering Research Council of Canada Strategic Partnership Grants for Networks Program, 'Toward Environmentally Responsible Resource Extraction Network' (NSERC-TERRE-NET, NETGP 479708-15; D. Blowes, Principal Investigator). We thank S. Holland (University of Waterloo) for help with sampling tailings cores. We gratefully acknowledge the assistance provided by Martin Couillard (National Research Council of Canada) in collecting SAED patterns. This manuscript benefitted from critical reviews by Lianna Smith (University of Ottawa) and three anonymous reviewers.

Supporting Information

Fig. 2S.1. Tailings area TA-01(view looking north). The tailings and the cemented crusts have been eroded by the creek that flows through the tailings impoundment toward the lake.

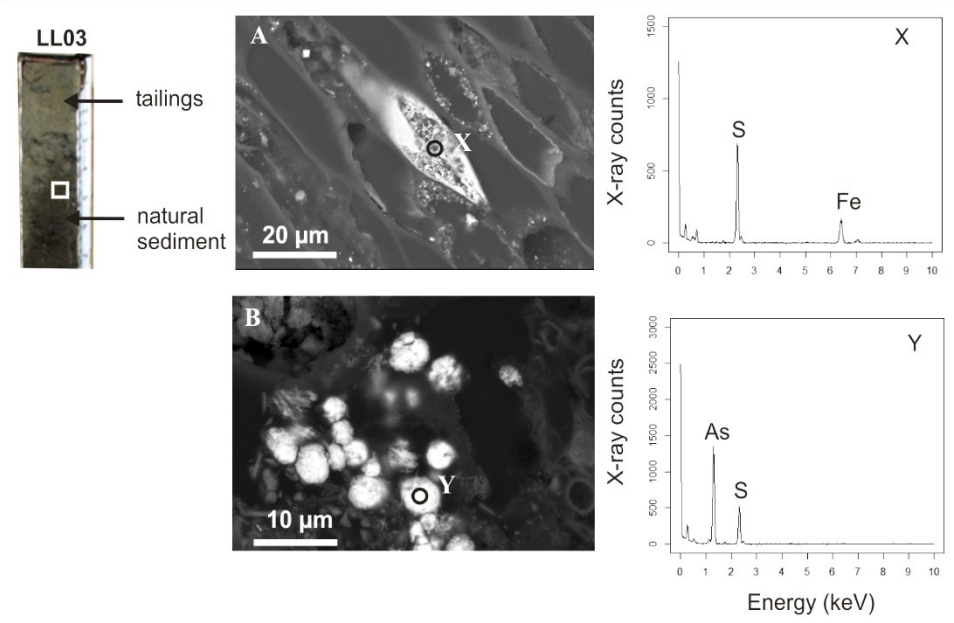

Fig. 2S.2. Backscattered images (A, B) of secondary sulfide minerals in the natural sediment just below the tailings-sediment interface at LL03. The EDS spectra indicate that they are Fe-sulfide (X) and As-sulfide (Y). The material surrounding the secondary minerals is dominantly fragments of vegetation.

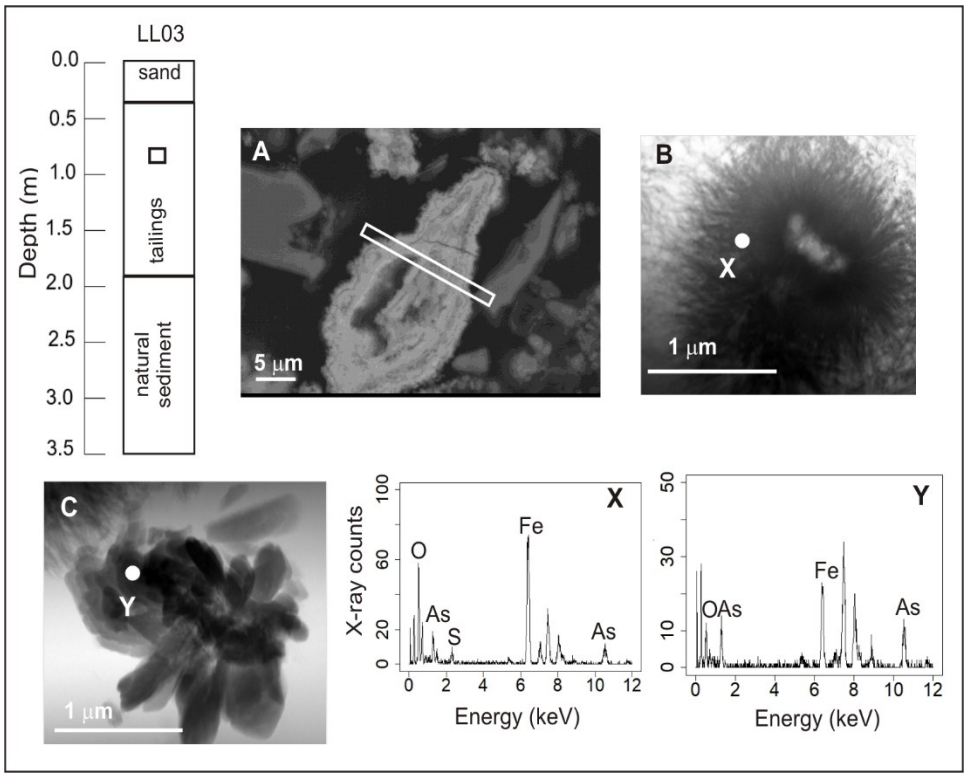

Fig. 2S.3. Secondary-mineral precipitate in the pore space of oxidized tailings at LL03 was selected for nanometer-scale STEM investigation at the location indicated by a rectangle in (A). STEM images illustrate secondary minerals with fibrous (B) and prismatic (C) habit. The EDS spectra indicate that the fibrous particles (X in panel B) are dominantly composed of Fe-O with minor As, and that of the prismatic grains (Y in panel C) are Fe-As-O.

References

Acero, P., Ayora, C., Carrera, J., 2007. Coupled thermal, hydraulic and geochemical evolution of pyritic tailings in unsaturated column experiments. Geochimica et Cosmochimica Acta, 71, 5325–5338.

Ahn, J. S., Song, H., Yim, G. J., Ji, S. W., Kim, J. G., 2011. An engineered cover system for mine tailings using a hardpan layer: a solidification/stabilization method for layer and field performance evaluation. Journal of Hazardous Materials, 197, 153–160.

Al, T. A. and Blowes, D. W., 1999. The hydrogeology of a tailings impoundment formed by central discharge of thickened tailings: implications for tailings management. Journal of Contaminant Hydrology, 38, 489–505.

Alakangas, L. and Öhlander, B., 2006. Formation and composition of cemented layers in low-sulphide mine tailings, Laver, northern Sweden. Environmental Geology, 50, 809–819.

Armstrong, J. T., 1988. Quantitative analysis of silicate and oxide materials: comparison of Monte Carlo, ZAF, and ψ (ρz) procedures. Microbeam Analysis, 239–246.

Bain, J. G., Blowes, D. W., Robertson, W. D., Frind, E. O., 2000. Modeling of sulfide oxidation with reactive transport at a mine drainage site. Journal of Contaminant Hydrology, 41, 23–47.

Ball J. W. and Nordstrom D. K., 1991. User's manual for WATEQ4F with revised thermodynamic data base and test cases for calculating speciation of major, trace and redox elements in natural waters. U.S. Geological Survey, Open File Report 91–183.

Basciano, L. C. and Peterson, R. C., 2007. Jarosite-hydronium jarosite solid-solution series with full iron site occupancy: mineralogy and crystal chemistry. American Mineralogist, 92, 1464–1473.

Benzaazoua, M., Bussière, B., Dagenais, A.M., Archambault, M., 2004. Kinetic tests comparison and interpretation for prediction of the Joutel tailings acid generation potential. Environmental Geology, 46, 1086-1101.

Blight, G. E., 2007. Wind erosion of tailings dams and mitigation of the dust nuisance. Journal of the Southern African Institute of Mining and Metallurgy, 107(2), 99–107.

Blowes, D. W., Reardon, E. J., Jambor, J. L., Cherry, J. A., 1991. The formation and potential importance of cemented layers in inactive sulfide mine tailings. Geochimica et Cosmochimica Acta, 55, 965–978.

Blowes, D. W., Al, T., Lortie, L., Gould, W. D., Jambor, J. L., 1995. Microbiological, chemical, and mineralogical characterization of the Kidd creek mine tailings impoundment, Timmins area, Ontario. Geomicrobiology Journal, 13, 13–31.

Blowes, D. W., Jambor, J. L., Hanton-Fong, C. J., Lortie, L., Gould, W. D., 1998. Geochemical, mineralogical and microbiological characterization of a sulphide-bearing carbonate-rich gold-mine tailings impoundment, Joutel, Québec. Applied Geochemistry, 13, 687–705.

Bussière, B., Benzaazoua, M., Aubertin, M., Mbonimpa, M., 2004. A laboratory study of covers made of low-sulphide tailings to prevent acid mine drainage. Environmental Geology, 45, 609–622.

Bussière, B., Maqsoud, A., Aubertin, M., Martschuk, J., McMullen, J., Julien, M.R., 2006. Performance of the oxygen limiting cover at the LTA site, Malartic, Quebéc. CIM Bulletin, 1(6), 1–11.

CCME (Canadian Council of Ministers of the Environment), 1997. Canadian Water Quality Guidelines for the Protection of Aquatic Life.

CH2M HILL, 2014. Site Characterization report and data analysis – Long Lake Gold Mine tailings areas, Eden Township, Ontario. Final technical report prepared for Ontario Ministry of Northern Development and Mines.

Dagenais, A.M., Aubertin, M., Bussière, B., Martin, V., 2005. Large scale applications of covers with capillary barrier effects to control the production of acid mine drainage. Proceedings of Post Mining 2005, 1–12.

DeSisto, S. L., Jamieson, H. E., Parsons, M. B., 2011. Influence of hardpan layers on arsenic mobility in historical gold mine tailings. Applied Geochemistry, 26, 2004–2018.

Ding, P., Hou, Y., Han, D., Zhang, X., Cao, S., Li, C., 2022. Effect of freeze–thaw cycles on mechanical and microstructural properties of tailings reinforced with cement-based material. Minerals, 12(4), 413.

Dold, B. and Fontbote, L., 2001. Element cycling and secondary mineralogy in porphyry copper tailings as a function of climate, primary mineralogy, and mineral processing. Journal of Geochemical Exploration, 74, 3–55.

Elghali, A., Benzaazoua, M., Bussière, B., Kennedy, C., Parwani, R., Graham, S., 2019. The role of hardpan formation on the reactivity of sulfidic mine tailings: A case study at Joutel mine (Quebéc). Science of the Total Environment, 654, 118–128.

Fortin, D. and Beveridge, T. J., 1997. Microbial sulfate reduction within sulfidic mine tailings: formation of diagenetic Fe sulfides. Geomicrobiology Journal, 14, 1–21.

Gilbert, S. E., Cooke, D. R., Hollings, P., 2003. The effects of hardpan layers on the water chemistry from the leaching of pyrrhotite-rich tailings material. Environmental Geology, 44, 687–697.

Gordon, J.B., Lovell, H.L., Grijs, Jan de, Davie R.F., 1979. Gold deposits of Ontario, Part 2. Part of District of Cochrane, Districts of Muskoka, Nipissing, Parry Sound, Sudbury, Timiskaming and Counties of southern Ontario; Ontario Geological Survey, Mineral Deposits Circular 18, 253p.

Graupner, T., Kassahun, A., Rammlmair, D., Meima, J. A., Kock, D., Furche, M., Fiege, A., Schippers, A., Melcher, F., 2007. Formation of sequences of cemented layers and hardpans within sulfide-bearing mine tailings (mine district Freiberg, Germany). Applied Geochemistry, 22, 2486–2508.

Heikkinen, P. M., Räisänen, M. L., Johnson, R. H., 2009. Geochemical characterisation of seepage and drainage water quality from two sulphide mine tailings impoundments: acid mine drainage versus neutral mine drainage. Mine Water and the Environment, 28, 30–49.

Jambor, J. L., Ptacek, C. J., Blowes, D. W., Moncur, M. C., 2005. Acid drainage from the oxidation of iron sulfides and sphalerite in mine wastes. In: Fujisawa, T. (Ed.), Lead & Zinc 2005, vol. 1, The Mining and Materials Processing Institute of Japan, 715–737.

Jamieson, H. E., Robinson, C., Alpers, C. N., Nordstrom, D. K., Poustovetov, A., Lowers, H. A., 2005. The composition of coexisting jarosite-group minerals and water from the Richmond mine, Iron Mountain, California. The Canadian Mineralogist, 43, 1225–1242.

Larochelle, C. G., Bussière, B., Pabst, T., 2019. Acid-generating waste rocks as capillary break layers in covers with capillary barrier effects for mine site reclamation. Water, Air, and Soil Pollution, 230, 1–16.

Li, C., Jin, J., Wu, P., Xu, B., 2022. Effect of freeze–thaw cycles on shear strength of tailings and prediction by grey model. Minerals, 12(9), 1125.

Liu, Y., Wu, S., Nguyen, T. A. H., Southam, G., Chan, T. S., Lu, Y. R., Huang, L., 2018. Microstructural characteristics of naturally formed hardpan capping sulfidic copper-lead-zinc tailings. Environmental Pollution, 242, 1500–1509.

Liu, Y., Wu, S., Southam, G., Nguyen, T. A. H., Kopittke, P. M., Paterson, D. J., Huang, L., 2019. Zinc and lead encapsulated in amorphous ferric cements within hardpans in situ formed from sulfidic Cu-Pb-Zn tailings. Environmental Pollution, 252, 1106–1116.

Liu, Y., Wu, S., Southam, G., Chan, T. S., Lu, Y. R., Paterson, D. J., Huang, L., 2021. Bioaugmentation with Acidithiobacillus species accelerates mineral weathering and formation of secondary mineral cements for hardpan development in sulfidic Pb-Zn tailings. Journal of Hazardous Materials, 411, 124988.

Lottermoser, B.G., 2010. Introduction to mine waste. In: Mine wastes, Springer, Berlin, Heidelberg, 1–41.

McGregor, R. G. and Blowes, D. W., 2002. The physical, chemical and mineralogical properties of three cemented layers within sulfide-bearing mine tailings. Journal of Geochemical Exploration, 76, 195–207.

Molson, J. W., Fala, O., Aubertin, M., Bussière, B., 2005. Numerical simulations of pyrite oxidation and acid mine drainage in unsaturated waste rock piles. Journal of Contaminant Hydrology, 78, 343–371.

Moncur, M. C., Ptacek, C. J., Blowes, D. W., Jambor, J. L., 2005. Release, transport and attenuation of metals from an old tailings impoundment. Applied Geochemistry, 20, 639–659.

Moncur, M. C., Blowes, D. W., Ptacek, C. J., 2013. Pore-water extraction from the unsaturated and saturated zones. Canadian Journal of Earth Sciences, 50, 1051–1058.

Murciego, A., Alvarez-Ayuso, E., Aldana-Martinez, S. C., Sanz-Arranz, A., Medina-Garcia, J., Rull-Perez, F., Villar-Alonso, P., 2019. Characterization of secondary products in arsenopyrite-bearing mine wastes: influence of cementation on arsenic attenuation. Journal of Hazardous Materials, 373, 425–436.

Nesbitt, H.W., Muir, I.J., Pratt, A.R., 1995. Oxidation of arsenopyrite by air and air-saturated, distilled water, and implications for mechanism of oxidation. Geochimica et Cosmochimica Acta, 59, 1773–1786.

Nordstrom, D.K., 1977. Thermochemical redox equilibria of ZoBell's solution. Geochimica et Cosmochimica Acta, 41, 1835-1841.

Nordstrom, D. K. and Southam, G., 1997. Geomicrobiology of sulfide mineral oxidation. In: Banfield, J.F. and Nealson, K.H., eds, Geomicrobiology: Interactions Between Microbes and Minerals, 35. Reviews in Mineralogy, Mineralogical Society of America, Washington, DC, 361–390.

Pabst, T., Bussière, B., Aubertin M., Molson, J., 2018. Comparative performance of cover systems to prevent acid mine drainage from pre-oxidized tailings: a numerical hydro-geochemical assessment. Journal of Contaminant Hydrology, 214, 39–53.

Parkhurst, D. L. and Appelo, C. A. J., 1999. User's Guide to PHREEQC (Version 2) – A Computer program for speciation, batch reaction, one-dimensional transport, and inverse geochemical calculations. Water-Resources Investigation Report 99–4259, U.S. Geological Survey.

Pedersen, T.F., Losher, A.J., 1988. Diagenetic processes in aquatic mine tailings deposits in British Columbia. W. Salomons et al. (eds.), Chemistry and Biology of Solid Waste. Springer, Berlin, Heidelberg, 238–258.

Pedretti, D., Lassin, A., Beckie, R. D., 2015. Analysis of the potential impact of capillarity on long-term geochemical processes in sulphidic waste-rock dumps. Applied Geochemistry, 62, 75–83.

Petrunic, B. M., Al, T. A., Weaver, L., Hall, D., 2009. Identification and characterization of secondary minerals formed in tungsten mine tailings using transmission electron microscopy. Applied Geochemistry, 24, 2222–2233.

Rimstidt, J.D. and Vaughan, D.J., 2003. Pyrite oxidation: a state-of-the-art assessment of the reaction mechanism. Geochimica et Cosmochimica Acta, 67, 873–880.

SNC-Lavalin, 2016. Long-term monitoring well installation and groundwater assessment report, 624398-0000-4GCC-0008-PB. Prepared for Ministry of the Northern Development Mines, Ontario.

Starr, R.C. and Ingleton, R.A., 1992. A new method for collecting core samples without a drill rig. Groundwater Monitoring and Remediation, 12, 91-95.

Walker, S. R., Parsons, M. B., Jamieson, H. E., Lanzirotti, A., 2009. Arsenic mineralogy of near-surface tailings and soils: influences on arsenic mobility and bioaccessibility in the Nova Scotia gold mining districts. The Canadian Mineralogist, 47, 533–556.

Winter, L.D.S., 1986. Geological report on the Eden Township Property, District of Sudbury, Ontario. Prepared for Loki Resources Inc.

Wunderly, M.D., Blowes, D.W., Frind, E.O., Ptacek, C.J., 1996. Sulfide-mineral oxidation and subsequent reactive transport of oxidation products in mine tailings impoundments: a numerical model. Water Resources Research, 32, 3173–3187.

CHAPTER THREE

DIAGENETIC IRON-OXYHYDROXIDES FORMED IN SUBOXIC TO ANOXIC MINE-IMPACTED LAKE SEDIMENTS NEAR SUDBURY, ONTARIO[1]

[1]Reprinted with permission from Chemical Geology:
Sapkota, B. and Al, T. , 2024. Diagenetic iron-oxyhydroxides formed in suboxic to anoxic mine-impacted lake sediments near Sudbury, Ontario. Chemical Geology, 658, 122131.

Abstract

Iron-oxyhydroxides are common in lake sediments, typically forming in oxidizing conditions near the sediment-water interface. However, in the mine-tailings-impacted sediment delta at Long Lake near Sudbury, Ontario, diagenetic Fe-oxyhydroxides are formed in suboxic-anoxic conditions. Geochemical and mineralogical techniques were applied to investigate the diagenetic transformations of tailings-derived oxidation products following burial in the sediment delta. Two sets of vertical cores were collected, one from a shallow-water location in the sediment delta near the lake shore and the other from a deeper-water location, approximately 90 m north from the mouth of the active channel. One core from each location was sectioned in the field into 0.1 m intervals using an anaerobic globe bag and porewater was extracted for aqueous geochemical analysis. The second core from each location was dried anaerobically and sub-sampled for solid-phase geochemical and mineralogical analyses. The aqueous concentrations of As, Fe, and SO_4 are elevated near the sediment-water interface at both locations but at the shallow location they decline to the lowest observed concentrations at depth in the natural sediment. The decline in their concentrations may be enhanced by bacterial SO_4 reduction and precipitation of Fe- and As-sulfides which were observed in mineralogical analysis. The mine-impacted sediment consists of numerous fragments of tailings-derived ferric-arsenate-cemented crusts. Compared to the

cemented crusts that occur in the tailings, these fragments exhibit partial-dissolution features and SEM-EDS analyses demonstrate that they have relatively low As/Fe ratios suggesting the occurrence of selective As(V) dissolution during diagenesis. Diagenetic Fe-oxyhydroxides occur throughout the mine-impacted sediment, including zones that contain diagenetic Fe- and As-sulfides, suggesting they may have formed in suboxic-anoxic conditions. They occur proximal to, but separate from, the fragments of tailings-derived crust and display diverse morphologies, including what may be a previously unreported spherulitic form. Individual Fe-oxyhydroxides range in size from nm to μm but they mostly occur in delicate clusters suggesting they are autochthonous. Compared to the cemented crusts from the tailings, they contain very small amounts of As. Analysis of one spherule indicates it contains lepidocrocite microcrystals with amorphous $SiO_2.nH_2O$ in the interstitial spaces. The microcrystals contain a mixture of Fe(III) and Fe(II), with Fe(III)/ΣFe = approximately 0.8. We interpret them to have formed by burst nucleation from Fe(III)-supersaturated solution, with subsequent aggregation of crystallites to form spherules.

Keywords: Mine tailings; Ferric-arsenate; Diagenesis; Spherulitic Fe-oxyhydroxides; STEM-EELS; Lepidocrocite

3.1. INTRODUCTION

Iron-oxides, hydroxides, and oxyhydroxides, collectively referred to as Fe-oxyhydroxides, are common in lake sediments, typically forming in oxidizing conditions (Ferris et al., 1989; Fortin et al., 1993; Fortin and Langley, 2005; Couture et al., 2010). Those most commonly encountered include ferric-oxyhydroxides (e.g., ferrihydrite [$Fe_{10}O_{14}(OH)_2$], goethite [α-FeOOH], lepidocrocite [γ-FeOOH]) and mixed-valence Fe-oxyhydroxides (Coey et al., 1974; Davison, 1993; Fortin et al., 1993; van der Zee et al., 2003). They are formed mainly by i) direct precipitation from Fe(II) and/or Fe(III)-containing solutions, and ii) transformation of Fe-oxyhydroxide

precursors, which involves the dissolution of a precursor and subsequent reprecipitation of new phases (e.g., ferrihydrite to goethite) (Cornell and Schwertmann, 2003). The dissolution of a precursor can be facilitated by multiple processes, including protonation, complexation, and reduction. In lake sediments, where anoxic conditions typically prevail below the first few centimeters at the sediment-water interface (Davison, 1993), microbially-mediated reduction has been shown to be a common mechanism for the dissolution of Fe(III)-minerals (Lovley, 1997; Cornell and Schwertmann, 2003; Bonneville et al., 2004; Cutting et al., 2009).

Under anoxic conditions, microorganisms fulfill their respiration requirements by reduction of electron acceptors such as As(V) and Fe(III) (Cummings et al., 1999). For instance, dissimilatory As-reducing bacteria related to *Geospirillum* and *Bacillus* spp. (Macy et al., 2000; Oremland and Stolz, 2003) and dissimilatory Fe(III)-reducing bacteria related to *Shewanella* and *Geobacter* spp. (Cummings et al., 1999; Esther et al., 2015) obtain electrons when metabolizing organic matter and transfer them to the surfaces of As(V) and Fe(III)-minerals via electron-shuttling compounds such as humic substances (Lovley et al., 1996; Nevin and Lovley, 2002), leading to the reduction of structurally-bound As(V) and Fe(III) (Equation 1).

$$4Fe(OH)_{3(s)} + CH_2O + 7H^+ \rightarrow 4Fe^{2+} + HCO_3^- + 10H_2O \quad (1)$$

The reductive dissolution of Fe(III)-minerals releases Fe(II) which is relatively mobile in anoxic conditions. It can be transported upward towards the sediment-water interface where O_2 may be supplied from the overlying water causing subsequent Fe(II) oxidation and leading to the formation of Fe(III)-oxyhydroxides. The newly formed Fe(III)-oxyhydroxides may be buried by subsequent sedimentation and undergo reduction, thus completing the Fe redox cycle in the vicinity of an oxic-anoxic interface. When both As- and Fe-reducing bacteria coexist in As-Fe-rich sediment, some studies (Nicholas et al., 2003; Campbell et al., 2006) reported that dissimilatory As(V)-reduction

preceded Fe(III)-reduction. Moreover, As-reduction by As(V)-respiring bacteria can occur independent of Fe-reduction (Das et al., 2016). In each case, the reduction of As(V) will release As(III) which is relatively mobile in anoxic conditions, leaving Fe(III) which may then reprecipitate as one or more Fe-oxyhydroxides.

Previous studies (Robins, 1987; Zhu and Merkel, 2001; Bluteau and Demopoulos, 2007; Paktunc and Bruggeman, 2010) have also reported abiogenic incongruent dissolution of some Fe(III)-minerals in circumneutral freshwater conditions. Laboratory studies conducted by Zhu and Merkel (2001) and Bluteau and Demopoulos (2007) demonstrated that incongruent dissolution of scorodite [$FeAsO_4 \cdot 2H_2O$], a common As-Fe-bearing secondary mineral in sulfide mine wastes, results in the release of various Fe(III) (e.g., Fe^{3+}, $Fe(OH)_2^+$, $FeOH^{2+}$) and As(V) species (e.g., $H_2AsO_4^-$, $HAsO_4^{2-}$), as exemplified in Equations 2 and 3 (modified after Zhu and Merkel, 2001). The aqueous Fe(III) can form one or more Fe-oxyhydroxides as represented by $Fe(OH)_3$ in Equations 2 and 3. However, abiogenic incongruent dissolution of scorodite in circumneutral pH conditons is slow and may not always reach equilibrium (Demopoulos, 2005). Bluteau and Demopoulos (2007) reported that at near-neutral pH, incongruent dissolution of scorodite led to stable aqueous As concentrations of 5.9 mg/L after 24 weeks.

$$FeAsO_4 \cdot 2H_2O + H_2O = Fe(OH)_{3\,(s)} + H_2AsO_4^- + H^+ \qquad \text{(pH: } \sim 5 - 6.5\text{)} \qquad (2)$$

$$FeAsO_4 \cdot 2H_2O + H_2O = Fe(OH)_{3\,(s)} + HAsO_4^{2-} + 2H^+ \qquad \text{(pH: } \sim 6.5 - 10.5\text{)} \qquad (3)$$

Many studies have documented the presence of Fe-oxyhydroxides near the sediment surface. For example, Ferris et al. (1989) reported fibrous, poorly-ordered, nano-sized ferrihydrite with lesser amounts of goethite and hematite in surficial lake sediments and sediment samples collected from seepage areas at inactive mine tailings ponds. Fortin et al. (1993) identified lath-like lepidocrocite particles, and spherical and ellipsoidal ferrihydrite particles (50 – 500 nm) in the

upper 10 cm of lake sediments. Similarly, Crowe et al. (2007) identified acicular fibers of goethite dominating the surface sediments (<10 cm) of Lake Matano, Indonesia, and van der Zee et al. (2003) reported nanogoethite (< 12 nm) in surficial (0 – 2 cm) lake sediments near Rouyn-Noranda, Quebec. While Fe-oxyhydroxides in surficial sediments near oxic-anoxic boundaries in freshwater lakes are well documented, to our knowledge, their formation in suboxic-anoxic conditions has not been reported.

The objective of this study was to understand the diagenetic transformations that affect tailings-derived oxidation products following burial in a lacustrine sedimentary delta, and we report on the occurrence and properties of Fe-oxyhydroxides that form under suboxic-anoxic conditions, including a unique spherulitic form. To the best of our knowledge, such diagenetic spherules have not been previously reported.

3.2. SITE DESCRIPTION

The former Long Lake Gold Mine (46º 18’ 19.1’’ N and 81º, 8’ 59.5’’ W) (Fig. 3.1), which operated from 1908 to 1939, is located in Eden Township, approximately 17 km southwest of the city of Sudbury. Long Lake has received tailings-derived solids in stream runoff since the gold mine began in 1908. Sapkota et al. (2023) provide an overview of the mining history and the current mine site conditions. During the mining operation, the tailings were discharged directly onto the ground surface without any additional containment. Over time, the erosion and transport of tailings-derived solids resulted in the formation of a sediment delta at the mouth of Luke Creek (Fig. 3.1). In an effort to limit the erosion and transport of tailings-derived solids into the lake, the Ontario government constructed a sand cover in the early 1970s (CH2M HILL, 2014). However, oxidation of arsenopyrite and pyrite in the tailings caused the formation of Fe-As-bearing

cemented crusts in the tailings and sand cover, and those crusts are being eroded and transported to the lake (Sapkota et al., 2023).

The Ontario government has been monitoring the water quality in Luke Creek and in the lake near the mouth of Luke Creek. The water quality measurements from 2012 to 2018 by the Ministry of Energy, Northern Development and Mines, Ontario, demonstrated elevated As concentrations (95 to 133 µg/L) that exceed the Canadian Council of Ministers of the Environment (CCME) guideline of 5 µg/L for the protection of freshwater aquatic life (CCME, 1997).

The study area is situated on the Canadian Shield and has a continental climate. The region experiences warm summers (average July temperature is 20 ºC) and cold winters (average January temperature is -12 ºC) with approximate seasonal range from -23 to 28 ºC. The average annual precipitation ranges between 660 and 1114 mm/yr (data from Sudbury, Ontario between 2000 and 2012, http://climate.weather.gc.ca).

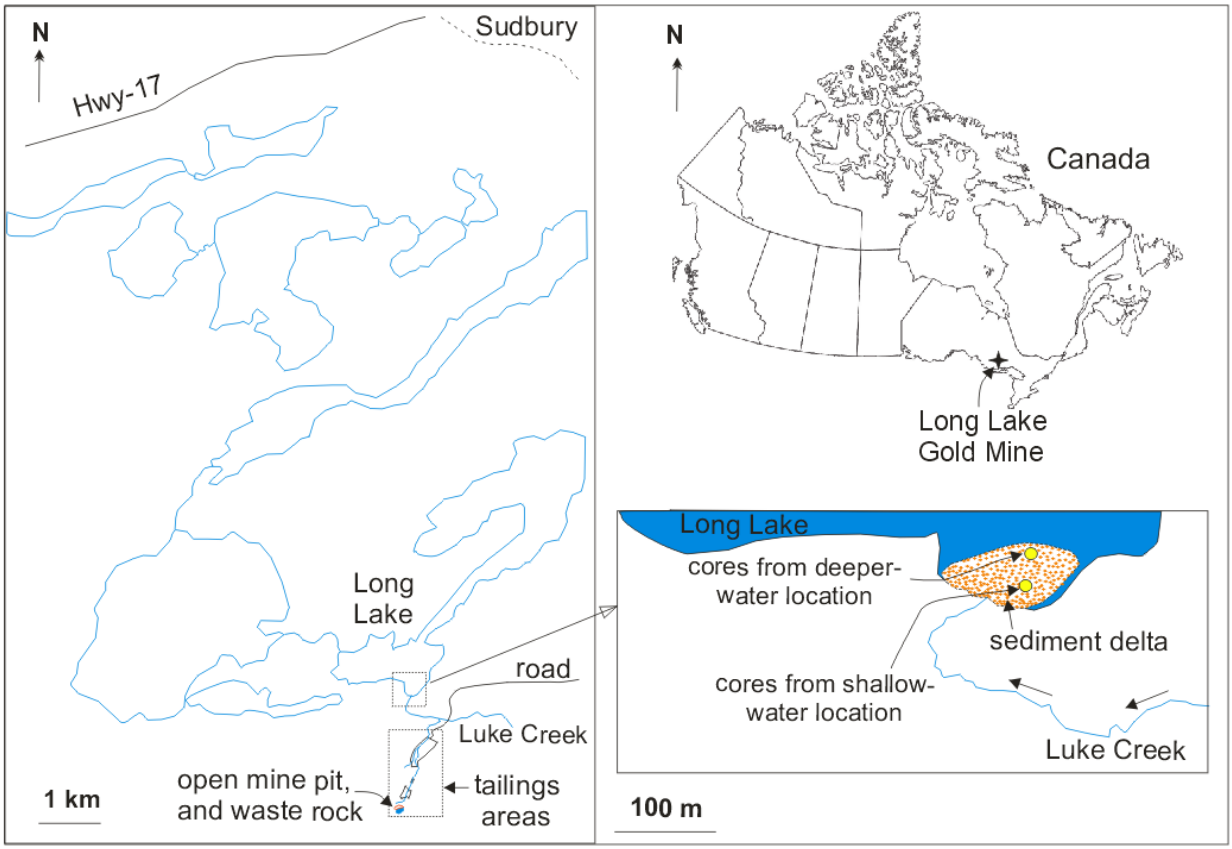

Fig. 3.1. Maps showing the location of the former Long Lake Gold Mine, and sample locations in the lake (lower right) (modified from Sapkota et al., 2023).

3.3. MATERIALS AND METHODS

3.3.1. Sample collection and preparation

In October 2018, sediment cores (0.051 m diameter, maximum depth of 2.2 m) were collected by scuba-diving from two locations: a shallow-water location in the sediment delta and a deeper-water location, approximately 90 m north from the mouth of Luke Creek (Fig. 3.1). Duplicate core samples were obtained from each location. The cores intersected mine-impacted sediment and the underlying natural sediment.

After core retrieval, the water above the sediment-water interface was drained and the cores were sealed to prevent oxidation or other chemical alteration of the sediment and porewater. A set of cores, one each from the shallow and deep locations, was designated for aqueous geochemical analysis. Within a few hours, these were sectioned into 0.1 m intervals in the field using an anerobic glove bag and the sub-samples were stored on ice during transportation to the laboratory where they were refrigerated at 4º C until porewater extraction was performed. The second of each duplicate set was split in half length-wise and dried in a N_2-purged anaerobic chamber for subsequent solid-phase geochemical and mineralogical analyses.

3.3.2. Sediment geochemistry

The sediment cores were sub-sampled at 2 cm increments. Two sets of samples (shallow core, n = 15; deep core, n = 33) were ground and homogenized with a mortar and pestle. A portion of each sample from the shallow and deep cores was subjected to digestion with aqua regia at 90 ºC for 12 hours. After the digestion, the samples were allowed to cool and the supernatant was separated from the solids by centrifugation at 3,000 rpm for 10 minutes, followed by dilution with deionized water. The resulting sample solutions were analyzed for total concentrations of As, Fe, S, K, Na, Al, Ca, Mg, Cu, Mn, Ni, Co, Cr, Zn, B, Sr, Pb, Ba, P, and Sb by Inductively-Coupled Plasma Optical-Emission Spectroscopy (ICP-OES) at the University of Ottawa. Another portion from each sample was treated with HCl at 80 ºC for eight hours to remove inorganic carbon, and then was dried at 60 ºC for 12 hours. The dried samples were mixed with tungsten oxide (WO_3) that acts as a combustion catalyst, flash-combusted at 1150 ºC in an elemental analyzer (Elementar vario EL cube, Germany) using ultra-pure helium as a carrier, and analyzed for organic carbon and nitrogen.

3.3.3. Aqueous geochemistry

The 0.1 m subsamples from the shallow and deep cores were transferred to 50 mL Nalgene centrifuge tubes in an anaerobic chamber. The tubes were capped and then porewater extraction was conducted by centrifugation with a Beckman J2-21M/E at 20,000 rpm for 10 minutes. After centrifugation, the samples were returned to the anaerobic chamber, and the porewater was separated from the sediment. Measurements of pH (Orion Ross pH electrode; Model 815600), Eh (Orion Platinum redox electrode; Model 9678 BN), and alkalinity were performed inside the chamber. The performance of the redox electrode was checked with ZoBell's solution (Nordstrom, 1977) and the values were referenced to the standard hydrogen electrode. For total alkalinity measurements, porewater samples were filtered through 0.45 μm cellulose-acetate membranes and titrated using a Hach Digital Titrator with 0.16 N or 1.6 N sulfuric acid and bromocresol green-methyl red indicator. Samples for geochemical analysis were also filtered (0.45 μm cellulose acetate) and those for cation determination were acidified to pH < 2.0 using trace-metal-grade nitric acid and analyzed by ICP-OES and Inductively-Coupled Plasma Mass Spectroscopy (ICP-MS).

Aqueous geochemical modelling was performed using PHREEQC (v. 3.6.1, Parkhurst and Appelo, 1999) with the WATEQ4F database (Ball and Nordstrom, 1991) to calculate mineral saturation indices and assess the potential for precipitation of selected Fe-oxyhydroxides, scorodite, and K/Na-jarosite.

3.3.4. Mineralogical characterization

Selected samples from shallow and deep cores, representing both the mine-impacted and natural sediments, were impregnated with low-viscosity epoxy resin (EPO-TEK 301 2FL), and

petrographic thin sections (~ 100 μm thick) were prepared using kerosene for polishing. The thin sections were carbon-coated and examined using Scanning Electron Microscopy (SEM, JEOL 6610LV) coupled with Energy-Dispersive X-ray Spectroscopy (EDS, Oxford Instruments INCA; University of Ottawa). Two samples were selected for detailed study with Transmission Electron Microscopy (TEM). The samples for TEM analysis (~ 10 μm x 30 μm x 0.1 μm) were prepared from petrographic thin sections using a focused ion beam (Ga ion source) at Fibics Incorporated, Ottawa, Ontario. A JEOL JEM-2100F analytical Scanning Transmission Electron Microscope (STEM; University of Ottawa) equipped with Gatan annular dark-field and bright-field detectors was used for imaging and mineralogical characterization of the secondary phases in the samples.

A Talos F200X (FEI Company; Canadian Centre for Electron Microscopy, McMaster University) operated at 200 kV was used to collect electron-energy loss spectroscopy (EELS) data for defining the Fe valence in μm-sized Fe-oxyhydroxides and to collect selected-area electron diffraction (SAED) patterns in support of mineral identification. Prior to collecting EELS data, in order to reduce the probability of interference from multiple scattering, relatively thin areas (< 100 nm) were identified by collecting low-energy-loss spectra (including zero-loss peak). The EELS spectrum images (47 x 17 pixels with a pixel size of 0.01 μm) were collected under the following conditions: collection angle = 23 mrad, beam current = 111 pA, energy dispersion = 0.15 eV/channel, energy resolution = 1.3 eV, and integration time = 0.3 seconds/pixel. After the spectrum images were collected, the Gatan Microscopy Suite (GMS) software was used to subtract the pre-edge background intensities (inverse power law). According to the method described by van Aken & Liebscher (2002) and Cavé et al. (2006), the pre-edge background-subtracted spectra were further processed using a double arctangent function to remove the post-edge background prior to calculating Fe L_3/L_2 intensity ratios and $Fe^{3+}/\Sigma Fe$. The SAED patterns were collected from

discrete phases in the samples after calibrating the camera length against a gold standard. The d-spacings were compared against those available in the American Mineralogist Crystal Structure Database (Downs and Hall-Wallace, 2003).

3.4. RESULTS

3.4.1. Sediment geochemistry

The sediment geochemistry is presented as elemental depth profiles through the mine-impacted sediment and into the natural pre-mining sediment (Fig. 3.2). In the near-shore region where the shallow core was collected, the mine-impacted zone is very thin (~0.3 m), likely because it is a relatively high-energy, wave-dominated environment and net sedimentation is low. Consequently, there are few samples in the mine-impacted zone and it is not possible to define clear trends. Nevertheless, it is apparent that concentrations of As, Fe, S, Cu, Ni, Zn, Na, K, Ba, C, and N are higher in the mine-impacted zone than the natural sediment. Similarly, at the deep core location, with the exception of Ca, Mg, and K, the concentrations of all reported elements are highest in the mine-impacted sediment (<1.75 m depth). Arsenic, Fe, and S are the principal mining-derived components and their concentrations in the mine-impacted sediment range from approximately 1 to 4 wt.%, 5 to 20 wt.% and 0.2 to 1.3 wt.%, respectively. In contrast, their concentrations in the natural sediment decrease to 0.03 – 0.09 wt.%, 0.9 – 1.8 wt.%, and 0.005 – 0.05 wt.%, respectively. The sample density in the mine impacted zone is higher at the deep-core location and a consistent trend is observed for most mine-impacted elements which is manifest by a distinct interval of relatively high concentrations between 1.75 and 1.25 m depth, and relatively low, but still elevated concentrations between 1.25 m and the surface. The As profile is unique in that it does not display a distinct deep versus shallow zonation of concentrations in the mine-impacted zone.

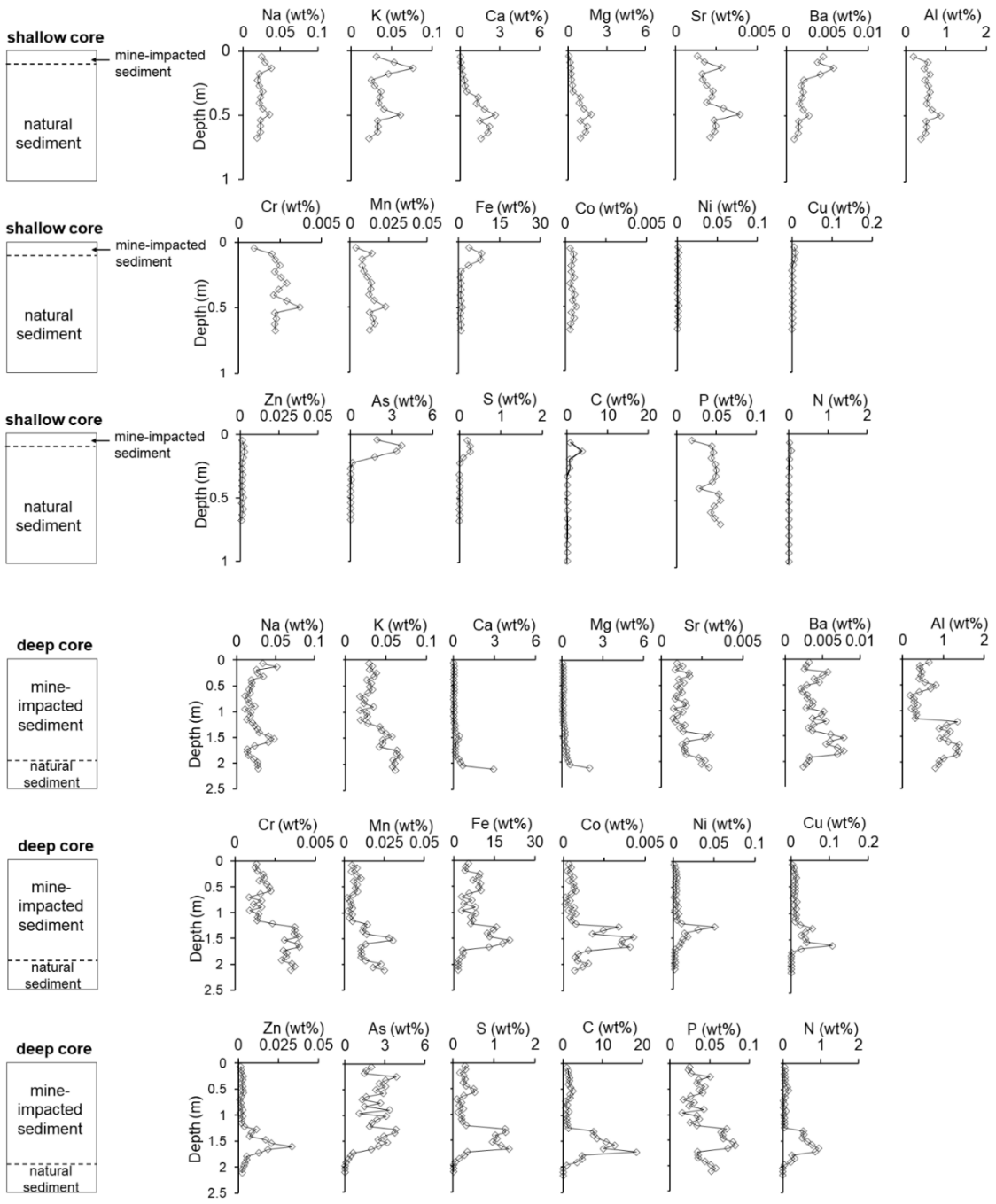

Fig. 3.2. Solid-phase geochemistry profiles for shallow and deep cores. The bottom portion of the shallow core was lost during core retrieval and sampling was limited to 1.0 m depth. The depth to mine-impacted sediment at both locations is indicated by dashed lines in the stratigraphic columns on the left.

3.4.2. Aqueous geochemistry

The porewater geochemistry analyses were conducted on samples from both the mine-impacted and natural sediment at the shallow location, but the permeability of the natural sediment at the deep location was low and it was not possible to extract water (Fig. 3.3). The porewater pH is circumneutral (6.7 to 7.2) with little variation versus depth at both locations. The Eh values range from -2 to 309 mV at the shallow location, with the lowest values at shallow depths near the mine-impacted zone followed by an abrupt increase to higher values at depth in the natural sediment. At the deep location where all data points are in the mine-impacted zone, the Eh values fall within the narrow range from -61 to 43 mV with little variation versus depth. Alkalinity, reported as meq HCO_3^-/kg_{H2O}, ranges from 2.17 to 10.96, with the highest values occurring at mid-depth at both locations. The concentrations of As are relatively high (0.31 to 1.22 $mmol/kg_{H2O}$) near the surface in the mine-impacted sediment, and at the shallow location they decline gradually with depth to minimum values (~0.17 $mmol/kg_{H2O}$) in the natural sediment. The concentrations of Fe are approximately 2.2 to 4.2 $mmol/kg_{H2O}$ in the mine-impacted sediment at both locations, but they decline to the lowest observed concentrations at depth in the natural sediment at the shallow location. The profiles for SO_4 display relatively high values (1.2 – 4.5 $mmol/kg_{H2O}$) near the surface and decrease with depth. Similar to As and Fe, the decreasing trend with depth is most pronounced in the natural sediment at the shallow location. With the exception of slightly elevated concentrations of K in the mine-impacted sediment (0.25 to 0.36 $mmol/kg_{H2O}$), there are few distinctive features in the profiles for the major and minor ions (Na, K, Ca, Mg, Mn, Sr, Al and Cl). Similarly, although Zn concentrations are slightly elevated in the mine-impacted sediment compared to the natural sediment porewater, the concentrations of heavy metals (Zn, Cr, and Co) are generally low (Zn <0.03, Cr <0.0002 and Co <0.0002 $mmol/kg_{H2O}$).

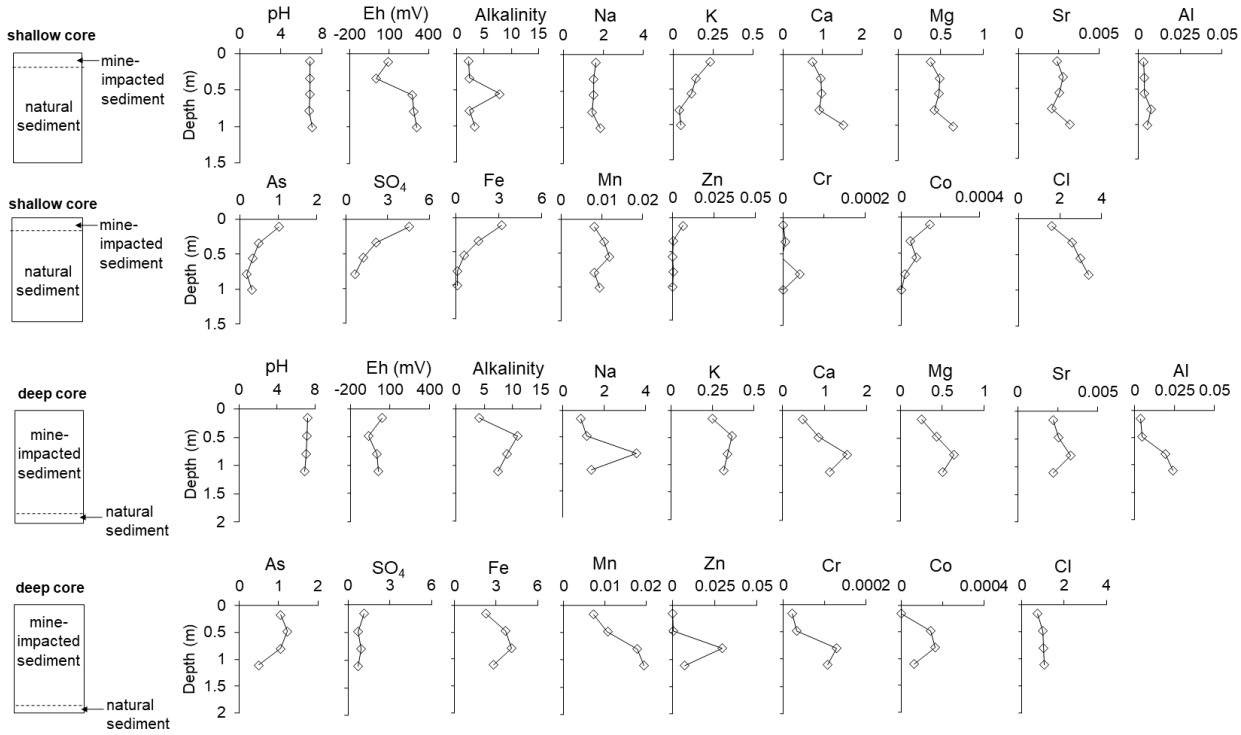

Fig. 3.3. Aqueous geochemistry concentration profiles (mmol/kg_{H2O} except for alkalinity which is in meq HCO_3^-/kg_{H2O}) for shallow and deep cores. The depth to mine-impacted sediment at both locations is indicated by dashed lines in the stratigraphic columns on the left.

Geochemical modelling of porewater data indicate the porewater in the mine-impacted sediment is supersaturated with respected to goethite and near-saturation or supersaturated with respect to ferrihydrite [as $Fe(OH)_3$ in the WATEQ4F database] (Fig. 3.4). However, the porewater in the mine-impacted sediment is undersaturated with respect to scorodite and K/Na-jarosite (Fig. 3.4).

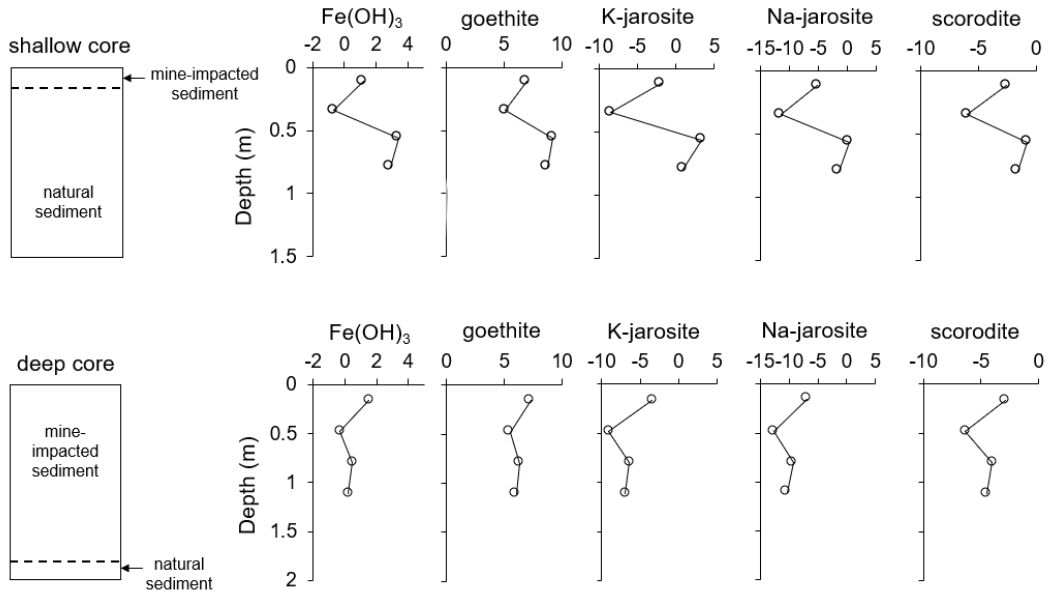

Fig. 3.4. Depth profiles of saturation indices for selected Fe-oxyhydroxides, K/Na-jarosite, and scorodite at the shallow and deep coring locations.

3.4.3. Mineralogical characterization

The depth of mine-impacted sediment at each coring location extends to approximately 0.3 m at the shallow location and 1.9 m at the deep location. The mine-impacted section is relatively thin at the shallow location, so the mineralogical investigation focussed on core from the deep location. A visual examination of the deep core shows that the top 0.2 m is yellowish-brown, transitioning to light-grey to 0.9 m, medium to dark brown between 0.9 and 1.7 m, medium grey between 1.7 m and 1.9 m, and grey from 1.9 to 2.2 m depth (Fig. 3.5). Thin section samples were collected from the mine-impacted sediment, the interface region between the mine-impacted sediment and the underlying natural sediment (Fig. 3.5).

3.4.3.1. SEM analysis

The SEM-EDS analysis indicates the presence of numerous fragments of tailings-derived cemented crusts in the mine-impacted sediment (Fig. 3.5), the abundance of which decreases with depth. The secondary minerals that form the cement in the fragments are porous and their composition is dominated by Fe-As-O, suggesting they are some form of ferric-arsenate. The ferric-arsenates commonly exhibit differences in brightness in backscattered electron images (Figs. 3.5A – B), indicating variable composition. A comparison between the cemented crusts in the tailings and these fragments that have been transported to the sediment is provided in Figure 3.6. The sediment-hosted fragments are relatively porous compared to those in the tailings, and EDS analyses reveal that the As/Fe ratios in the sediment-hosted crusts are low and variable (As/Fe ~ 0.3 – 6.0; n = 20) compared to those in the tailings (As/Fe ~ 6.2 – 9.4; n = 15) (Fig. 3.6).

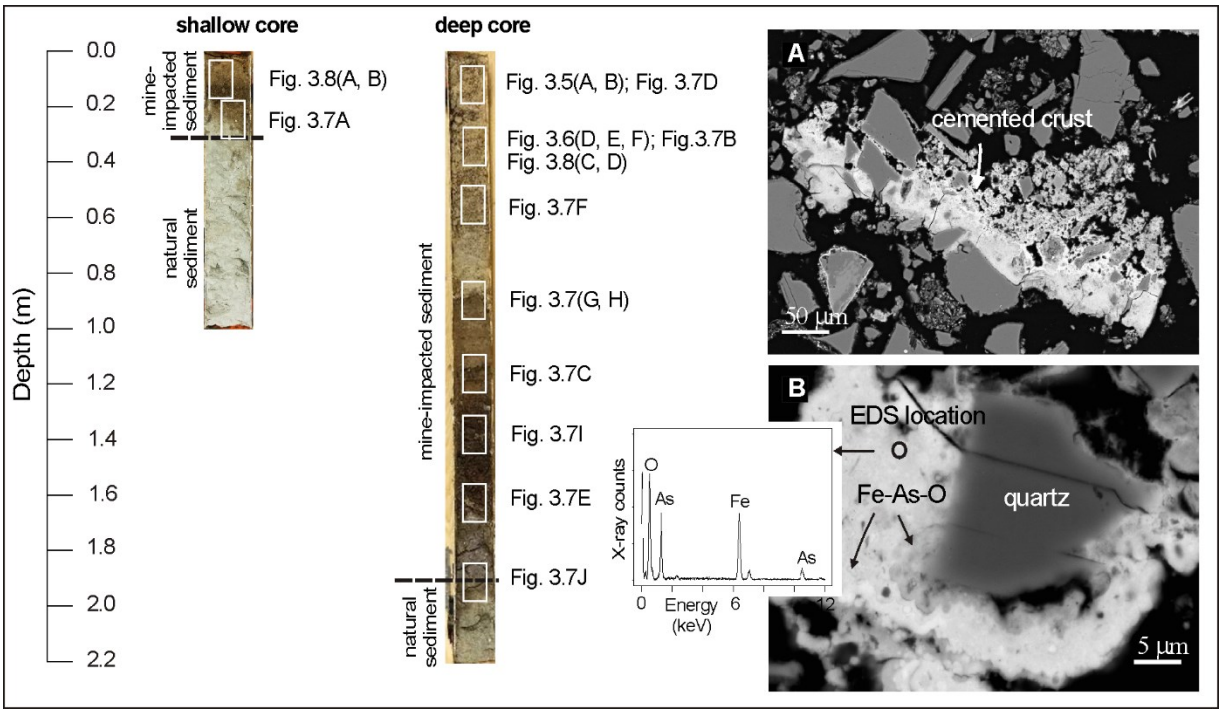

Fig. 3.5. (Left) Photographs of the cores from the shallow and deep coring locations showing colour gradations in the mine-impacted sediment overlying the natural sediment. White rectangles indicate locations where thin section samples were collected for mineralogical analyses. (Right) (A) Backscattered-electron SEM image from the mine-impacted sediment at the deep coring location shows a fragment of cemented crust that has been transported from the tailings. The cementing minerals commonly display variations in brightness as demonstrated by the material surrounding a quartz grain in (B). EDS analyses of the secondary minerals in the crust indicate they are ferric-arsenate.

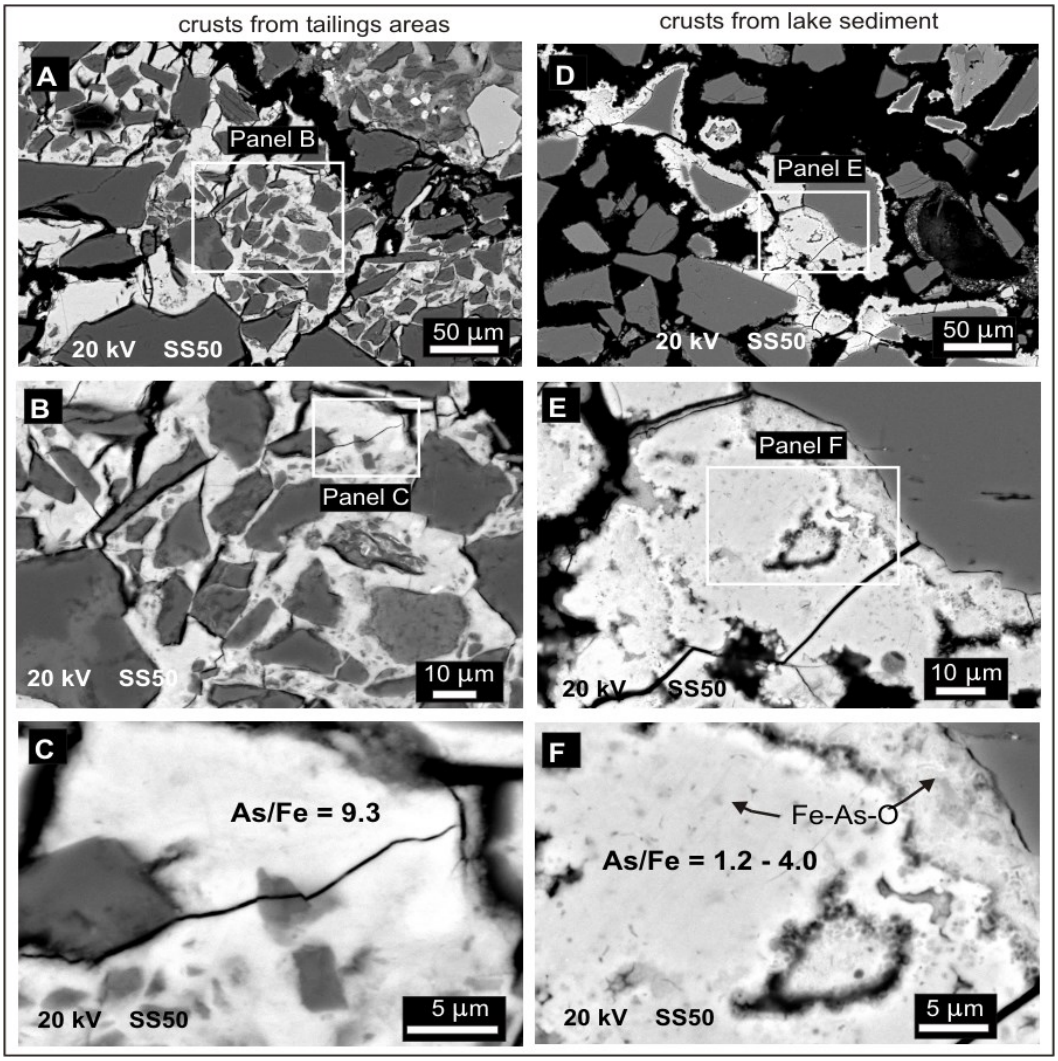

Fig. 3.6. Backscattered-electron SEM images of the cemented crusts from the tailings (A – C) and the lake sediment (D – F). White rectangles represent magnified regions corresponding to B and C (crusts from the tailings areas), and E and F (crusts from lake sediment). The SEM images were collected under the same operating conditions to compare morphology and As/Fe ratios between the crusts. The images in panels C and F indicate that the crusts in the tailings are relatively uniform compared to the residual crusts in the sediment that are porous and embayed. The EDS analyses demonstrate that As/Fe ratios are relatively low and variable in the sediment-hosted crusts (As/Fe ~ 0.3 – 6.0; n = 20) compared to the crusts in the tailings (As/Fe ~ 6.2 – 9.4; n = 15).

The SEM-EDS analysis reveals the presence of diagenetic products within the mine-impacted sediment. These products primarily include Fe-oxyhydroxides (Figs. 3.7A – H) which are distributed throughout the mine-impacted sediment. They exhibit diverse morphologies (e.g., banded, fibrous, spherulitic), vary in size from nm to μm, and commonly contain small amounts of As. They occur separately or in proximity to the fragmented crusts. The occurrence of Fe-oxyhydroxides that consist of aggregates of nm- to μm-sized crystals arranged in spherulitic form (Fig. 3.7A – E) is unique as they have not been reported in earlier studies. These spherulitic Fe-oxyhydroxides range in diameter from 8 to 45 μm, and consist of subhedral crystals that occupy 54% to 98% of the spherule volume (assumes cross-sectional area corresponds to volume). Based on limited cross-sectional images, the microcrystals do not appear to form recognizable patterns, and the separation between them varies from < 0.1 μm (Fig. 3.7A) to 1.5 μm (Fig. 3.7B – 3.7D). The EDS analyses indicate the composition of crystallites is dominated by Fe-O (Fig. 3.7A); however, due to analytical-volume constraints on resolution with SEM-EDS (~2 – 3 μm), the compositions of some crystallites and the interstitial spaces could not be distinguished. Additional diagenetic products include As- and Fe-sulfides (Fig. 3.7I – J). They occur at depths between 1.4 and 1.9 m in the mine-impacted sediment. As-sulfides are relatively abundant compared to Fe-sulfides, some of which occur as framboidal pyrite (Fig. 3.7J).

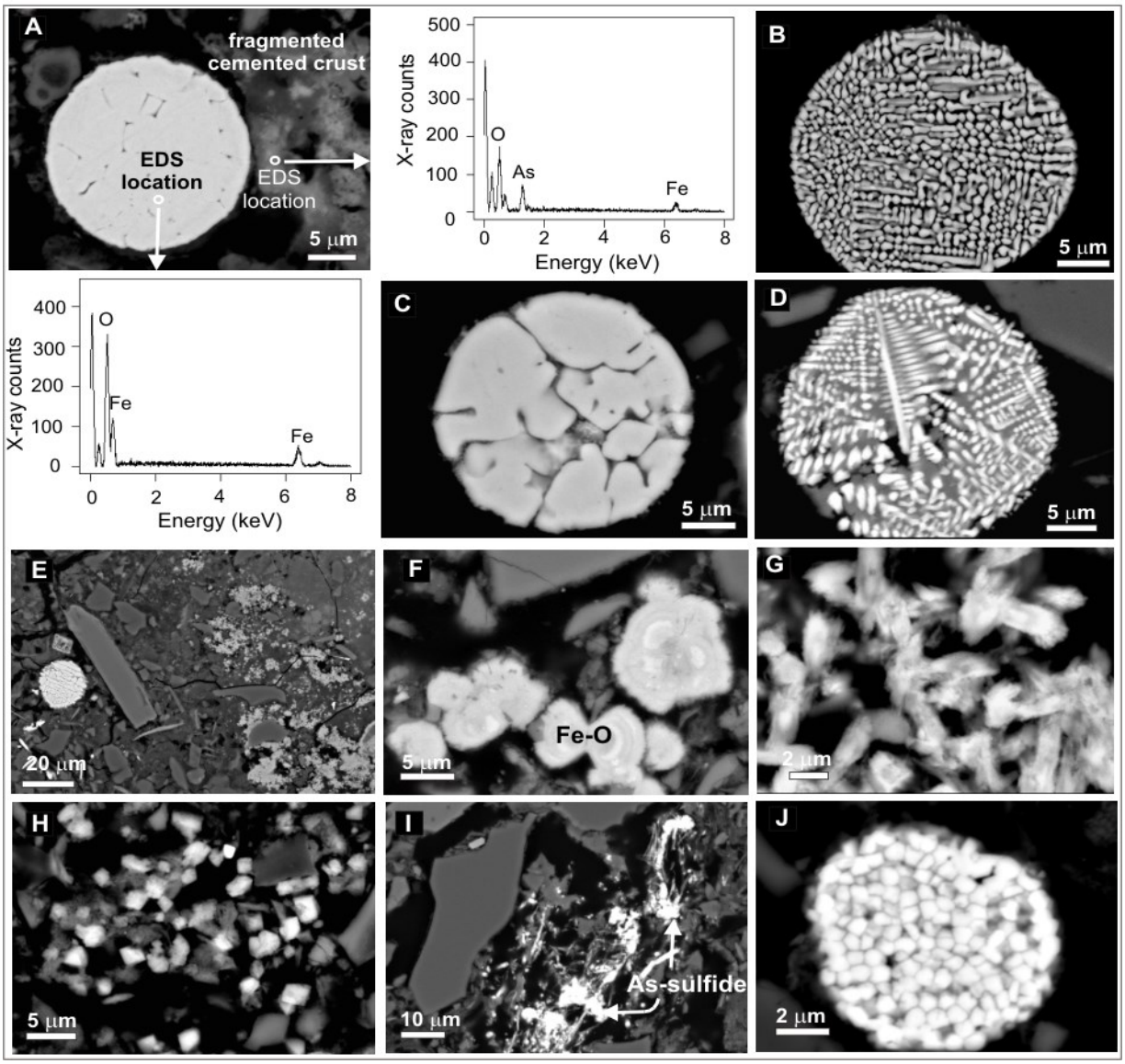

Fig. 3.7. Backscattered electron images showing diagenetic products within the mine-impacted sediment (locations are indicated beside white rectangles in Fig. 3.5). Fe-oxyhydroxides display diverse morphologies including spherulitic (A – E), radially-zoned semi-spherical clusters (F), and lathe and prismatic (G, H). The secondary sulfides include As-sulfides (I) and Fe-sulfides, some of which precipitate in framboidal form (J). The EDS spectra collected from the microcrystals and the surrounding crust material in panel A indicate that the spherulitic microcrystals consist of Fe-O while the residual crust contains Fe-As-O.

3.4.3.2. STEM analysis

Two spherulitic Fe-oxyhydroxides were selected for STEM-EDS analysis: i) spherule-1, which is located adjacent to a fragment of crust, and ii) spherule-2, which is not directly surrounded by crust (Fig. 3.8). One TEM sample transects a portion of spherule-1 and its surrounding crust (Fig. 3.8B) while the other transects the full diameter of spherule-2 (Fig. 3.8D). The STEM-EDS analysis reveals that spherule-1 consists of interlocking, μm-sized crystals with minimal (<0.1 μm) interstitial separation between crystals. The STEM annular-dark-field (STEM-ADF) images in Figure 3.9 show the boundary between spherule-1 and the surrounding crust. The STEM-EDS analysis conducted on a microcrystal from spherule-1 (Fig. 3.9B) indicates that it contains Fe-O (Fig. 3.9C). The analyses conducted along a transect from near the edge of spherule-1 outward to the surrounding crust (Fig. 3.9B) indicate that the near-edge material has a composition dominated by Fe-O, while the crust contains Fe-As-O (Fig. 3.9D). Consistent with SEM-EDS analyses of the crusts, the STEM-EDS X-ray count ratios for As and Fe in the crust are low, ranging between 0.8 and 1.5. Spherule-2 also consists of μm-sized, subhedral crystals (Fig. 3.10A). The STEM-EDS analyses indicate that these microcrystals are composed of Fe-O with small amounts of Ni (Fig. 3.10C). The interstitial spaces contain a Si-O phase.

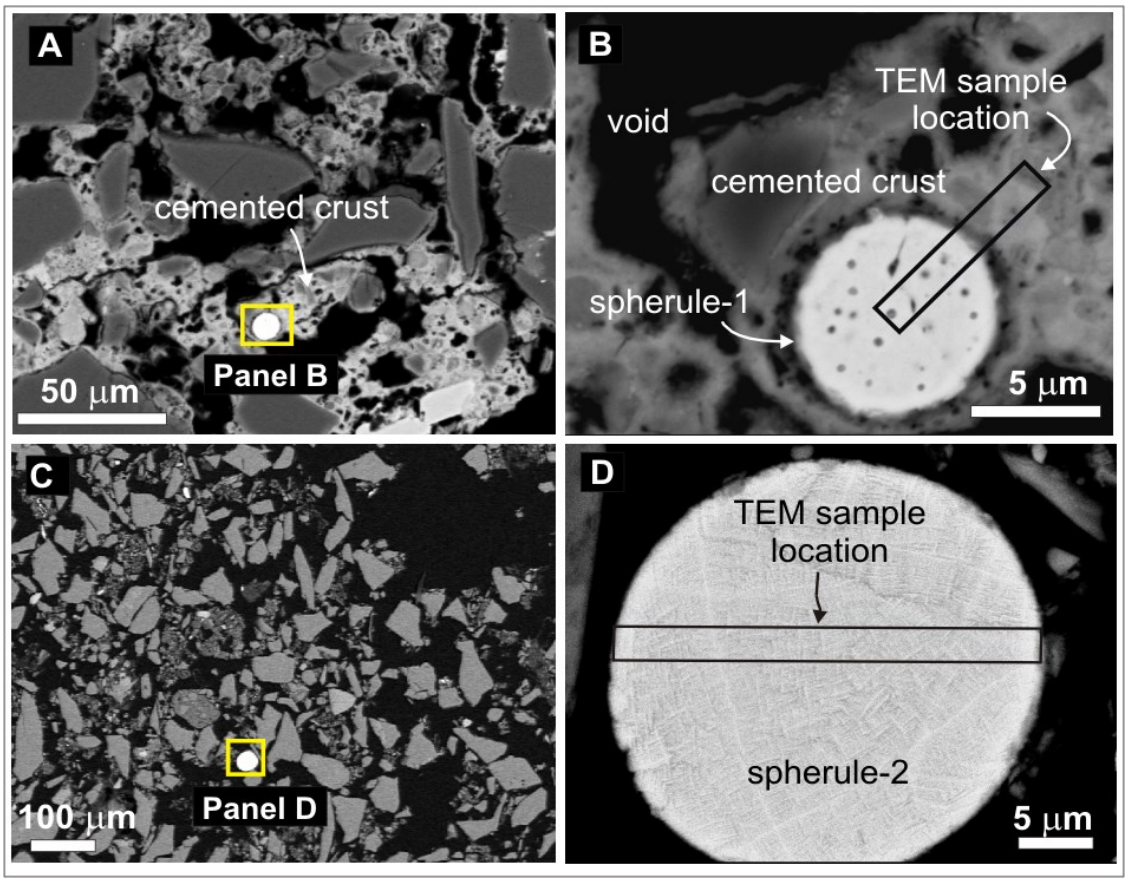

Fig. 3.8. (A, C) Backscattered-electron images showing the locations of two spherules selected for STEM analysis. Yellow rectangles represent magnified regions corresponding to B and D. Spherule-1 is within a fragment of crust (B) whereas spherule-2 is not directly surrounded by the crust (D).

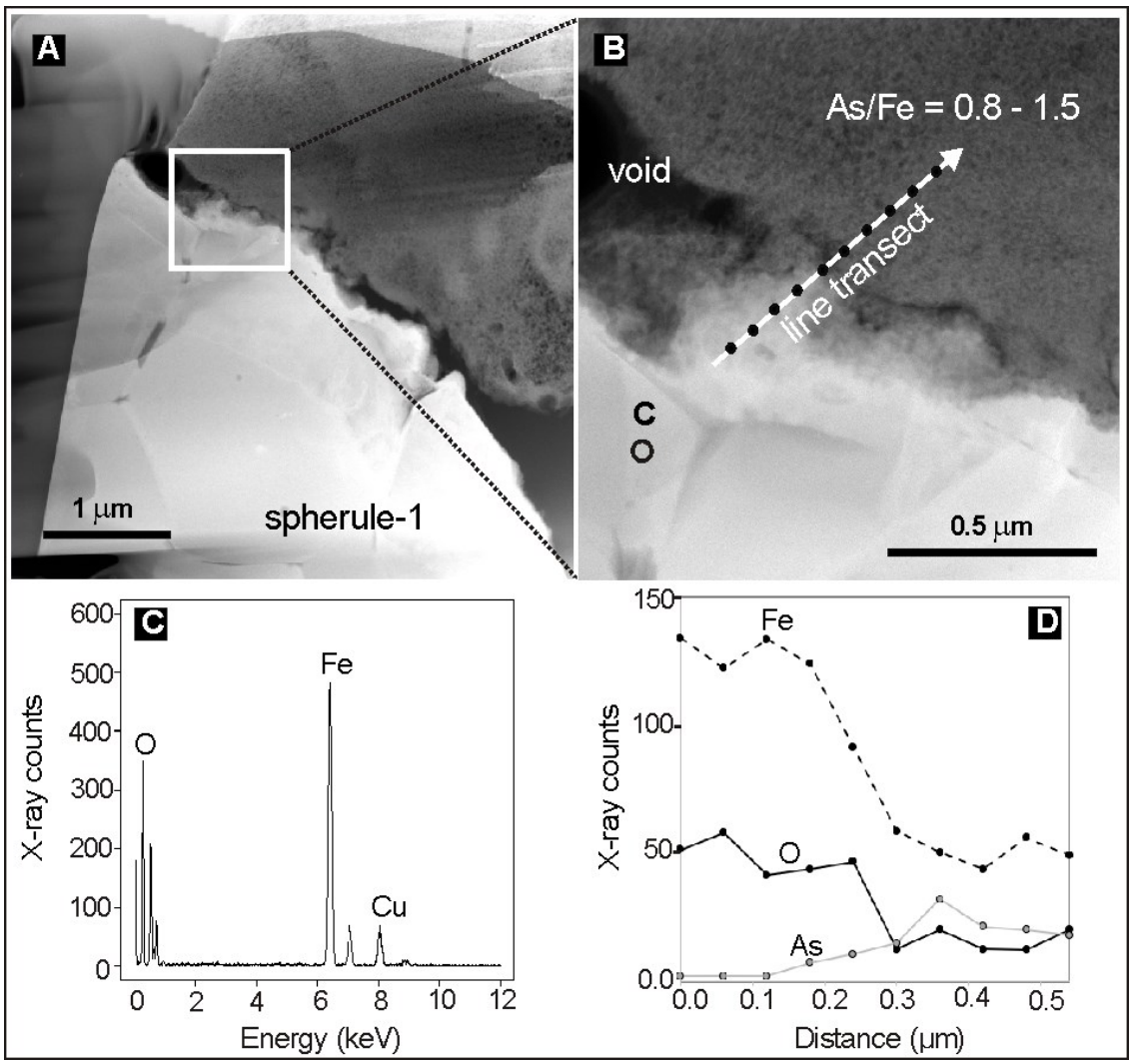

Fig. 3.9. (A) STEM-ADF image showing the boundary between spherule-1 and the surrounding crust. (B) STEM-ADF image showing locations of STEM-EDS analyses, including a spot analysis on a microcrystal from spherule-1 and an analytical transect from near the spherule's edge outward to the residual crust. (C) STEM-EDS analysis on the microcrystal indicates that it is composed of Fe-O; Cu peak is due to spurious X-rays from the sample holder. (D) STEM-EDS analytical profiles along the transect shown in B demonstrate that the composition of the material near the edge of the spherule is Fe-O while the surrounding material consists of Fe-As-O. The As/Fe X-ray count intensity ratios in the surrounding crust range from 0.8 to 1.5.

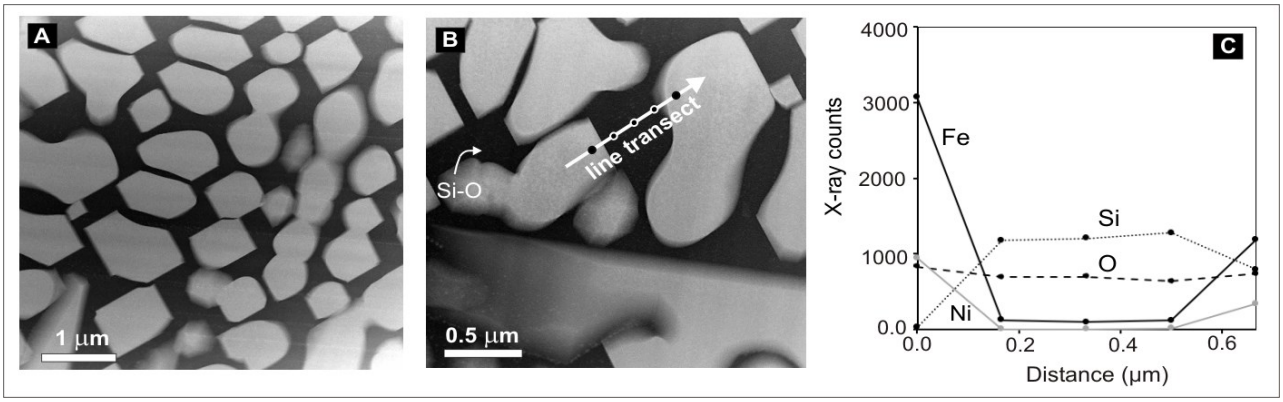

Fig. 3.10. (A) STEM-ADF image from a portion of spherule-2 illustrating subhedral, μm-sized crystals. (B) STEM-ADF image showing the location of a STEM-EDS analytical transect. (C) STEM-EDS analyses demonstrate that the microcrystals consist of Fe-O with some Ni, and the interstitial space is filled with a Si-O phase.

A SAED pattern obtained from a microcrystal in spherule-2 is presented in Figure 3.11. The d-spacings obtained from the Fe-O phase are consistent with lepidocrocite, but the SAED patterns collected from the Si-O phase exhibit diffuse rings, indicating that it is amorphous.

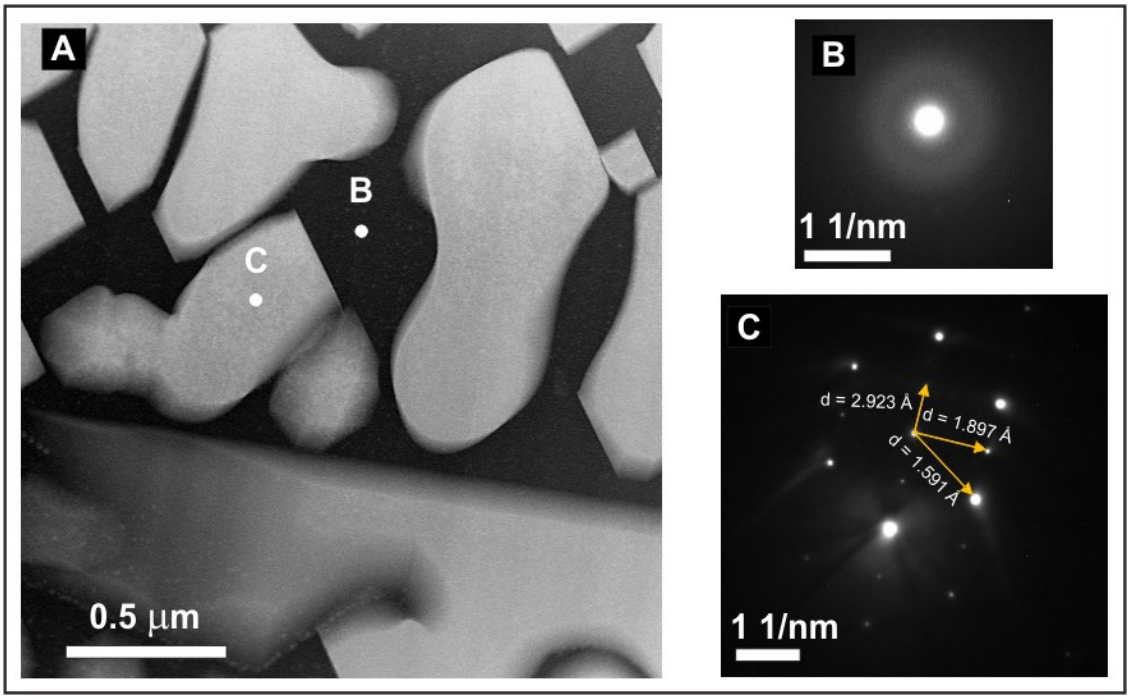

Fig. 3.11. (A) STEM-ADF image showing a portion of spherule-2. (B) The SAED pattern from the Si-O phase filling the interstitial spaces displays diffuse rings indicating that it is amorphous. (C) The d-spacings determined from a SAED pattern of a microcrystal correspond to lepidocrocite.

An EELS spectrum showing the Fe $L_{3,2}$ white lines obtained from a working area within a microcrystal in spherule-2 is presented in Figure 3.12. The background corrections were conducted according to the method described by van Aken et al. (1998) and Cavé et al. (2006). Quantification of Fe valence was done using the calibration derived by Cavé et al. (2006) that relates $Fe^{3+}/\Sigma Fe$ in Fe-minerals to variations in L_3/L_2 intensity ratios. This approach indicates that $Fe^{3+}/\Sigma Fe$ in the microcrystal is 0.8 and Cavé et al. (2006) report that the error on these measurements ranges from 4 to 7 %. These results suggest that the microcrystals contain mixed Fe-valence, predominantly Fe^{3+} which accounts for approximately 80% of the total Fe concentration.

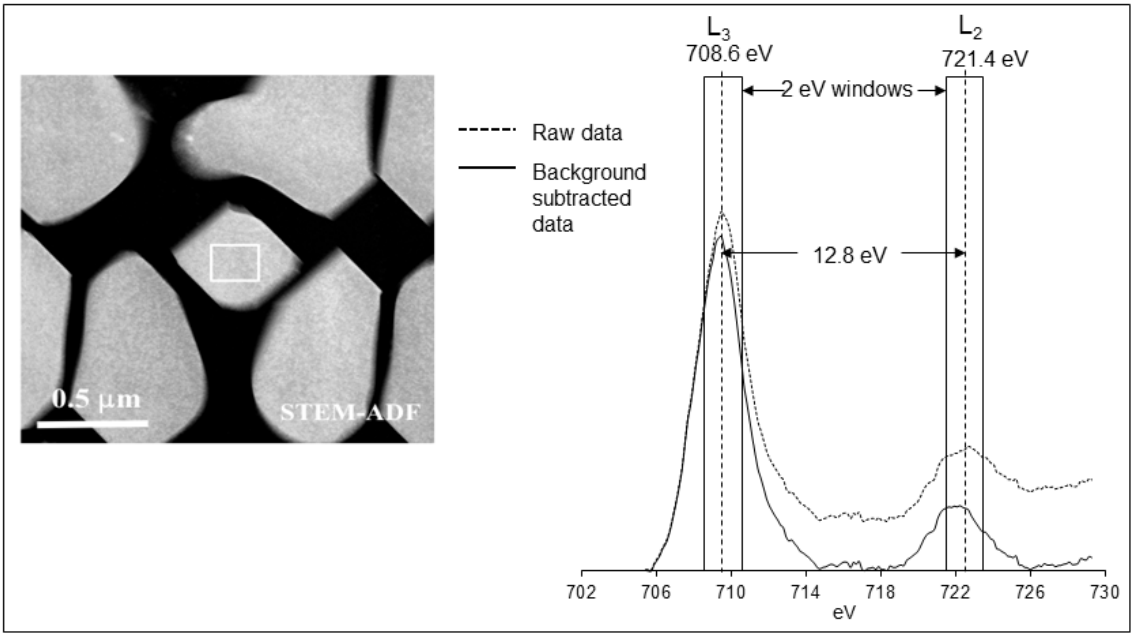

Fig. 3.12. (Left) STEM image showing the EELS measurement area (rectangle) in a microcrystal from spherule-2. (Right) Background-subtracted near-edge EELS spectrum showing the 2 eV integration windows used to calculate $Fe^{3+}/\Sigma Fe$. Dashed and solid lines represent data following power-law background subtraction and final data following white-lines background removal, respectively.

3.5. DISCUSSION

The solid-phase geochemical analyses indicate that As, Fe, and S are enriched in the mine-impacted sediment at both locations (Fig. 3.2). Their enrichment can be attributed to the erosion and transport of pyrite and arsenopyrite (the principal sulfide minerals in the Long Lake tailings) and ferric-arsenate and K/Na-jarosite-bearing cemented crusts from the tailings areas to Luke Creek and into the lake (Sapkota et al., 2023). A similar explanation accounts for the elevated concentrations of Cu, Mn, Co, Ni, and Zn in the mine-impacted sediment at both locations, as these elements are commonly found in elevated concentrations in sulfide-rich mine tailings (McGregor

and Blowes, 2002; Sidenko et al., 2007; Lindsay et al., 2009, 2015). At the deep location, concentrations of As, Fe, S, Cu, Mn, Co, Ni, and Zn are highest between 1.75 m and 1.25 m depth and above that depth they decline to lower, but still elevated concentrations (Fig. 3.2). This step-like decrease in tailings-derived components indicates a reduced influx of tailings-derived material that likely corresponds in time to construction of a sand cover on the tailings in the early 1970s. Similarly, there is an abrupt step-like increase in C, N, and P concentrations between 1.75 and 1.25 m depth which likely corresponds to mining-related land clearing and disruption of wetlands and the decrease in concentrations above 1.25 m depth may be attributed to remedial efforts in the early 1970s to reduce sediment erosion and transport to the lake.

The pH values indicate near-neutral conditions and the Eh measurements suggest suboxic to anoxic conditions in the mine-impacted sediment (Fig. 3.3). Geochemical modelling results display undersaturation with respect to scorodite and K/Na-jarosite in the porewater (Fig. 3.4) indicating that they are thermodynamically unstable in this setting. Mineralogical observations support the modelling results in that, compared to the crusts from the tailings, the crusts in the lake sediment are relatively porous and embayed, suggesting they have undergone partial-dissolution following burial (Figs. 3.5 – 3.6). Under similar conditions, scorodite dissolution has been reported by Zhu and Merkel, (2001) and Bluteau and Demopoulos, (2007), and jarosite dissolution has been reported by Al et al. (1994) and references therein. Partial-dissolution of scorodite and K/Na-jarosite contribute to elevated aqueous concentrations of As, Fe, K, and SO_4 (Fig. 3.3), creating a concentration gradient that can drive their diffusive transport upward into the lake water, and downward into the underlying natural sediment. At the shallow coring location, the decline in As, Fe, K, and SO_4 aqueous concentrations in the porewater of the natural sediment displays diffusion-like profiles but the sampling resolution is too coarse to observe a similar upward decline due to

diffusion. At the deep core location where sampling resolution is higher in the mine impacted sediment, the aqueous concentrations of As, Fe, and K decline between 0.5 m depth and the surface, consistent with diffusive transport of dissolution products toward the lake. The concentrations of As and Fe, and to a lesser extent K, also decline with depth below 0.5 to 0.75 m depth. This could reflect downward transport by diffusion but the trend may be enhanced by bacterial SO_4 reduction and precipitation of insoluble Fe- and As-sulfides (Fig. 3.7).

Given the suboxic to anoxic conditions in the mine-impacted sediment, it was not expected that Fe-oxyhydroxides would be a common diagenetic reaction product (Fig. 3.7). They form throughout the depth of the mine-impacted sediment, from near the sediment surface to depth intervals where secondary Fe- and As-sulfides are formed (Figs. 3.5, 3.7). The principal tailings-derived reactive phases that are most likely to be diagenetically transformed are scorodite, amorphous ferric-arsenate, and K/Na-jarosite (Sapkota et al., 2013). Previous studies (Zhu and Merkel, 2001; Bluteau and Demopoulos, 2007) suggest on the basis of thermodynamic geochemical modelling that scorodite can undergo abiogenic incongruent dissolution in circumneutral freshwater, releasing Fe(III) and As(V). However, in suboxic to anoxic environments, microbially-mediated reductive dissolution of scorodite can be the dominant mechanism, as demonstrated by several microcosm-based studies (Newman et al., 1998; Nicholas et al., 2003; Revesz et al., 2015). Furthermore, when both dissimilatory As-reducers (e.g., *Bacillus* sp.) and Fe-reducers (e.g., *Shewanella* sp.) coexist, dissimilatory As(V)-reduction has been observed to precede Fe(III)-reduction (Nicholas et al., 2003; Campbell et al., 2006). For instance, Campbell et al. (2006) demonstrated that dissimilatory As(V)-reduction preceded Fe(III)-reduction in sediment incubations (amended with lactate and acetate and those without amendment). These and other studies (e.g. Cummings et al., 1999; Kneebone et al., 2002; Islam et al., 2004, 2005; Das

et al., 2016) describe a variety of mechanisms for the release of As and Fe from As-Fe-rich sediments, and that biogeochemical cycling of Fe and As are closely interconnected.

In this study, analyses of the buried crust fragments provide evidence for dissolution of scorodite and ferric-arsenate. The crusts contained in the mine-impacted sediment are porous and exhibit partial-dissolution features, and they have relatively low As/Fe ratios compared to the crusts in the tailings (Fig. 3.6), indicating preferential As-depletion. In the event that As(V) in scorodite or ferric-arsenate is reduced to As(III) causing destabilization of the solid phase, some of the Fe(III) could be liberated to the aqueous phase. Ferrihydrite, which is commonly found to be the main diagenetic product from the reductive dissolution of scorodite (Nicholas et al., 2003; Revesz et al., 2015 and references therein), is then likely to form. This inference is supported by geochemical modelling (Fig. 3.4) which indicates porewater saturation indices for scorodite and ferrihydrite [$Fe(OH)_3$] are below zero and near zero or above, respectively, in the mine impacted sediment. Subsequent transformation of ferrihydrite may occur forming more stable Fe-oxyhydroxides such as goethite and lepidocrocite (Cornell et al., 1989; Cudennec and Lecerf, 2006; Guo and Barnard, 2013; Schulz et al., 2022). Hu et al. (2020) conducted experiments on Fe(II)-catalyzed transformation of ferrihydrite and observed that lepidocrocite precipitation was favoured over goethite in conditions with elevated aqueous As concentrations.

At circumneutral pH conditions, phase transformations between Fe(III)-minerals can proceed in the presence of a catalyst such as aqueous Fe(II) (Pederson et al., 2005; Yee et al., 2006; Boland et al., 2014; Qafoku et al., 2020). These studies suggest that the Fe(II)-catalyzed transformation involves the adsorption of Fe(II) ions from the solution onto the freshly-formed Fe(III)-mineral (e.g., ferrihydrite). The sorbed Fe(II) is a strong reducing agent and is rapidly oxidized, but as a catalyst, it decreases the activation energy barrier of the Fe(III)-mineral

transformation. The electron that is lost from the adsorbed Fe(II) is transferred to an adjacent atom of the Fe(III)-mineral and causes a local instability in its crystal structure before its release to the solution as Fe(II). The adsorbed and oxidized Fe precipitates in the form of a more stable Fe-oxyhydroxide. Elevated aqueous Fe(II) concentrations in the Long Lake sediment porewater (Fig. 3.3) are likely generated by the reductive dissolution of Fe(III)-minerals in the tailings-derived crust fragments, and may catalyze ferrihydrite phase transformations.

3.5.1. Evolution of spherules

Some of the Fe-oxyhydroxides in the mine-impacted sediment display spherulitic textures that resemble framboidal pyrite. The formation of framboidal pyrite is a well-studied topic and it's possible that a similar mechanism is involved in the formation of the spherules. In the literature, biogenic and abiogenic models have been proposed to explain the origin of the framboidal habit of pyrite. The biogenic model suggests that formation of framboidal pyrite requires the presence of fossilized microbial remains (for a summary, see Folk, 2005). However, several experimental studies have successfully produced pyrite framboids in the absence of bacteria (see review by Ohfuji and Rickard, 2005), and the abiogenic model seems to have gained acceptance. The abiogenic model considers precipitation from solutions supersaturated with respect to Fe and S (Merinero et al., 2009). For pyrite framboids to form, a large number of separate Fe-S-bearing nuclei are thought to form simultaneously - a mechanism described as 'burst nucleation' (Baronov et al., 2015; Rickard, 2021) - and the crystals aggregate to minimize the free energy of the system.

In the Long Lake sediment, it is possible that preferential As(V)-reduction destabilized the ferric-arsenate structure, liberating Fe(III) and leading to supersaturation with respect to lepidocrocite. A burst-nucleation mechanism could result in nucleation and growth of the lepidocrocite microcrystals, and minimization of the surface-free-energy to volume ratio would

cause aggregation in spheroidal form. In the reducing environment of the lake sediments, some Fe(II) might substitute for Fe(III) during growth, consistent with the measured Fe(III)/ΣFe = 0.8 in spherule-2. Growth of microcrystals may continue until the interstitial spaces between the microcrystals have grown together or are filled with a cementing mineral such as the secondary silica observed in the Long Lake spherules. The role of silica in the formation of the spherules is uncertain, but it may be more than coincidence that the amorphous silica in the interstitial space of spherule-2 (Fig. 3.10) is almost pure. Schulz et al. (2022) report that in the presence of aqueous silica, Fe(II)-catalyzed transformation of ferrihydrite leads to the formation of lepidocrocite, but in their experiments the lepidocrocite formed directly in contact with the ferrihydrite precursor. Reardon (1979) reports on the formation of Fe(III)-silica complexes and their role in increasing Fe(III) solubility and mobility in natural waters. Pokrovski et al. (2003) used X-ray spectrometry to demonstrate that aqueous silica inhibits polymerization of Fe(III), thereby increasing its stability and mobility in natural waters. Iron-silica complexation could explain how Fe(III) can be transported from the surface of the dissolving crusts to the point of nucleation and growth of the spherules, which may be well separated in space (Fig. 3.8). However, the mechanism for destabilizing the Fe(III)-silicate complexes to allow nucleation and growth of lepidocrocite remains unclear.

3.6. CONCLUSIONS

The geochemical and mineralogical study of the Long Lake sediments demonstrates that the erosion and transport of pyrite, arsenopyrite, and ferric-arsenate and K/Na-jarosite-bearing cemented crusts from the tailings areas into the lake cause enrichment of As, Fe, S, Cu, Mn, Co, Ni, and Zn in the sediment delta to approximately 0.3 m at the shallow location and 1.9 m at the deep location. Their solid-phase concentrations are highest between 1.75 m and 1.25 m depth and

above that depth they decline to lower concentrations, indicating a reduced influx of tailings-derived material that likely corresponds in time to construction of a sand cover on the tailings. Mineralogical analyses of ferric-arsenate minerals in the sediment-hosted crusts display partial-dissolution features and relatively low As/Fe X-ray count ratios compared to the crusts in the tailings, indicating preferential As-depletion. This inference is also supported by enriched aqueous concentrations of As and Fe, and by geochemical modelling that indicates undersaturation of the sediment porewater with respect to scorodite. Fe-oxyhydroxides are common diagenetic reaction products in the mine-impacted sediment and they occur from near the sediment surface to depths where secondary Fe- and As-sulfides form, suggesting they formed in suboxic to anoxic conditions. They vary in size from nm to µm, and exhibit diverse morphologies, including a unique spherulitic form that consists of lepidocrocite microcrystals.

Data availability

Data are available through Mendeley Data at:
https://data.mendeley.com/preview/szbb4tz7rb?a=01425f2a-8450-4ece-b387-27e2bcd5e233

Acknowledgements

The funding for this study was provided by the Natural Sciences and Engineering Research Council of Canada (NSERC) through the Strategic Partnership Grants for Networks Program, 'Toward Environmentally Responsible Resource Extraction Network' (NSERC TERRE-NET, NETGP 479708-15), awarded to David W. Blowes and collaborators. We thank Simon Hayles for assistance with sampling sediment cores.

References

Al, T., Blowes, D. W., Jambor, J. L., Scott, J. D., 1994. The geochemistry of mine-waste pore affected by the combined disposal of natrojarosite and base-metal sulphide tailings at Kidd Creek, Timmins, Ontario. Canadian Geotechnical Journal 31, 502–512.

Baronov, A., Bufkin, K., Shaw, D. W., Johnson, B. L., Patrick, D. L., 2015. A simple model of burst nucleation. Physical Chemistry Chemical Physics 17, 20846–20852.

Ball J. W. and Nordstrom D. K., 1991. WATEQ4F–User's manual with revised thermodynamic data base and test cases for calculating speciation of major, trace and redox elements in natural waters. U.S. Geological Survey, Open File Report 91–183.

Bluteau, M. C. and Demopoulos, G. P., 2007. The incongruent dissolution of scorodite – solubility, kinetics and mechanism. Hydrometallurgy 87, 163–177.

Boland, D. D., Collins, R. N., Miller, C. J., Glover, C. J., Waite, T. D., 2014. Effect of solution and solid-phase conditions on the Fe(II)-accelerated transformation of ferrihydrite to lepidocrocite and goethite. Environmental Science and Technology 48, 5477–5485.

Bonneville, S., Van Cappellen, P., Behrends, T., 2004. Microbial reduction of iron(III) oxyhydroxides: Effects of mineral solubility and availability. Chemical Geology 212, 255–268.

Campbell, K. M., Malasarn, D., Saltikov, C. W., Newman, D. K., Hering, J. G., 2006. Simultaneous microbial reduction of ion(III) and arsenic(V) in suspensions of hydrous ferric oxide. Environmental Science and Technology 40, 5950–5955.

Cavé, L., Al, T., Loomer, D., Cogswell, S., Weaver, L., 2006. A STEM/EELS method for mapping iron valence ratios in oxide minerals. Micron 37, 301–309.

CCME (Canadian Council of Ministers of the Environment), 1997. Canadian Water Quality Guidelines for the Protection of Aquatic Life.

CH2M HILL, 2014. Site Characterization report and data analysis - Long Lake Gold Mine tailings areas, Eden Township, Ontario. Final Technical Report Prepared for Ontario Ministry of Northern Development and Mines.

Coey, J. M. D., Schindler, D. W., Weber, F., 1974. Iron compounds in Lake Sediments. Canadian Journal of Earth Sciences 11, 1489–1493.

Cornell, R.M. and Schwertmann, U., 2003. The iron oxides: structure, properties, reactions, occurrences and uses. Second Ed., Wiley-VCH, Weinheim.

Cornell, R. M., Schneider, W., Giovanoli, R., 1989. Phase transformations in the ferrihydrite/cysteine system. Polyhedron 8, 2829–2836.

Couture, R. M., Gobeil, C., Tessier, A., 2010. Arsenic, iron and sulfur co-diagenesis in lake sediments. Geochimica et Cosmochimica Acta 74, 1238–1255.

Crowe, S. A., Roberts, J. A., Weisener, C. G., Fowle, D. A., 2007. Alteration of iron-rich lacustrine sediments by dissimilatory iron-reducing bacteria. Geobiology 5, 63–73.

Cudennec, Y. and Lecerf, A., 2006. The transformation of ferrihydrite into goethite or hematite, revisited. Journal of Solid State Chemistry 179, 716–722.

Cummings, D. E., Caccavo, F., Fendorf, S., Rosenzweig, R. F., 1999. Arsenic mobilization by the dissimilatory Fe(III)-reducing bacterium Shewanella alga BrY. Environmental Science and Technology 33, 723–729.

Cutting, R. S., Coker, V. S., Fellowes, J. W., Lloyd, J. R., Vaughan, D. J., 2009. Mineralogical and morphological constraints on the reduction of Fe(III) minerals by Geobacter sulfurreducens. Geochimica et Cosmochimica Acta 73, 4004–4022.

Das, S., Liu, C. C., Jean, J. S., Lee, C. C., Yang, H. J., 2016. Effects of microbially induced transformations and shift in bacterial community on arsenic mobility in arsenic-rich deep aquifer sediments. Journal of Hazardous Materials 310, 11–19.

Davison, W., 1993. Iron and manganese in lakes. Earth Science Reviews 34, 119–163.

Demopoulos, G. P., 2005. On the preparation and stability of scorodite, In: R.G. Reddy and V. Ramachandran (Eds.), Arsenic Metallurgy, TMS, Warrendale, PA, pp. 25–50.

Downs, R.T. and Hall-Wallace, M., 2003. The American Mineralogist crystal structure database. American Mineralogist 88, 247–250.

Esther, J., Sukla, L. B., Pradhan, N., Panda, S., 2015. Fe (III) reduction strategies of dissimilatory iron reducing bacteria. Korean Journal of Chemical Engineering 32, 1–14.

Ferris, F. G., Tazaki, K., Fyfe, W. S., 1989. Iron oxides in acid mine drainage environments and their association with bacteria. Chemical Geology 74, 321–330.

Folk, R. L., 2005. Nannobacteria and the formation of framboidal pyrite: textural evidence. Journal of Earth System Science 114, 369–374.

Fortin, D., Leppard, G.G., Tessier, A., 1993. Characteristics of lacustrine diagenetic iron oxyhydroxides. Geochimica et Cosmochimica Acta 57, 4391–4404.

Fortin, D. and Langley, S., 2005. Formation and occurrence of biogenic iron-rich minerals. Earth-Science Reviews 72, 1–19.

Guo, H. and Barnard, A. S., 2013. Naturally occurring iron oxide nanoparticles: morphology, surface chemistry and environmental stability. Journal of Materials Chemistry A 1, 27–42.

Hu, S., Liang, Y., Liu, T., Li, F., Lu, Y., Shi, Z., 2020. Kinetics of As(V) and carbon sequestration during Fe(II)-induced transformation of ferrihydrite-As(V)-fulvic acid coprecipitates. Geochimica et Cosmochimica Acta, 272, 160–176.

Islam, F. S., Gault, A. G., Boothman, C., Polya, D. A., Charnock, J. M., Chatterjee, D., Lloyd, J. R., 2004. Role of metal-reducing bacteria in arsenic release from Bengal delta sediments. Nature 430, 68–71.

Islam, F. S., Boothman, C., Gault, A. G., Polya, D. A., Lloyd, J. R., 2005. Potential role of the Fe(III)-reducing bacteria Geobacter and Geothrix in controlling arsenic solubility in Bengal delta sediments. Mineralogical Magazine 69, 865–875.

Kneebone, P.E., O'Day, P.A., Jones, N., Hering, J.G., 2002. Deposition and fate of arsenic in iron- and arsenic-enriched reservoir sediments. Environmental Science and Technology 36, 381–386.

Lindsay, M. B. J., Condon, P. D., Jambor, J. L., Lear, K. G., Blowes, D. W., Ptacek, C. J., 2009. Mineralogical, geochemical, and microbial investigation of a sulfide-rich tailings deposit characterized by neutral drainage. Applied Geochemistry 24, 2212–2221.

Lindsay, M. B. J., Moncur, M. C., Bain, J. G., Jambor, J. L., Ptacek, C. J., Blowes, D. W., 2015. Geochemical and mineralogical aspects of sulfide mine tailings. Applied Geochemistry 57, 157–177.

Lovley, D. R., 1997. Microbial Fe(III) reduction in subsurface environments. FEMS Microbiology Reviews 20, 305–313.

Lovely, D.R., Coastes, J.D., Blunt-Harris, E.L., Phillips, E.J.P., Woodward, J.C., 1996. Humic substances as electron acceptors for microbial respiration. Nature 382, 445–448.

Macy, J. M., Santini, J. M., Pauling, B. V., O'Neill, A. H., Sly, L. I., 2000. Two new arsenate/sulfate-reducing bacteria: mechanisms of arsenate reduction. Archives of Microbiology 173, 49–57.

McGregor, R. G. and Blowes, D. W., 2002. The physical, chemical and mineralogical properties of three cemented layers within sulfide-bearing mine tailings. Journal of Geochemical Exploration 76, 195–207.

Merinero, R., Lunar, R., Somoza, L., Diaz-Del-Rio, V., Martinex-Frias, J., 2009. Nucleation, growth and oxidation of framboidal pyrite associated with hydrocarbon-derived submarine chimneys: lessons learned from the Gulf of Cadiz. European Journal of Mineralogy 21, 947–961.

Nevin, K. P. and Lovley, D. R., 2002. Mechanisms for Fe(III) oxide reduction in sedimentary environments. Geomicrobiology Journal 19, 141–159.

Newman, D. K., Ahmann, D., Morel, F. M. M., 1998. A brief review of microbial arsenate respiration. Geomicrobiology Journal 15, 255–268.

Nicholas, D. R., Ramamoorthy, S., Palace, V., Spring, S., Moore, J. N., Rosenzweig, R. F., 2003. Biogeochemical transformations of arsenic in circumneutral freshwater sediments. Biodegradation 14, 123–137.

Nordstrom, D. K., 1977. Thermochemical redox equilibria of ZoBell's solution. Geochimica et Cosmochimica Acta 41, 1835–1841.

Ohfuji, H. and Rickard, D., 2005. Experimental syntheses of framboids - a review. Earth-Science Reviews 71, 147–170.

Oremland, R.S. and Stolz, J.F., 2003. The ecology of arsenic. Science 300, 939 – 944.

Paktunc, D. and Bruggeman, K., 2010. Solubility of nanocrystalline scorodite and amorphous ferric arsenate: implications for stabilization of arsenic in mine wastes. Applied Geochemistry 25, 674–683.

Parkhurst, D. L., Appelo, C. A. J., 1999. User's Guide to PHREEQC (Version 2) – A Computer program for speciation, batch reaction, one-dimensional transport, and inverse geochemical calculations. Water Resources Investigation Report 99–4259, U.S. Geological Survey.

Pedersen, H. D., Postma, D., Jakobsen, R., Larsen, O., 2005. Fast transformation of iron oxyhydroxides by the catalytic action of aqueous Fe(II). Geochimica et Cosmochimica Acta 69, 3967–3977.

Pokrovski, G. S., Schott, J., Farges, F., Hazemann, J. L., 2003. Iron (III)-silica interactions in aqueous solution: Insights from X-ray absorption fine structure spectroscopy. Geochimica et Cosmochimica Acta 67, 3559–3573.

Qafoku, O., Kovarik, L., Bowden, M. E., Nakouzi, E., Sheng, A., Liu, J., Pearce, C.I., Rosso, K. M., 2020. Nanoscale observations of Fe(II)-induced ferrihydrite transformation. Environmental Science: Nano 7, 2953–2967.

Reardon, E.J., 1979. Complexing of silica by iron(III) in natural waters. Chemical Geology 25, 339 -345.

Revesz, E., Fortin, D., Paktunc, D., 2015. Reductive dissolution of scorodite in the presence of Shewanella sp. CN32 and Shewanella sp. ANA-3. Applied Geochemistry 63, 347–356.

Richard, D., 2021. Framboids. Oxford University Press, 360p.

Robins, R. G., 1987. Solubility and stability of scorodite, FeAsO4.2H2O: discussion. American Mineralogist 72, 842–844.

Sapkota, B., Verbuyst, B., Bain, J., Ptacek, C., Blowes, D., Al, T., 2023. Geochemical and mineralogical investigation of cemented crusts in the tailings cover at Long Lake Gold Mine, Sudbury, Canada. Journal of Hazardous Materials 451, 131192.

Schulz, K., ThomasArrigo, L. K., Kaegi, R., Kretzschmar, R., 2022. Stabilization of ferrihydrite and lepidocrocite by silicate during Fe(II)-catalyzed mineral transformation: impact on particle morphology and silicate distribution. Environmental Science and Technology 56, 5929–5938.

Sidenko, N. V., Khozhina, E. I., Sherriff, B. L., 2007. The cycling of Ni, Zn, Cu in the system "mine tailings-ground water-plants": A case study. Applied Geochemistry 22, 30–52.

Van Aken, P. A. and Liebscher, B., 2002. Quantification of ferrous/ferric ratios in minerals: new evaluation schemes of Fe L_{23} electron energy-loss near-edge spectra. Physics and Chemistry of Minerals 29, 188–200.

van der Zee, C., Roberts, D. R., Rancourt, D. G., Slomp, C. P., 2003. Nanogoethite is the dominant reactive oxyhydroxide phase in lake and marine sediments. Geology 31, 993–996.

Yee, N., Shaw, S., Benning, L.G., Nguyen, T.H., 2006. The rate of ferrihydrite transformation to goethite via the Fe(II) pathway. American Mineralogist 91, 92–96.

Zhu, Y. and Merkel, B., 2001. The dissolution and solubility of scorodite, $FeAsO_4.2H_2O$: evaluation and simulation with PHREEQC2. TU Bergakedemie Frieberg 18, 1–12.

CHAPTER FOUR

CONCLUSIONS

Geochemical and mineralogical characterizations of mine tailings and mine-impacted sediments were conducted at Long Lake, near Sudbury, Ontario. Mineralogical analyses of the tailings indicate moderate to high degrees of sulfide-mineral oxidation at <0.7 m depth below the interface between the tailings and the overlying sand cover. Over the decades since mining ended, sulfide-mineral oxidation has generated acidic porewater that contains elevated concentrations of As, Fe, and SO_4 (up to 346, 2326, and 12,000 mg/L, respectively). The upward transport of solutes from the oxidized tailings to the sand cover due to capillary-pressure gradients resulted in the precipitation of ferric-arsenates and jarosite minerals that cemented the sand particles and formed cemented crusts. Relatively thin (mm-scale) crusts are also formed on the tailings surface due to groundwater discharge where incised stream channels intersect the saturated tailings. The distribution of secondary-mineral precipitates is variable in the pore space of the tailings and sand cover, leading to a discontinuous distribution of cemented crusts both vertically and horizontally. The crusts continually evolve in response to the changes in porewater composition and hydrologic conditions. Their erosion at several locations, however, has become a secondary source of contamination to the surrounding environment. The physical weakening of the surface material by freeze-thaw action allows erosion by surface runoff and stream flow, and transport of crusts downstream to Long Lake via Luke Creek.

Mineralogical analysis of the mine-impacted lake sediment (maximum depth 1.9 m) has identified fragments of tailings-derived cemented crusts, the abundance of which decreases with depth. These fragments are relatively porous compared to the crusts in the tailings, suggesting they have undergone partial-dissolution following burial. Partial-dissolution of scorodite and K/Na-

jarosite, which are the dominant secondary minerals present in the crusts, contribute to elevated aqueous concentrations of As, Fe, K, and SO_4 near the sediment surface, creating concentration gradients that can drive diffusive transport upward into the lake water, and downward into the underlying natural sediment. Preferential dissolution of As from the ferric-arsenate minerals has resulted in lower As/Fe ratios in the sediment-hosted crusts compared to the crusts in the tailings. The depletion and mobilization of As leaves residual ferric-arsenates progressively enriched with Fe(III), and residual Fe(III) precipitates in several morphological forms of Fe-oxyhydroxides, including spherules which consist of lepidocrocite microcrystals and silica in the interstitial spaces. The measurement of $Fe(III)/\Sigma Fe = 0.8$ in the lepidocrocite microcrystals indicates that they contain a mixture of Fe valence states. Fe-oxyhydroxides are common diagenetic reaction products in the mine-impacted sediment, occurring from the sediment surface to depths near the interface between mine-impacted sediment and the underlying natural sediment where secondary Fe- and As-sulfides are formed in response to sulfate reduction. This suggests that the Fe-oxyhydroxides have formed in suboxic to anoxic conditions. A burst-nucleation mechanism is proposed to explain the nucleation and growth of microcrystals, and minimization of the surface-free-energy to volume ratio could cause aggregation of the microcrystals in spheroidal form. The interstitial spaces between the microcrystals are filled with secondary silica.

It is hoped that future remediation efforts may benefit from knowledge of the mineralogical forms of As that control aqueous As concentrations, and from an understanding of the erosion, transport, deposition and diagenetic processes that occur throughout the surficial and lake-sediment environments affected by historic mining.

APPENDICES

Appendix A: Supplementary material for Chapter 2

Solid-phase geochemistry of Long Lake tailings

LL06	Elements	wt%								
Depth (m)	Total S	Al	As	Be	Ca	Co	Cr	Cu	Fe	K
0.03	1.41	6.45	1.34	< 0.001	0.13	0.012	< 0.01	0.019	2.86	0.4
0.17	1.99	6.28	1.02	< 0.001	0.2	0.011	0.01	0.031	2.83	0.5
0.37	2.11	6.37	1.11	< 0.001	0.96	0.015	0.01	0.025	4.75	0.7
0.48	0.34	5.59	2.01	< 0.001	0.4	0.005	0.01	0.009	5.05	0.4
0.67	2.37	5.59	3.16	< 0.001	0.8	0.01	0.01	0.033	5.97	0.4
0.83	3.9	6.28	1.23	< 0.001	0.41	0.012	0.01	0.064	5.29	0.3
1.07	4.26	6.27	1.29	< 0.001	0.3	0.018	0.01	0.047	5.76	0.3
1.25	5.18	6.2	1.61	< 0.001	0.18	0.023	< 0.01	0.067	6.49	0.3
1.53	3.77	6.24	1.13	< 0.001	0.14	0.023	< 0.01	0.044	5.54	0.3
1.83	5.34	6.1	2.38	< 0.001	0.5	0.047	0.01	0.085	8.11	0.4
2.53	4.27	5.91	1.91	< 0.001	0.34	0.028	< 0.01	0.059	6.23	0.4
2.82	2.6	3.75	0.9	< 0.001	0.73	0.048	< 0.01	0.032	3.03	0.4
3.45	0.11	6.69	0.04	< 0.001	1.19	0.003	< 0.01	< 0.005	2.72	1.9
4.10	0.03	7.63	0.02	< 0.001	1.35	0.002	0.02	< 0.005	3.66	2.4

LL06	Elements	wt%									
Depth (m)	Li	Mg	Mn	Ni	Pb	S	Sb	Si	Ti	W	Zn
0.03	< 0.01	0.22	< 0.01	0.01	< 0.01	1.41	< 0.01	34.4	0.15	< 0.005	< 0.01
0.17	< 0.01	0.27	< 0.01	0.011	< 0.01	1.93	< 0.01	32.9	0.15	< 0.005	< 0.01
0.37	< 0.01	1.07	0.02	0.015	< 0.01	2.04	< 0.01	31.7	0.2	< 0.005	0.03
0.48	< 0.01	0.32	< 0.01	< 0.005	< 0.01	0.35	< 0.01	32.1	0.19	< 0.005	< 0.01
0.67	< 0.01	0.3	0.01	0.01	< 0.01	2.29	< 0.01	29.3	0.15	< 0.005	0.01
0.83	< 0.01	0.42	< 0.01	0.014	< 0.01	3.73	< 0.01	30.2	0.16	< 0.005	0.01
1.07	< 0.01	0.24	< 0.01	0.016	< 0.01	4.06	< 0.01	31.4	0.14	< 0.005	0.02
1.25	< 0.01	0.19	< 0.01	0.02	< 0.01	5.06	< 0.01	30.4	0.15	< 0.005	0.03
1.53	< 0.01	0.22	< 0.01	0.017	< 0.01	3.66	< 0.01	31.8	0.14	< 0.005	0.04
1.83	< 0.01	0.59	0.01	0.031	< 0.01	5.25	< 0.01	27.5	0.18	< 0.005	0.1
2.53	< 0.01	0.39	< 0.01	0.02	< 0.01	4.06	< 0.01	28.5	0.16	< 0.005	0.04
2.82	< 0.01	0.29	0.01	0.031	< 0.01	2.45	< 0.01	16.8	0.11	< 0.005	0.07
3.45	< 0.01	1.05	0.04	0.006	< 0.01	0.11	< 0.01	33.7	0.31	< 0.005	< 0.01
4.10	< 0.01	1.44	0.05	0.006	< 0.01	0.02	< 0.01	31.6	0.34	< 0.005	< 0.01

LL03	Elements wt%									
Depth (m)	Total S	Al	As	Be	Ca	Co	Cr	Cu	Fe	K
0.03	2.88	5.28	0.22	< 0.001	0.16	< 0.002	< 0.01	0.007	7.68	0.4
0.13	2.45	5.15	0.79	< 0.001	0.13	< 0.002	< 0.01	0.006	7.62	0.6
0.23	1.46	6.01	1.11	< 0.001	0.09	< 0.002	< 0.01	0.016	2.84	0.4
0.35	2.14	6.15	1.56	< 0.001	0.05	< 0.002	0.01	0.064	3.59	0.4
0.42	1.94	6.63	0.37	< 0.001	0.08	< 0.002	< 0.01	0.051	2.47	0.4
0.51	2.48	6.41	1.78	< 0.001	0.33	0.022	0.01	0.073	3.57	0.4
0.67	3.87	6.5	3.53	< 0.001	0.75	0.046	0.01	0.12	5.29	0.5
0.77	1.18	6.66	0.54	< 0.001	0.36	0.003	< 0.01	0.044	1.64	0.4
0.92	0.61	6.67	0.58	< 0.001	0.34	< 0.002	< 0.01	0.081	1.04	0.4
1.27	7.69	5.34	2.11	< 0.001	0.43	0.022	< 0.01	0.057	8.12	0.3
1.44	5.01	6.41	1.61	< 0.001	0.48	0.024	< 0.01	0.069	6.64	0.4
1.67	6	5.79	2.42	< 0.001	0.47	0.034	< 0.01	0.075	7.12	0.3
1.92	2.03	4.04	0.66	< 0.001	0.47	0.013	< 0.01	0.031	3.44	0.6
2.31	0.06	7.09	< 0.01	< 0.001	1.05	0.002	< 0.01	< 0.005	2.67	1.8
2.99	< 0.01	6.51	< 0.01	< 0.001	1.3	< 0.002	0.01	< 0.005	2.67	1.9
3.48	0.02	7.13	< 0.01	< 0.001	1.33	0.002	< 0.01	< 0.005	3.25	2.2

LL03	Elements wt%										
Depth (m)	Li	Mg	Mn	Ni	Pb	S	Sb	Si	Ti	W	Zn
0.03	< 0.01	0.11	< 0.01	< 0.005	< 0.01	2.95	< 0.01	29.9	0.14	< 0.005	< 0.01
0.13	< 0.01	0.09	< 0.01	< 0.005	< 0.01	2.49	< 0.01	30.2	0.13	< 0.005	< 0.01
0.23	< 0.01	0.05	< 0.01	< 0.005	< 0.01	1.46	< 0.01	34.3	0.14	< 0.005	< 0.01
0.35	< 0.01	0.1	< 0.01	< 0.005	< 0.01	2.05	< 0.01	33.4	0.15	< 0.005	< 0.01
0.42	< 0.01	0.14	< 0.01	< 0.005	< 0.01	1.96	< 0.01	35.5	0.15	< 0.005	< 0.01
0.51	< 0.01	0.33	< 0.01	0.017	< 0.01	2.43	< 0.01	33.5	0.16	< 0.005	< 0.01
0.67	< 0.01	0.49	< 0.01	0.031	< 0.01	3.78	< 0.01	30.2	0.16	< 0.005	< 0.01
0.77	< 0.01	0.27	< 0.01	< 0.005	< 0.01	1.16	< 0.01	35.2	0.19	< 0.005	< 0.01
0.92	< 0.01	0.18	< 0.01	< 0.005	< 0.01	0.62	< 0.01	35.5	0.21	< 0.005	< 0.01
1.27	< 0.01	0.34	< 0.01	0.022	< 0.01	7.33	< 0.01	28.5	0.21	< 0.005	< 0.01
1.44	< 0.01	0.39	0.01	0.019	< 0.01	4.78	< 0.01	29.8	0.14	< 0.005	0.04
1.67	< 0.01	0.22	< 0.01	0.03	< 0.01	5.79	< 0.01	30.9	0.21	< 0.005	0.04
1.92	< 0.01	0.21	< 0.01	0.012	< 0.01	1.88	< 0.01	21.6	0.15	< 0.005	0.03
2.31	< 0.01	0.98	0.03	0.005	< 0.01	0.05	< 0.01	33.2	0.33	< 0.005	< 0.01
2.99	< 0.01	1.01	0.03	< 0.005	< 0.01	0.02	< 0.01	33.2	0.31	< 0.005	< 0.01
3.48	< 0.01	1.23	0.04	0.006	< 0.01	0.01	< 0.01	32.3	0.34	< 0.005	< 0.01

Additional SEM-EDS data from Long Lake tailings

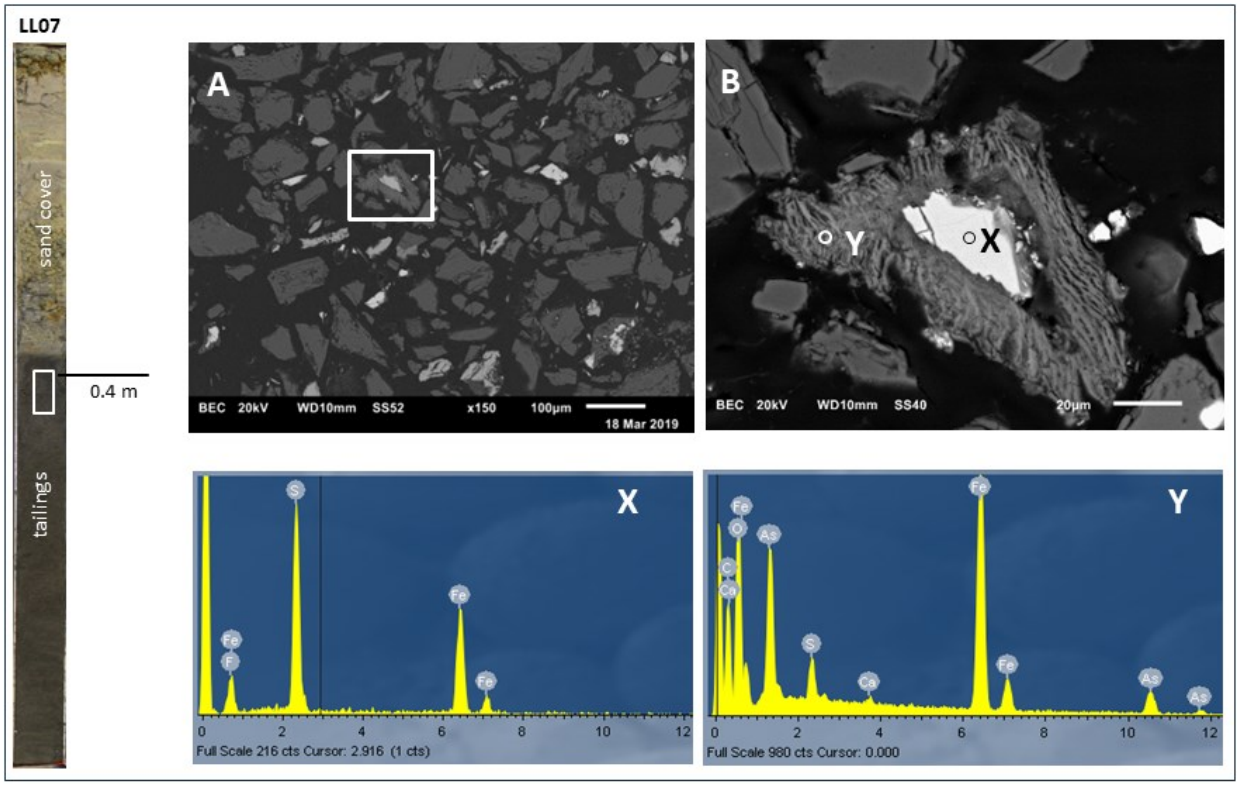

Mineralogy of the tailings at LL07 (0.4 mbgs). (A) Backscattered electron image illustrating weathered sulfide minerals; white rectangle represents the magnified region corresponding to (B). X and Y represent locations for EDS analyses. (Below) The EDS spectra indicate that these phases are composed of Fe-S and Fe-As-S-O, respectively.

Appendix B: Supplementary material for Chapter 3

Solid-phase geochemistry of Long Lake sediments

Shallow Core	Elements	wt%							
Depth (m)	Na	K	Ca	Mg	Sr	Ba	Al	Cr	Mn
0.05	0.0248	0.0310	0.0599	0.0649	0.0013	0.0046	0.2006	0.0009	0.0038
0.09	0.0297	0.0529	0.1004	0.1667	0.0018	0.0038	0.5474	0.0020	0.0143
0.14	0.0379	0.0765	0.1320	0.1745	0.0028	0.0058	0.4732	0.0022	0.0079
0.18	0.0216	0.0459	0.2220	0.2306	0.0016	0.0042	0.6059	0.0025	0.0078
0.23	0.0198	0.0250	0.3380	0.2439	0.0017	0.0021	0.4770	0.0022	0.0091
0.27	0.0216	0.0293	0.3987	0.3029	0.0019	0.0018	0.5605	0.0026	0.0114
0.32	0.0261	0.0366	0.5289	0.3874	0.0023	0.0021	0.6106	0.0029	0.0138
0.36	0.0231	0.0357	1.3867	0.9278	0.0022	0.0019	0.5469	0.0024	0.0136
0.41	0.0221	0.0341	1.2238	0.8646	0.0019	0.0016	0.5266	0.0021	0.0123
0.45	0.0265	0.0406	1.8505	1.2092	0.0029	0.0021	0.6525	0.0029	0.0156
0.50	0.0359	0.0607	2.6666	1.8074	0.0039	0.0028	0.8666	0.0037	0.0229
0.54	0.0234	0.0324	1.4830	0.9608	0.0024	0.0015	0.5096	0.0022	0.0128
0.59	0.0238	0.0336	2.2320	1.4783	0.0025	0.0015	0.5224	0.0023	0.0150
0.63	0.0234	0.0327	2.1232	1.3495	0.0024	0.0015	0.4906	0.0022	0.0161
0.68	0.0190	0.0219	1.5949	0.9556	0.0021	0.0010	0.3751	0.0022	0.0126

Shallow Core	Elements	wt%								
Depth (m)	Fe	Co	Ni	Cu	Zn	As	S	C	P	N
0.05	3.9490	0.0003	0.0011	0.0058	0.0013	1.9288	0.1939	0.7491	0.0189	0.0202
0.09	8.5439	0.0005	0.0020	0.0082	0.0025	3.7406	0.2590	3.6651	0.0441	0.0617
0.14	8.0016	0.0005	0.0014	0.0062	0.0029	3.3625	0.2630	0.5534	0.0465	0.0117
0.18	3.6084	0.0004	0.0011	0.0020	0.0023	1.7636	0.0872	0.6368	0.0435	0.0157
0.23	0.9149	0.0004	0.0010	0.0003	0.0013	0.1454	0.0082	0.0216	0.0484	0.0000
0.27	0.8364	0.0006	0.0013	0.0006	0.0015	0.0229	0.0003	0.0193	0.0504	0.0000
0.32	0.9109	0.0003	0.0013	0.0007	0.0017	0.0251	0.0021	0.0023	0.0497	0.0000
0.36	0.9043	0.0004	0.0013	0.0007	0.0015	0.0413	0.0057	0.0354	0.0449	0.0000
0.41	0.7754	0.0006	0.0010	0.0006	0.0015	0.0064	0.0074	0.0230	0.0283	0.0000
0.45	0.9575	0.0005	0.0012	0.0008	0.0016	0.0296	0.0070	0.0521	0.0529	0.0000
0.50	1.3193	0.0007	0.0020	0.0011	0.0021	0.0228	0.0131	0.0938	0.0552	0.0000
0.54	0.7602	0.0004	0.0012	0.0008	0.0013	0.0094	0.0044	0.0477	0.0471	0.0000
0.59	0.7970	0.0005	0.0014	0.0006	0.0024	0.0068	0.0016	0.0002	0.0429	0.0000
0.63	0.8546	0.0003	0.0010	0.0005	0.0014	0.0041	0.0042	0.0000	0.0477	0.0000
0.68	0.8474	0.0003	0.0009	0.0004	0.0011	0.0025	0.0003	0.0000	0.0549	0.0000

Deep Core	Elements	wt%							
Depth (m)	Na	K	Ca	Mg	Sr	Ba	Al	Cr	Mn
0.06	0.0338	0.0289	0.0352	0.0726	0.0010	0.0032	0.6494	0.0014	0.0049
0.13	0.0519	0.0334	0.0725	0.0831	0.0013	0.0028	0.4209	0.0013	0.0081
0.19	0.0254	0.0302	0.0584	0.0795	0.0009	0.0025	0.4224	0.0014	0.0045
0.26	0.0272	0.0383	0.0655	0.0836	0.0017	0.0057	0.4850	0.0018	0.0078
0.32	0.0343	0.0355	0.0848	0.1092	0.0017	0.0050	0.4538	0.0018	0.0106
0.38	0.0185	0.0267	0.0506	0.0880	0.0011	0.0039	0.4139	0.0015	0.0060
0.45	0.0196	0.0321	0.0627	0.1054	0.0014	0.0045	0.5481	0.0020	0.0082
0.51	0.0191	0.0298	0.0627	0.1063	0.0010	0.0029	0.8114	0.0021	0.0069
0.58	0.0157	0.0332	0.0708	0.1175	0.0011	0.0021	0.6944	0.0022	0.0085
0.64	0.0172	0.0281	0.0583	0.0848	0.0013	0.0023	0.4127	0.0016	0.0055
0.70	0.0106	0.0178	0.0273	0.0473	0.0009	0.0030	0.1837	0.0009	0.0020
0.77	0.0148	0.0235	0.0475	0.0819	0.0009	0.0030	0.2882	0.0017	0.0040
0.83	0.0159	0.0230	0.0702	0.0702	0.0014	0.0037	0.2877	0.0012	0.0045
0.90	0.0232	0.0352	0.0861	0.0928	0.0015	0.0036	0.3730	0.0017	0.0053
0.96	0.0108	0.0178	0.0405	0.0593	0.0008	0.0028	0.2081	0.0009	0.0026
1.02	0.0183	0.0262	0.0703	0.0817	0.0013	0.0052	0.3207	0.0015	0.0053
1.09	0.0171	0.0272	0.0512	0.0767	0.0010	0.0048	0.3365	0.0014	0.0034
1.15	0.0128	0.0188	0.0532	0.0756	0.0007	0.0037	0.3101	0.0014	0.0054
1.22	0.0204	0.0282	0.0682	0.1007	0.0008	0.0055	1.3425	0.0023	0.0145
1.28	0.0235	0.0425	0.1592	0.1424	0.0015	0.0038	1.0885	0.0037	0.0124
1.34	0.0270	0.0445	0.1302	0.1598	0.0011	0.0031	0.9003	0.0037	0.0117
1.41	0.0294	0.0506	0.1671	0.2021	0.0014	0.0037	1.1630	0.0037	0.0143
1.47	0.0413	0.0576	0.4374	0.2332	0.0030	0.0061	1.0808	0.0040	0.0282
1.54	0.0484	0.0463	0.3630	0.1555	0.0027	0.0078	0.9174	0.0031	0.0306
1.60	0.0407	0.0459	0.2123	0.2095	0.0016	0.0060	1.1183	0.0039	0.0136
1.66	0.0234	0.0419	0.1773	0.1627	0.0013	0.0055	1.3931	0.0040	0.0107
1.73	0.0141	0.0635	0.1632	0.3080	0.0014	0.0070	1.3123	0.0030	0.0105
1.79	0.0137	0.0630	0.1642	0.3217	0.0014	0.0078	1.3695	0.0032	0.0110
1.86	0.0153	0.0680	0.1805	0.3219	0.0015	0.0070	1.3163	0.0032	0.0106
1.92	0.0220	0.0588	0.3939	0.3620	0.0023	0.0033	1.0119	0.0029	0.0136
1.98	0.0272	0.0610	0.5428	0.4718	0.0027	0.0032	0.8951	0.0035	0.0230
2.05	0.0268	0.0579	0.6787	0.5888	0.0025	0.0028	0.8813	0.0037	0.0183
2.11	0.0274	0.0613	2.9195	2.0028	0.0029	0.0024	0.8017	0.0035	0.0253

Deep Core	Elements wt%									
Depth (m)	Fe	Co	Ni	Cu	Zn	As	S	C	P	N
0.06	5.3785	0.0003	0.0012	0.0040	0.0015	1.9748	0.2867	1.0405	0.0246	0.0401
0.13	4.2839	0.0005	0.0024	0.0092	0.0018	1.6096	0.3027	1.4435	0.0232	0.0510
0.19	4.0393	0.0003	0.0033	0.0072	0.0015	1.4913	0.1740	1.3405	0.0271	0.0457
0.26	9.6077	0.0004	0.0037	0.0109	0.0029	3.8728	0.2696	1.7047	0.0509	0.0644
0.32	9.1796	0.0006	0.0042	0.0149	0.0027	3.0735	0.2903	1.7229	0.0363	0.0588
0.38	7.0803	0.0004	0.0031	0.0102	0.0020	2.5878	0.2541	1.4527	0.0343	0.0527
0.45	9.8587	0.0006	0.0035	0.0114	0.0026	3.0498	0.3244	1.9684	0.0441	0.1178
0.51	9.1687	0.0007	0.0032	0.0120	0.0026	2.3180	0.4961	2.5347	0.0372	0.1404
0.58	10.0579	0.0008	0.0041	0.0111	0.0031	2.8994	0.5265	1.8125	0.0412	0.0565
0.64	5.6068	0.0005	0.0033	0.0095	0.0020	1.5905	0.2662	1.8771	0.0263	0.0561
0.70	2.7799	0.0002	0.0011	0.0051	0.0010	1.2895	0.0961	0.7443	0.0164	0.0152
0.77	6.6442	0.0004	0.0035	0.0165	0.0018	2.6828	0.2078	1.1819	0.0302	0.0437
0.83	3.7124	0.0001	0.0031	0.0087	0.0017	1.4590	0.1535	0.7510	0.0240	0.0181
0.90	7.9073	0.0007	0.0061	0.0139	0.0028	3.3456	0.2465	1.6028	0.0427	0.0847
0.96	2.7419	0.0003	0.0021	0.0068	0.0012	1.0778	0.1208	0.8041	0.0151	0.0214
1.02	8.1328	0.0008	0.0067	0.0149	0.0027	3.1229	0.2145	1.0387	0.0340	0.0421
1.09	6.2532	0.0004	0.0039	0.0133	0.0019	2.4103	0.2067	1.0270	0.0369	0.0356
1.15	6.9393	0.0005	0.0046	0.0116	0.0021	2.0476	0.2398	1.0781	0.0251	0.0354
1.22	6.0937	0.0008	0.0100	0.0250	0.0040	1.8596	0.3246	1.3297	0.0337	0.0465
1.28	15.7353	0.0034	0.0507	0.0558	0.0112	3.8405	1.2623	7.7764	0.0718	0.5472
1.34	14.6210	0.0024	0.0307	0.0374	0.0080	3.7425	1.2763	7.7123	0.0641	0.5497
1.41	12.3531	0.0018	0.0137	0.0259	0.0069	2.9236	1.0315	8.5054	0.0668	0.5166
1.47	13.1658	0.0043	0.0176	0.0384	0.0169	2.4965	1.0804	10.8823	0.0672	0.6408
1.54	20.5716	0.0036	0.0114	0.0408	0.0207	3.1789	0.9582	13.0516	0.0799	0.7616
1.60	18.0920	0.0035	0.0092	0.1069	0.0335	2.5248	1.1656	10.2038	0.0826	0.9453
1.66	12.9151	0.0041	0.0073	0.0259	0.0185	1.9679	1.3606	18.5039	0.0734	0.8506
1.73	3.2738	0.0015	0.0022	0.0024	0.0129	0.5984	0.3492	4.8193	0.0349	0.2388
1.79	3.3845	0.0009	0.0018	0.0015	0.0054	0.4668	0.2811	4.8551	0.0358	0.3081
1.86	2.9246	0.0007	0.0017	0.0012	0.0051	0.2810	0.1483	3.5335	0.0352	0.2150
1.92	1.6795	0.0009	0.0016	0.0011	0.0040	0.0935	0.0573	1.0034	0.0445	0.0432
1.98	1.5075	0.0015	0.0022	0.0010	0.0035	0.0370	0.0127	0.1760	0.0514	0.0000
2.05	1.5498	0.0012	0.0019	0.0011	0.0026	0.0175	0.0181	0.0941	0.0582	0.0000
2.11	1.5818	0.0007	0.0016	0.0010	0.0025	0.0147	0.0081	0.1073	0.0522	0.0000

Aqueous-phase geochemistry of Long Lake sediments

Shallow Core				mmol/kgH2O			
Depth (m)	pH	Eh (mV)	Alkalinity (meq HCO_3^-/kgH_2O)	Na	K	Ca	Mg
0.11	6.82	90	2.1727	1.6196	0.2335	0.7416	0.3843
0.34	6.80	-2	2.2547	1.4957	0.1442	0.9678	0.4881
0.56	6.80	274	7.7816	1.4900	0.1130	0.9848	0.4774
0.79	6.77	287	2.3063	1.4357	0.0400	0.9185	0.4255
1.01	7.06	309	3.2560	1.8365	0.0492	1.5304	0.6449

Shallow Core	mmol/kgH2O									
Depth (m)	Sr	Al	As	SO4	Fe	Mn	Zn	Cr	Co	Cl
0.11	0.0024	0.0028	1.0247	4.5399	3.2471	0.0082	0.0065	0.0000	0.0001	1.6071
0.34	0.0028	0.0035	0.4913	2.1828	1.6157	0.0106	0.0003	0.0000	0.0000	2.5965
0.56	0.0025	0.0035	0.3392	1.2541	0.6063	0.0119	0.0001	0.0000	0.0001	2.9632
0.79	0.0021	0.0077	0.1702	0.6373	0.1183	0.0081	0.0002	0.0000	0.0000	3.3832
1.01	0.0032	0.0055	0.3083	NA	0.1295	0.0095	0.0001	0.0000	0.0000	NA

Deep Core				mmol/kgH2O			
Depth (m)	pH	Eh (mV)	Alkalinity (meq HCO_3^-/kgH_2O)	Na	K	Ca	Mg
0.16	7.22	43	4.0644	0.8491	0.2478	0.4711	0.2588
0.48	7.19	-61	10.9577	1.1735	0.3662	0.8509	0.4370
0.8	7.07	0	9.1056	3.5391	0.3417	1.5406	0.6350
1.11	6.95	13	7.4430	1.3783	0.3182	1.1219	0.5045

Deep Core	mmol/kgH2O									
Depth (m)	Sr	Al	As	SO4	Fe	Mn	Zn	Cr	Co	Cl
0.16	0.0022	0.0034	1.0427	1.1555	2.2924	0.0073	0.0004	0.0000	0.0000	0.7335
0.48	0.0026	0.0048	1.2231	0.7260	3.6728	0.0107	0.0006	0.0000	0.0001	1.0023
0.8	0.0033	0.0194	1.0537	0.9332	4.1577	0.0179	0.0296	0.0001	0.0002	1.0120
1.11	0.0022	0.0240	0.4852	0.7034	2.8213	0.0195	0.0073	0.0001	0.0001	1.0737

Additional SEM-EDS data from Long Lake tailings

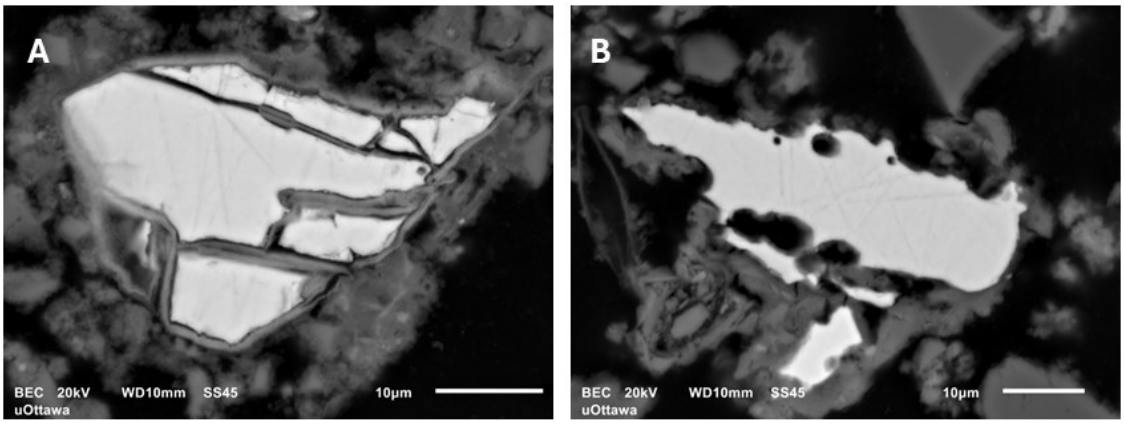

(A, B) Backscattered electron images illustrating weathered sulfide-minerals in the mine-impacted lake sediment. These were eroded and transported from the tailings to the sediment delta.

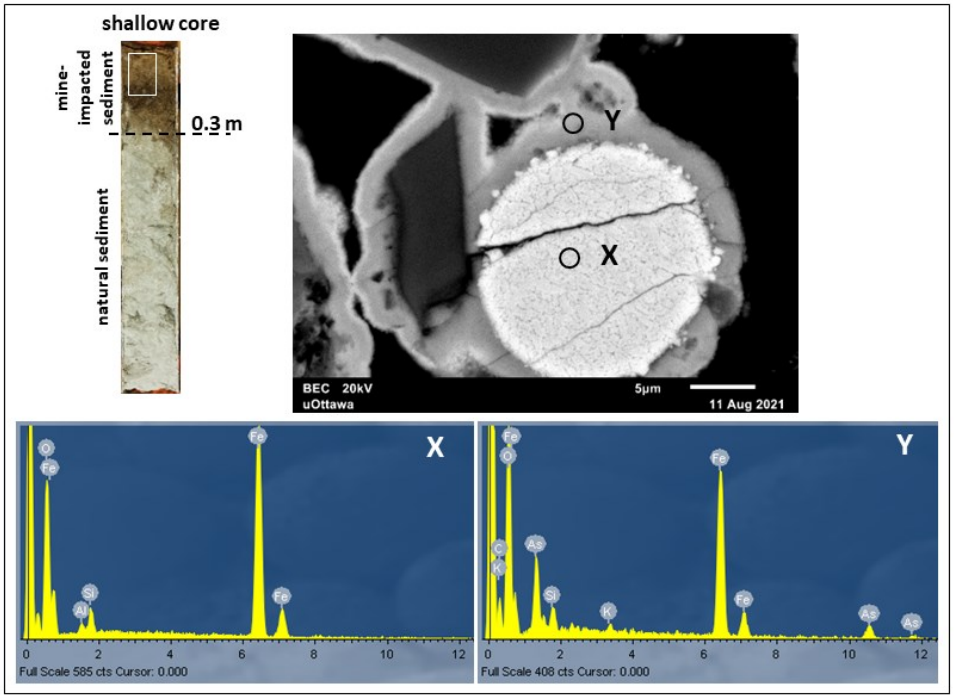

(Above) Backscattered electron image illustrating a spherule in the mine-impacted sediment at the shallow location indicated by a white rectangle in the photograph. X and Y represent locations for EDS analyses. (Below) The EDS spectra indicate that these phases are mainly composed of Fe-O, and Fe-As-O, respectively.